MODELING OF TURBULENT CAVITATING FLOWS

by

Chien-Chou Tseng

A dissertation submitted in partial fulfillment
of the requirements for the degree of
Doctor of Philosophy
(Mechanical Engineering)
in The University of Michigan
2010

Doctoral Committee:

Professor Steven L. Ceccio, Co-Chair
Professor Wei Shyy, Co-Chair
Professor Marc Perlin
Professor William W. Schultz

To My Parents, My Wife Chin-Yi Lin, and My Son Ethan Tseng

ACKNOWLEDGEMENTS

First of all, I would like to express my grateful thanks to my research advisor Professor Wei Shyy. I am very grateful that I have received help from him as a student and even as a friend. I would also like to thank Prof. Steven L. Ceccio. I have learned fundamental science and engineering and also professional skills from the working experience with these two true scholars.

Many thanks go to my committee members, Prof. Marc Perlin and Prof. William W. Schultz, for serving on my committee and providing valuable advices on my dissertation.

I would also like to thank the members of Prof. Shyy's group, Dr. Hikaru Aono, Mr. Young-Chang Cho, Mr. Wenbo Du, Dr. Amit Gupta, Mr. Ez Hassan, Mr. Chang-Kwon Kang, Mr. Chih-Kuang Kuan, Mr. Jaeheon Sim, Miss, Jianing Tang, Mr. Patrick Trizila, for their support during the past years. I will miss our coffee break when we made joke to each other.

I really appreciate the help from Prof. Yingjie Wei during his visit, and also thank Dr. Xiangchun Zhang's help regarding surrogate models.

I gratefully acknowledge the support of my research sponsors, NASA under the Constellation University Institute Program (CUIP). Most important of all, without the spiritual and financial support from my parents, Mrs. Hsueh-Ju Tseng and Dr. Cheng-Chuan Tseng, I can not finish this degree. My wife, Chin-Yi Lin, has accompanied with me for every sweet and bitter moment. I could not imagine the outcome of this adventure if she were not here with me. Finally, thank to my little son, Ethan Tseng, for being my little four-leaved clover.

TABLE OF CONTENTS

LIST OF TABLES

LIST OF FIGURES

LIST OF SYMBOLS

σ_∞	Free stream cavitation number; cavitation number based on the free stream temperature
σ	Local cavitation number; cavitation number based on the local temperature
B	B-factor
$C_{\varepsilon 1}, C_{\varepsilon 2}, \sigma_\varepsilon, \sigma_k$	Coefficients of $k-\varepsilon$ turbulence model
c	Chord length
C	Heat capacity
Cp	Pressure coefficient
D	Characteristic length scale
d	Wall distance
f	Eddy viscosity correction function
f_v	Vapor mass fraction
h	Enthalpy
I	Turbulence intensity
k	Turbulent kinetic energy
L	Latent heat
m^+, m^-	Source and sink terms in the cavitation model
n	Normal direction
n_b	Bubble number density
Pr	Prandtl number
P_t	Production term of turbulent kinetic energy
P_v	Saturation vapor pressure
P_{diff}	L_2 norm between experiment and predicted pressure
Re	Reynolds number
R	Bubble radius/Liquid-to-vapor density ratio
S	Sensitivity indices
S_a	Interface area
S_{cv}	Control volume face area
S_v	Surface area of the bubbles

T	Temperature
T_{diff}	L_2 norm between experiment and predicted temperature
t_∞	Reference time scale, $t_\infty = L/U_\infty$
U_∞	Reference velocity
u	Velocity
$U_{v,n}$	Normal component of the vapor velocity moving away from the interface
$U_{I,n}$	Normal interfacial velocity
V	Total variance
Δv	Difference of specific volume during phase change in Clapeyron equation
ΔT^*	Reference temperature drop
x	Space variable
α_l	Liquid volume fraction
α_v	Vapor volume fraction
ρ	Density
μ	Dynamic viscosity
$\mu_T/\mu_L\|_{inlet}$	Eddy-to-laminar viscosity ratio at the inlet
φ_m	Mixture property
ε	Turbulent dissipation rate
ω	Specific dissipation rate
Δ	Filter size in filter-based model
δ^*	Displacement thickness

Subscript

j	Component
l	Liquid
L	Laminar
m	Mixture property
T	Turbulent
v	Vapor
ω	Free stream quantities

ABSTRACT

MODELING OF TURBULENT CAVITATING FLOWS

by

Chien-Chou Tseng

Co-Chairs: Steven L. Ceccio and Wei Shyy

The goal of this dissertation is to establish a predictive tool for turbulent cavitating flows, including those under cryogenic conditions with noticeable thermal effects. The modeling framework consists of a transport-based cavitation model with ensemble-averaged fluid dynamics equations and turbulence closures. The cavitation models used in this study include a phenomenological model with empirical supports and an interfacial dynamics model that utilizes continuity and force balance across the interfaces. For the turbulence closure, a filter-based approach and density correction approach has been imposed to the two equation k-ε model.

The reported experimental investigations contain insufficient details regarding the inlet turbulence characteristics of the flow field. However, the inlet turbulent quantities can substantially impact the outcomes because the viscous effect can modify the effective shape of a solid object, which causes noticeable variations in the predicted multiphase flow structures. A filter-based turbulence closure is utilized to reduce the impact of the inlet turbulent quantities based on the local resolution. Its effectiveness is confirmed by

both isothermal and cryogenic cavitation. In addition, the thermal effect and the competing effect between the cavitation number and the density ratio effects are investigated by evaporation and condensation dynamics under the cryogenic conditions. Based on the surrogate-based global sensitivity analysis under cryogenic conditions, one can assess the role of model parameters and uncertainties in material properties. It is revealed that variables represented for the evaporation rate are more critical than those for the condensation rate. Furthermore, the recommended model parameter values are optimized by tradeoffs between pressure and temperature predictions.

For unsteady cavitating flows, the phenomenological model and interfacial dynamics model are utilized by the turbulence closure with the filter-based approach, the density correction approach, and a hybrid approach that blends the previous two methods. It is discovered that the eddy viscosity near the closure region can significantly influence the capture of the detached cavity. From the experimental validations, no single model combination performs best in all aspects. Furthermore, the implications of the parameters contained in the different cavitation models are investigated. The phase change process is more pronounced near the detached cavity, which is more substantial in the interfacial dynamics model.

CHAPTER I

INTRODUCTION

1.1 BACKGROUND AND THERMODYNAMICS OF CAVITATION

Cavitation typically occurs when the fluid pressure is lower than the vapor pressure at a local thermodynamic state [1-5]. It is often associated with undesired effects such as noise, vibration, erosion, and power loss. Cavitation can happen in nozzles, injectors, propellers, hydrofoil, and a variety of other fluid machinery components.

As cavitation occurs, the forming vapor phase will replace the liquid phase inside the cavity. In order to maintain the vapor phase, the surrounding liquid will adjust its thermodynamic state and experience evaporative cooling, which causes the temperature to drop around the cavity. For fluids such as water, due to a very large ratio between liquid and vapor densities, approximately $O(10^5)$, these thermal effects are insignificant during the cavitation process.

Cryogenic liquids, including oxygen, nitrogen, and hydrogen, are popular fuels for commercial launch vehicles as propellants because the by-products are clean and the power/gallon ratio is high. A key design issue related to rocket fuel and oxidizer pumps is the minimum pressure that the design can tolerate for a given inlet temperature and

rotating speed. To keep inlet pressure low (reduce tank weight) and pump rotational speeds high (reduce engine weight), cavitation often appears in the inducer section. To date, there is no established method capable of predicting the actual loads due to cavitation on the inducer blades. The unsteadiness of the cavitating pump can couple with the feed or discharge system to cause large component oscillations. Virtually every rocket engine system designed in the U.S. has experienced issues with cavitating elements in the pump. This includes recent programs like ATP turbopumps for the SSME, the Fastrac LOX pump, and the RS-68 commercial engine. An integrated framework based on computational modeling and control strategies is desirable to treat this critical and difficult issue.

For cryogenic fluids, the liquid/vapor density ratios are not as high as that of water, and other quantities such as latent heat and thermal conductivity can influence the thermal field more substantially than for water. Representative values of these quantities and the pressure-temperature saturation curves are listed and illustrated in Table 1.1 and Figure 1.1, respectively. The cryogenic fluids such as nitrogen have significantly higher slopes of pressure-temperature saturation curve than water [6], indicating that the vapor pressure can vary substantially due to the thermal effect. Based on the Clapeyron equation [7] at representative working temperatures:

$$\frac{dP_v}{dT} = \frac{L}{T\Delta v} \tag{1.1}$$

The sensitivity of the vapor pressure with respect to temperature for liquid nitrogen and hydrogen are 20kPa/K (83K) and 28kPa/K (22K), respectively, and only 0.19kPa/K for water under room temperature.

Table 1.1 Variation of physical properties for water (298K), liquid nitrogen (83K), and liquid hydrogen (22K) on saturation curves. [6]

Substance	Heat capacity (*J/Kg K*)	Density ratio	Thermal conductivity (*W/mK*)	*L* (*KJ/Kg*)	Δv
Water (298k)	4200	43220	681	2442	43.35
N_2 (83k)	2075	95	134	190	0.12
H_2 (20k)	9484	57	103	446	0.79

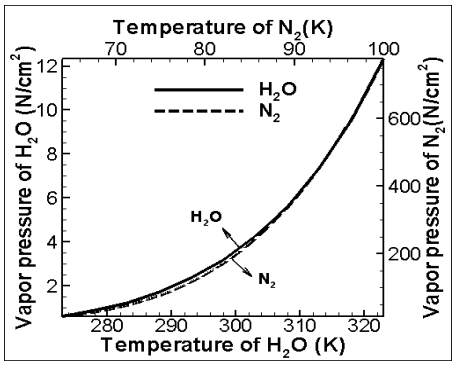

(a)P_v vs. T

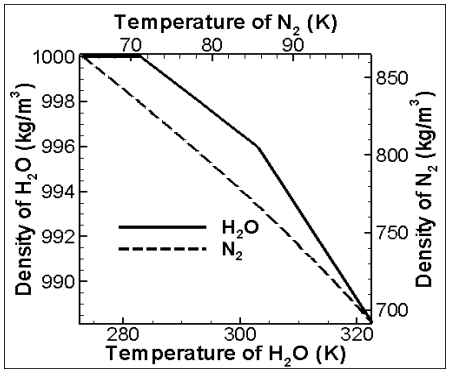

(b) ρ_v vs. T

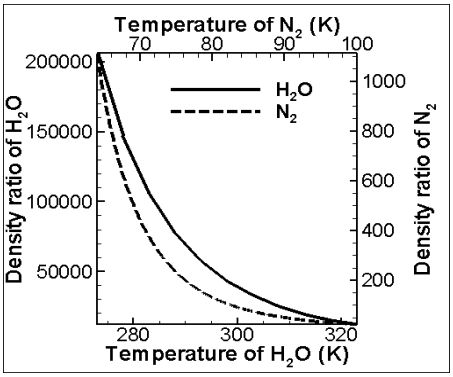

(c) ρ_l/ρ_v vs. T

Figure 1.1 Variation of physical properties for liquid nitrogen and water along saturation curve [6]

(Solid lines represnt water and use bottom and left as x-axis and y-axis in each figure; dash lines represnt liquid nitrogen and use top and right as x-axis and y-axis in each figure)

The B-factor, which can estimate the scale of temperature difference during evaporative cooling, can be derived based on a simple heat balance between the two phases:

$$\rho_v V_v L = \rho_l V_l C_l \Delta T$$
$$B = \frac{V_v}{V_l} = \frac{\Delta T}{\Delta T^*}; \Delta T^* = \frac{\rho_v L}{\rho_l C_l} \quad (1.2)$$

B-factor is defined as the volume ratio between the vapor phase and liquid phase (V_v/V_l), and the reference temperature drop ΔT^* of water, liquid nitrogen, and liquid hydrogen from Table 1.1 will be 0.013K, 0.96K, and 0.82K respectively. In order to maintain comparable cavity size (keep B-factor as a constant), there will be substantial temperature drop ΔT due to the greater heat transfer involved for cryogenic liquids (larger reference temperature drop ΔT^*) [1,8,9]. Equations (1.1) and (1.2) clearly demonstrate that the isothermal assumption, which is often used for water under room temperature, is inappropriate for cryogenic cavitation.

The dynamic similarity for isothermal cases such as water is governed by the cavitation number $\sigma_\infty=(P_\infty-P_v(T_\infty))/0.5\rho_l U_\infty^2$ based on a constant vapor pressure $P_v(T_\infty)$. For cryogenic cavitation, the actual local cavitation number σ needs to be corrected according to the local temperature: $\sigma=(P_\infty-P_v(T))/0.5\rho_l U_\infty^2$. Utturkar et al. [1] and Goel et al. [9] use the first order approximation as follows:

$$\frac{1}{2}\rho_l U_\infty^2(\sigma-\sigma_\infty) = \frac{dP_v}{dT}(T_\infty - T)$$
$$\sigma = \sigma_\infty - \frac{dP_v}{dT}\frac{\Delta T}{0.5\rho_l U_\infty^2}; \ \Delta T = T - T_\infty < 0 \quad (1.3)$$

Equation (1.3) clearly shows the temperature dependency of cavitation, and the local temperature drop in cryogenic cavitation will produce a noticeable rise for the local cavitation number σ. The rise in σ suppresses the cavitation intensity compared with that

under isothermal assumption [9]. The detailed impact of the thermal-sensible material properties on the cavitation model will be introduced later.

1.2 REVIEWS FOR THE KEY ASPECTS OF CAVITATION DYNAMICS

Many papers and books have been published in the field of cavitation, e.g., [1-3,10]. Instead of recounting the large body of literature in the field, the following samples of papers from the experimental angle regarding unsteadiness, geometry, 3D effect, main flow structure, thermal effects, and turbulence are selected to help motivate the development of simulation tools. Table 1.2 highlights the overview for these selected experimental studies.

Kubota et al. [11] have demonstrated that the convection essence of cavitation and the unsteady structure of cloud cavitation can occur even when the hydrofoil is stationary and the inlet is steady. Leroux et al. [12] have investigated the unsteadiness of cavitation for water past NACA66 hydrofoil. At the cavity closure, the pressure coefficient experiences an adverse pressure gradient. It has been determined that the intensity of pressure fluctuations is clearly larger in the area close to the closure region. As the cavitation number decreases and the cavity length increases, the fluctuations also become larger with a bigger affected area.

For water cloud cavitation, Kawanami et al. [13] have demonstrated that the re-entrant jet after the closure region triggers the shedding of the cloud cavitation. The re-entrant jet is rushed from the trailing edge to the leading edge of the sheet cavity. Therefore, the re-entrant jet flows under the sheet cavity and does not propagate along the collapse of the

sheet cavity. Furthermore, Kawanami et al. [13] have displayed the geometric impacts for re-entrant jet structures. If an obstacle placed on the hydrofoil after the closure region has enough height, the obstacle can suppress and block the propagation of the re-entrant jet, and the pressure fluctuation near the closure region will become smaller together with the reduction of noise and drag force. Laberteaux and Ceccio [14] have observed two types of partial cavities with two distinct behaviors: closed partial cavities formed on a two-dimensional NACA0009 hydrofoil, and open partial cavities without re-entrant flow formed on a plano-convex hydrofoil. A closed partial cavity has a clear interface and a cavity closure relatively free of bubbles. On the other hand, an open cavity is typically frothy and has a periodically varying length associated with the shedding of vapor clouds. Callenaere et al. [15] have studied the cavitation instability induced by the development of a re-entrant jet for water past a back step channel. The re-entrant jet will be created if the adverse pressure gradient near the closure region is large enough. A simplified solution has been analytically solved to relate the thickness of the re-entrant jet to the cavity length. Gopalan and Katz [16] have demonstrated that the collapse of vapor bubbles in the closure region for sheet cavitation is the primary source of vorticity production. Besides, the change in the size of the cavity will result in significant changes in the turbulence level and momentum thickness of the downstream boundary layer. Also, Li and Ceccio [17] have shown that traveling bubbles close to the surface can induce local turbulent regions by stretching the boundary layer, thus creating streamwise vorticity.

Laberteaux and Ceccio [18] have examined 3D effects, such as spanwise variation of a hydrofoil. If the re-entrant jet exists in the closure region of a 3D partial cavity, the re-entrant jet could be redirected away from the cavity interface. This allows for a steady and closed cavity. Therefore, the flows around the closed cavity are essentially irrotational and laminar by the weaker cavitation strength. This demonstrates that a hydrofoil with a spanwise variation changes the topology of the cavity when compared with that of a 2D hydrofoil in the same flow conditions. As a result, the dependency of cavitation is strongly coupled with the complicated geometry, and hence similar cavitation numbers can exhibit totally different flow structures. Furthermore, this implies that selecting a characteristic length for simulation is critical. The 3D effect in [18] shows that an additional direction will suppress the unsteadiness, which should be investigated more through simulation. The geometry together with 3D effect, turbulence, and unsteadiness makes cavitation simulation still a challenging issue.

Sarosdy et al. [19] have conducted different kinds of cavitation experiments, such as determining the difference between water cavitation and Freon cavitation. For water cavitation, the interface is clear, and the cavitation strength is more intense. Under similar conditions with Freon cavitation, the cavity and interface is frothy with greater entrainment rates and weaker cavitation intensities. Hord [20] has published comprehensive experimental data on cryogenic cavitation. Pressure and temperature are measured at five probe locations over the geometries under varying inlet conditions. As a result, this experiment is used widely for validating numerical techniques in terms of thermodynamic effects. Kazuki et al [21] have estimated the turbulent heat transfer

coefficient under cryogenic condition, and the value is reduced when the void fraction increases, and it is increased when the turbulent intensity strengthens. They have also observed that the thermodynamic effects on cryogenic cavitation can suppress and delay the development of cavity bubbles.

As for recent experiments regarding the thermal effect of water cavitation, Huang and Zhuang [22] have conducted an experiment on hemispherical projectile, and the working liquid is water around 35˚C. After the facility is turned on, the cavity grows, and the temperature near the cavity drops relative to that of the upstream. It highlights the vaporization as an endothermic process, and hence the temperature will decrease during phase change. Gervone et al. [23] have studied the thermal effects of water at different temperatures at the same cavitation number (NACA0015 hydrofoil). It has been discovered that for 25˚C and 50˚C, the cavity size is comparable. However, water at 70˚C experiences a significant reduction of cavity size because at higher temperatures, such as 70˚C, the absorption of the latent heat at the cavity interfaces increases, reducing the vapor pressure under the saturation value. Besides, the frequency spectrum of pressure is obtained to define different flow regimes for cavitation based on different cavitation numbers, such as traveling cavitation, transition, cloud cavitation, and supercavitation. These regimes can be determined by the difference of maximum and minimum cavity length. Yuka et al. [24] have observed from their experiment that water under room temperature has experienced stronger cavitation phenomenon than that of liquid nitrogen under similar conditions. Besides, under cryogenic conditions, the development of a cavity can encounter more suppression when free stream temperature increases.

Gustavsson et al. [25] have used ‘fluoroketone’ as working liquids instead of cryogenic liquids to display the thermal effects of cavitation. It has been found out that vapor formation was much stronger in fluoroketone than in cold water at similar cavitation number. In other words, the vapor formation occurs at significantly higher cavitation numbers in this thermal-sensible fluid than in water. This trend allows us to display the thermal effects in a safer environment than that of cryogenic liquids.

1.3. RESEARCH MOTIVATIONS AND CURRENT CONTRIBUTIONS

Cavitation for most engineering applications is turbulent, and the interplay between cavitation and turbulence makes the cavitation dynamics even more complicated, and thus the detail dynamics of the phase change is not well understood. In addition, the large density variations across the interface and the thermal effects associated with cryogenic fluids are all challenging issues for cavitation modeling. The objectives of this dissertation are to develop reliable and first-principle-based computational tools. The emphasis is on the unified mixture theory, Navier-Stokes equations and turbulence closures, and cavitation models capable of handling: (a) large density jumps, (b) vapor-liquid mixing processes, (c) formation and departure of cavity and phase change, (d) interface definition and tracking, moving boundary computations, and (e) thermal effects associated with the cryogenic condition in realistic geometry.

Based on this framework, the current contributions are summarized below:

(1) Examine the interplay between turbulence and the cavitation model by changing the inlet turbulent-to-laminar viscosity ratio, and reduce the uncertainties of the eddy viscosity model with a filter-based approach.

Table 1.2 Summary of the literature reviews for cavitation

Category	Papers	Geometry and flow regime	Descriptions	Comments
Unsteadiness and turbulence	[11]	2D hydrofoil with cloud cavitation, $Re=1.4\times10^6$	Cavitation is essentially an unsteady problem with coupling of turbulence, and the unsteady phenomenon will become stronger near the closure region.	Cavitation simulation will be critical near the closure region.
	[12]	2D hydrofoil, sheet/cloud cavitation, $Re=0.8\times10^6$		
	[17]	2D hydrofoil, sheet cavitation, $Re=1.24\times10^6$		
Flow structure	[11]	As introduced before.	Re-entrant jet is the basic mechanism that triggers the shedding, and it will result in unsteadiness	Transport phenomenon is essential for cavitation model, and again, the choice of turbulence closure can affect the flow structure.
	[13]	2D hydrofoil with side wall effect, cloud cavitation, $Re=2.0\times10^6$		
	[14]	2D hydrofoil with cloud cavitation, $Re\sim1.1\times10^6$		
	[15]	2D back step with cloud cavitation, $Re=0.7\times10^6$		
	[16]	2D nozzle with cloud cavitation, $Re\sim10^6$		
Geometry and 3D effect	[13]	As introduced before.	Re-entrant is sensitive to geometry, and from current paper, it will be suppressed by 3D effects	Choice of characteristic length can be critical.
	[18]	Spanwise-variational hydrofoil with cloud cavitation,$Re\sim1.0\times10^6$		
Thermal effects	[19]	Water/Freon over 2D hydrofoil, sheet cavitation, $Re\sim10^6$	Different flow structures will result from different materials, such as water and cryogenic cavitation	Different treatments of cavitation models will be required to simulate water and cryogenic cavitation
	[20]	Cryogenic liquids over 2D hydrofoil, sheet cavitation, $Re\sim10^7$		
	[22]	Water over hemispherical projectile, sheet		
	[23]	Water over 2D hydrofoil, traveling/sheet/cloud/super cavitation,		
	[25]	Fluoroketone over 2D hydrofoil, sheet cavitation, $Re\sim10^7$		

(2) Investigate the cavitation dynamics of the phase change process under the cryogenic condition, and demonstrate the competition between the cavitaion number and the liquid-to-vapor density ratio in cryogenic cavitation.

(3) Utilize surrogate modeling techniques to assess the sensitivity of design variables and improve the performance of a transport-based cryogenic cavitation model systematically.

(4) Investigate the impacts of density effect and filter-based approach on the turbulence closures by assessing the time-dependent flow structures.

(5) Investigate the transport dynamics of the evaporation and condensation for each specific stage within the cavitation process.

BIBLIOGRAPHY

1. Utturkar, Y., Wu, J., Wang, G., Shyy, W.: Recent Progress in Modeling of Cryogenic Cavitation for Liquid Rocket Propulsion. Progress in Aerospace Sciences 41(7), 558-608 (2005)
2. Knapp, R.T., Daily, J.W., Hammitt, F.G.: Cavitation. McGraw-Hill. New York (1970)
3. Brennen, C.E.: Cavitation and Bubble Dynamics. Oxford Engineering & Sciences Series 44, Oxford University Press (1995)
4. Joseph, D.D.: Cavitation in a Flowing Liquid. Phys. Review E 51(3), 1649-1650 (1995)
5. Joseph, D.D.: Cavitation and the State of Stress in a Flowing Liquid. Journal of Fluid Mechanics 366, 367-378 (1998)
6. Lemmon, E.W., McLinden, M.O., Huber, M.L.: REFPROP: Reference Fluid Thermodynamic and Transport Properties. NIST Standard Database 23, version 7.0 (2002)
7. Sonntag, R.E., Borgnakke, C., Wylen, G.J.: Fundamentals of thermodynamics. John Wiley and Sons, Inc (2004)

8. Ruggeri, R.S., Moore, R.D.: Method for prediction of pump cavitation performance for various liquids, liquid temperatures and rotative speeds. NASA TN D-5292 (1969)
9. Goel, T., Zhao, J., Thakur, S., Haftka, R. T., Shyy, W., Zhao, J.: Surrogate Model-Based Strategy for Cryogenic Cavitation Model Validation and Sensitivity Evaluation", Int. J. Numer. Meth. Fluids 58, 969-1007 (2008)
10. Wang, G., Senocak, I., Shyy, W., Ikohagi, T., Cao, S.: Daynamics of Attached Turbulent Cavitating Flows. Progress in Aerospace Sciences 37, 551-581 (2001)
11. Kubota, A., Kato, H., Yamaguchi, H., Maeda, M.: Unsteady Structure Measurement of Cloud Cavitation on a Foil Section Using Conditional Sampling Technique. J. Fluid Eng-T. ASME 111, 204-210 (1989)
12. Leroux, J.B., Astolfi, J.A., Billare, J.Y.: An Experimental Study of Unsteady Partial Cavitation. ASME 26, 94-101 (2004)
13. Kawanami, Y., Kato, H., Tanimura, M., Tagaya, Y.: Mechanism and Control of Cloud Cavitation. J. Fluid Eng-T. ASME 119, 788-794 (1997)
14. Laberteaux, K.R., Ceccio, S.L.: Partial Cavity Flows. Part 1.Cavities Forming on Models without Spanwise Variation. J. Fluid Mech 431, 1–41 (2002)
15. Callenaere, M., Franc, J.P., Michel, J.M., Riondet, M.: The Cavitation Instability Induced by the Development of a Re-entrant Jet. J. Fluid Mech. 444, 223-256 (2001)
16. Gopalan, S., Katz, J.: Flow Structure and Modeling Issues in the Closure Region of Attached Cavitation. Phys. Fluids 12(4), 895-911 (2000)
17. Li, C.Y., Ceccio, S.L: Interaction of Single Travelling Bubbles with the Boundary Layer and Attached Cavitation. J. Fluid Mech. 322, 329-353 (1996)
18. Laberteaux, K.R., Ceccio, S.L.: Partial Cavity Flows. Part 2. Cavities Forming on Test Objects with Spanwise Variation. J. Fluid Mech 431, 43-63 (2002)
19. Sarosdy, L.R., Acosta, A.J.: Note on Observations of Cavitation in Different Fluids. Paper 60-WA-83, ASME Winter Annual Meeting, New York (1961)
20. Hord, J.: Cavitation in Liquid Cryogens II-Hydrofoil. NASA CR-2156 (1973)
21. Kazuki, N., Satoshi, H., Shinichi, T., Yoshiki, Y., Tsutomu, T., Mamoru, O.: Thermodynamic Effects on Cryogenic Cavitation Flow in Orifice. CAV2009, Paper No. 36, Proceedings of the 7th International Symposium on Cavitation, August 17-22, 2009, Ann Arbor, Michigan, USA.
22. Huang, D.G., Zhuang, Y.Q.: Temperature and Cavitation. IMechE 222, 207-211 (2008)
23. Cervone, A., Bramanti, C., Rapposelli, E., Agostino, L.: Thermal Cavitation Experiments on a NACA 0015 Hydrofoil. ASME 128, 326-331 (2006)
24. Yuka, I., Naoya, O., Yoshiki, Y., Toshiaki, I.: Numerical Invetigation of Thermodynamic Effect on Unsteady Cavitation in Cascade. CAV2009, Paper No. 78, Proceedings of the 7th International Symposium on Cavitation, August 17-22, 2009, Ann Arbor, Michigan, USA.
25. Gustavsson, J.P.R., Denning, K.C., Segal, C.: Incipient Cavitation Studied under Strong Thermodynamic Effect. AIAA Journal 47(3), 710-716 (2009)

CHAPTER 2

CAVITATION, TURBULENCE, AND SURROGATE MODELING TECHNIQUES

Due to the interplay between cavitation and turbulence mentioned in the previous chapter, a computational tool consisting of Navier-Stokes equations, turbulence closure, and cavitation models needs to be developed and investigated. Different cavitation models are listed for their merits and weaknesses in Chapter 2.1.

2.1 CAVITATION MODELS

Various cavitation models can be categorized based on how the moving interface and multiphase mixtures are handled: namely, (1) interface tracking method, (2) density-pressure coupling model, and (3) transport models for liquid/mass fraction. Table 2.1 summarizes the overview for these selected cavitation models.

2.1.1 INTERFACE TRACKING METHODS

In this method, Chen and Hesiter [1] and Deshpande et al. [2] have treated the computational domains with individual phases separately by time-wise grid regeneration according to the cavity shape. The pressure inside the cavity is constant, and a wake model is used to handle the cavity closure. This method is insufficient once the cavity is detached. There are alternative approaches available to track interface, including sharp and smooth interface methods [3], using Eulerian, Lagrangian, and hybrid approaches [4].

2.1.2 DENSITY-PRESSURE COUPLING MODELS

In this category, density will be directly coupled with pressure by some specific equation. For Huang and Zhuang [5] and Edward et al. [6], the equation of state is used. Based on continuity, momentum, and energy conservation (even for isothermal cases), a numerical method for cavitating flow is developed without an additional cavitation model or any other assumptions and experiment coefficients. They claim that since the mass and energy transfer between water and vapor affects cavitation dynamics, abandoning the energy conservation is unadvisable. If the pressure is iterated, the saturation temperature can be interpolated, and then the enthalpy and the specific volume along the saturation water and vapor line can be updated. In this way, the iterated enthalpy can determine if the substance is in vapor, liquid, or mixture phase, and each phase has its own equation of state to specify the density. Wang et al. [7] have developed a homogeneous flow model of sheet/cloud cavitation. Strictly speaking, they do not use any additional transport equations for cavitation. Instead, a fifth-order polynomial curve for different phases and flow regime is adopted to describe the relationship between density ratio and pressure coefficient when cavitation occurs. Delannoy and Kueny [8] have utilized the arbitrary barotropic equations to solve the density field. However, these approaches fail to capture some fundamental fluid physics, such as baroclinic vorticity production, which has been shown in an experimental study [9]. In reality, the pressure and density gradients are not always parallel.

These methods discussed above are unable to account for the convection and transport phenomenon of the cavitation bubbles due to the lack of cavitation transport equation; therefore, these models are more suitable when studying an attached cavity.

2.1.3 TRANSPORT-BASED MODELS

A popular homogeneous flow model is developed and utilized by the framework of the transport-based equation method. The cavitation model in this category [10-27] can be generally termed as:

$$\frac{\partial(\alpha_l)}{\partial t} + \frac{\partial(\alpha_l u_j)}{\partial x_j} = m^+ + m^- \tag{2.1}$$

The mixture fluid property can be evaluated based on the liquid-vapor mixture ratios:

$$\varphi_m = \varphi_l \alpha_l + \varphi_v (1 - \alpha_l) \tag{2.2}$$

The source term m^+ and sink term m^- in Equation (2.1) represent condensation and evaporation rates, which could come from the empirical support, interfacial dynamics, and bubble dynamics. The apparent advantage in the transport-based cavitation model is that this model comes from the convective character of equation, which allows modeling of the impact of inertial forces and the detachment or drift of bubbles. Some researchers [10,12,16,17,20] utilized pressure-based methods, and others [14,15,21-25] employed the density-based methods.

2.1.3.1 PHENOMENOLOGICAL MODELS

Merkle et al. [13] and other researchers [10,12,14-17] have modeled the liquid volume fraction α_l (or vapor volume fraction) by the similar sink and source terms, which

regulate the mass transfer between vapor and liquid phases with the empirical constants. The general form of evaporation and condensation rates for this transport-based cavitation model are shown respectively:

$$m^- = \frac{C_{dest}\alpha_l}{t_\infty}\frac{\rho_l}{\rho_v}\frac{\min(0, P-P_v)}{(0.5\rho_l U_\infty^2)} \quad m^+ = \frac{C_{prod}(1-\alpha_l)}{t_\infty}\frac{\max(0, P-P_v)}{(0.5\rho_l U_\infty^2)} \tag{2.3}$$

The conditional statement in the source term m^+ and sink term m^- means evaporation/condensation occurs when pressure is smaller/larger than vapor pressure under the assumption of thermal equilibrium.

In Equation (2.3), C_{dest} and C_{prod} are the empirical constants, U_∞ is the reference velocity scale, and t_∞ is the reference time scale, which is the characteristic length scale L divided by the reference velocity scale U_∞ ($t_\infty=L/U_\infty$. Therefore, the models here are derived for entire bubble clusters, but not a single bubble). For non-cryogenic fluids like water, the constants are specified as C_{dest} =1 and C_{prod} =80 [12,13,13,16,17]. Goel et al. [11] have conducted numerical experimentations for cryogenic liquids. For liquid nitrogen, the constants are chosen as C_{dest} =0.639 and C_{prod} =54.4, and for liquid hydrogen, C_{dest} =0.767 and C_{prod} =54.4 are suggested.

All elements in the evaporation term in Equation (2.3) can be interpreted from physical meaning: (a) only the liquid phase can contribute to evaporation therefore α_l appears; (b) evaporation only occurs when pressure is less than vapor pressure thus $\min(0,P-P_v)/0.5\rho_l U_\infty^2$ is shown in Equation (2.3). This term can be regrouped as $\min(0, C_p+\sigma)$ and essentially represents the cavitation number; (c) The evaporative cooling associated with

thermal effects will be dominated by the density ratio ρ_l/ρ_v. As a result, a smaller free stream cavitation number will have stronger evaporation dynamics in isothermal cases since the density ratio is not changed essentially. For the cryogenic cavitation, the impact of thermal-sensible properties is amplified since the density ratio is smaller; this can cause significant evaporative cooling. Therefore, the cavitation intensity is suppressed for cryogenic cavitation here as described in several experimental/numerical investigations [28-30]. In addition to the cavitation number, the temperature-dependent variation of the density ratio ρ_l/ρ_v will also play an important role. Based upon the physical understanding, this is expected because the thermal effects associated with the larger mass/heat transfer due to smaller density ratio will weaken the cavitation intensity in Equation (2.3).

2.1.3.2 INTERFACIAL DYNAMICS MODELS

To construct the continuity and force balance across the interfaces, Utturkar et al [10] and Senocak and Shyy [16,17] have considered the high Reynolds number approximation and neglected the viscous and surface tension forces:

$$\rho_l(U_{l,n} - U_{I,n}) = \rho_v(U_{v,n} - U_{I,n}) \tag{2.4}$$

$$P_v - P_l = \rho_l(U_{l,n} - U_{I,n})^2 - \rho_v(U_{v,n} - U_{I,n})^2 \tag{2.5}$$

Here, $U_{v,n}$ is the normal component of the vapor velocity moving away from the interface, and $U_{I,n}$ is the normal interfacial velocity.

If the cavitation is essentially isothermal, it is suitable to consider that the phase change takes place between the mixture and vapor phases across clear interfaces by simply replacing the liquid phase with the mixture phase (for cryogenic liquid, the vapor phase

will be replaced instead, due to its distinct flow structures with mushy interfaces [10]). As for the mixture density, Equation (2.6) shows that it can be obtained from liquid volume fraction and liquid/vapor phase density. Furthermore, the following cavitation sink and source term in Equation (2.7) can be obtained by combining Equation (2.4)-(2.6) and normalizing the combined equation with t_∞:

$$\rho_m = \rho_l \alpha_l + \rho_v (1 - \alpha_l) \tag{2.6}$$

$$m^- = \frac{\rho_l \min(P - P_v, 0)\alpha_l}{\rho_v (U_{v,n} - U_{I,n})^2 (\rho_l - \rho_v) t_\infty} \quad m^+ = \frac{\max(P - P_v, 0)(1 - \alpha_l)}{(U_{v,n} - U_{I,n})^2 (\rho_l - \rho_v) t_\infty} \tag{2.7}$$

The choice of the time scale in Equation (2.7) will determine the cavitation dynamics. A systematic investigation is needed to ascertain this aspect. In the present study, it is chosen as L/U_∞ in Equation (2.3) for the entire bubble clusters.

The empirical constants in Equation (2.3) can be replaced by the explicit calculations for the interfacial velocity terms in Equation (2.7). The normal component of the vapor velocity moving away from the interface, $U_{v,n}$, is calculated as:

$$U_{v,n} = \vec{u} \cdot \vec{n}; \qquad \vec{n} = \frac{\nabla \alpha_l}{|\nabla \alpha_l|} \tag{2.8}$$

The normal interfacial velocity, $U_{I,n}$, is zero in steady calculation. However, in unsteady computations, this term needs modeling efforts. Previous studies expressed $U_{I,n}$ in terms of part of the $U_{v,n}$ [16,17]. An alternate method of modeling is also discussed by Utturkar et al. and Wu et al. [10,12]. This method is based on the local variation of liquid volume fraction with time marching, where S_{cv} is the control volume face area, and S_a is the interface area:

$$U_{I,n} = \frac{\Delta \dot{m}}{S_a} = \frac{(\alpha_l(t+\Delta t) - \alpha_l(t)) \cdot S_{CV}}{\Delta t \cdot S_a} \tag{2.9}$$

S_a can be calculated by projecting the control volume face area onto the normal direction of the interface:

$$S_a = \frac{S_{CV}}{|\, n_x / \sqrt{n_x^2 + n_y^2}\,|}, \quad \vec{n} = \frac{\nabla \alpha_l}{|\nabla \alpha_l|} = n_x \vec{i} + n_y \vec{j} \tag{2.10}$$

Despite the eliminations of empirical constants, the choice of time scale and how to compute the velocities of the moving interface will still be crucial.

2.1.3.3 RAYLIEGH-PLESSET EQUATION FOR BUBBLE DYNAMICS

In this approach [18-25], the bubble dynamics can be expressed as a simplified Rayliegh-Plesset equation, which neglects the acceleration of bubble growth, viscous force, and surface tension. The model is based on inertial effects under a high Reynolds number approximation, and it neglects thermodynamic phenomena in the system. The dynamics of the growth of vapor bubbles is modeled by taking the inertial effects of the radius growth rate into account. It assumes the phase change only depends on the pressure difference between liquid and vapor in the surrounding of the bubble. Therefore, the growth rate of the bubble radius R is given by a simplified Rayliegh-Plesset equation:

$$\frac{dR}{dt} = \pm \left(\frac{2}{3} \frac{|P_v - P|}{\rho_l}\right)^{0.5} \tag{2.11}$$

The sign of the radius change rate depends on whether the bubble is growing (evaporation, $P_v > P$) or decaying (condensation, $P_v < P$). As for the vapor volume fraction

α_v, it could be expressed as the combinations of the bubble radius R and the bubble number density n_b:

$$\alpha_v = n_b \frac{4}{3}\pi R^3 \tag{2.12}$$

The cavitation transport equation can be derived as follows:

$$\frac{\partial \alpha_v}{\partial t} + \nabla \cdot (u\alpha_v) = S = \frac{3\alpha_v}{R}\frac{dR}{dt}$$

Therefore, the general form of this category is:

$$\frac{\partial \alpha_v}{\partial t} + \nabla \cdot (u\alpha_v) = \pm \frac{3\alpha_v}{R}\left(\frac{2}{3}\frac{|P_v - P|}{\rho_l}\right)^{0.5} \tag{2.13}$$

Apparently, the spirit of this model in Equation (2.13) is that the local vapor volume fraction is determined by the summation of the increase/decrease volume of every micro bubble, which accounts for evaporation/condensation. In this model, every bubble is assumed to have the same radius inside each specific computational cell, and the number density for each computational cell is the same for the entire space, which is suggested as 10^8 in [18]. In Equation (2.3) and (2.7), where the transport equation comes from empirical support or interfacial dynamics, different sink and source term represent different phase change rates of evaporation and condensation. However, Equation (2.13) accounts for the bubble growth and collapse in one source term. Li et al. [19] and Singhal et al. [20] have used different phase change rates with the additional empirical constants from numerical experiments. Hosangadi et al. [21,22] have used an additional transport

equation to avoid the ad-hoc source term. The additional transport equation is for the net surface area of the bubbles S_v:

$$\begin{aligned}
&\frac{\partial S_v}{\partial t} + \nabla \cdot (S_v u) = 2 S_v \frac{1}{R} \frac{dR}{dt} \\
&\frac{\partial \rho_v \alpha_v}{\partial t} + \nabla \cdot (\rho_v \alpha_v u) = \rho_v S_v \frac{dR}{dt} \\
&S_v = 4\pi R^2 n_b, \;\; \alpha_v = \frac{4}{3}\pi R^3 n_b, \\
&R = 3\alpha_v / S_v, \;\; \frac{dR}{dt} = \pm \left(\frac{2}{3} \frac{|P_v - P|}{\rho_l}\right)^{0.5}
\end{aligned} \tag{2.14}$$

To start the simulation, such as Equation (2.13) and (2.14), the initial value of the bubble number density n_b is needed; it is assumed to be a constant throughout the entire simulation and flow domain. Therefore, after the minimum value of the vapor volume fraction is specified, the initial bubble radius can be calculated from Equation (2.12) to initiate the simulation. As mentioned above, to start the simulations, the bubble number density and the minimum value of the vapor volume fraction are needed as initial conditions for the bubble radius. Different outcomes could result from different initial conditions, especially if the estimated initial bubble radius is too small resulting in the sink/source term being too large. The initial conditions critically impact the simulation's outcome. Additionally, the bubble number density is assumed to be constant throughout the whole simulation, and the bubble radius inside each computational cell for every micro bubble is the same. This means that the interaction between bubbles is neglected, and the assumption could not be true and will limit the accuracy, especially when the bubble density is very high.

Table 2.1 Summary of the numerical methods for cavitation simulations

Cavitation model	**Papers**	**Descriptions**	**Comments**
Interface tracking method	[1,2]	Treat individual phases separately by constant cavity pressure and time-wise grid regeneration.	Hard to deal with the detached cavity.
Specific density and pressure relation	[5-8]	Density and pressure are coupled by equation of state or arbitrary barotropic equation.	Lack of the ability to perform the convection/transport phenomenon and other cavitation behaviors.
Transport equation	[11–17]	Different phase change rates exist for evaporation and condensation together with empirical constants from dimensional arguments.	1. Ability to capture the detached cavity with suitable turbulence mode. 2. Un-universal empirical constants for different fluids
	[11,13,16,17]	Empirical constants can be replaced by the explicit calculations based on the interfacial dynamics.	Improvement needed for the calculations of the moving interface.
	[18-25]	Use Rayliegh-Plesset equation to account for the bubble growth and collapse.	1. Complexity and interplay between the initial bubble radius and simulation results. 2. Accuracy limited by the constant assumption for the bubble number density.

Yao and Morel [26] and Mimouni et al. [27] have also included the transport equation of bubble number density to account for the variation in space and time. However, the introduction of the nucleation theory involves more ad-hoc terms, empirical constants, and complexity to close the equations. Kubota et al. [31] and Xing and Frankel [32] have taken the interaction of bubbles in the subgrid scale into consideration to modify the Rayliegh-Plesset equation for the low bubble number density. However, few researchers have utilized this modified equation; perhaps this is due to the complicated implementation or the limit of improved accuracy.

Overall, in regards to the transport-based cavitation model in Chapter 2.1.3, the accuracy and performance do not have decisive differences as long as an appropriate turbulence model is used. Even though some models claim they can account for more physics, the induced empirical constants will still limit the accuracy as a noise loading.

2.2 TURBULENCE CLOSURES

As mentioned before, the interplay between cavitation and turbulence regarding the unsteadiness and flow structures are important. Therefore, the choice of a turbulence model is also critical.

The highest accuracy for resolving all turbulence scales is Direct Numerical Simulation (DNS). However, it requires a very fine grid resolution proportional to Re^3. Even for the near future, DNS will still be very hard to apply to practical flows due to the high consuming of computer performance. As a standard tool for industrial application,

Reynolds-averaged Navier-Stokes (RANS) takes into account all turbulence scales, which vary from the largest eddies to the Kolmgorov scale, with appropriate turbulence closure. In the Reynolds-averaged equation, the instantaneous flow variables are summations of a mean $\bar{\phi}$ and a fluctuation ϕ'. The average is statistically done for N realizations of the flow domain; therefore the mean of the fluctuation is zero [33-35]:

$$\bar{\phi} = \lim_{N\to\infty} \frac{1}{N} \sum_{n=1}^{N} \phi_n(\vec{x}, t) \tag{2.15}$$

However, for variable density flows, such as cavitation, additional terms will be induced by the products of fluctuations between density and other variables. Hence, Favre-averaging, a density-weighted method, is defined by Dahm [34] and Launder [35] as follows:

$$\tilde{\phi} = \frac{\overline{\rho\phi}}{\rho}; \quad \phi = \tilde{\phi} + \phi''; \quad \overline{\rho\phi''} = 0 \tag{2.16}$$

The Favre-averaged Navier-Stokes equation can be expressed as follows:

$$\frac{\partial \bar{\rho}}{\partial t} + \nabla \cdot (\bar{\rho}\tilde{u}_j) = 0 \tag{2.17}$$

$$\frac{\partial \bar{\rho}}{\partial t} + \nabla \cdot (\bar{\rho}\tilde{u}_i\tilde{u}_j) = -\nabla \bar{P} + \nabla \cdot (\bar{\tau}_{ij} - \overline{\rho u_i'' u_j''}) \tag{2.18}$$

$$\bar{\tau}_{ij} = \mu\left(\frac{\partial \tilde{u}_i}{\partial x_j} + \frac{\partial \tilde{u}_j}{\partial x_i} - \frac{2}{3}\frac{\partial \tilde{u}_k}{\partial x_k}\delta_{ij}\right) + \mu\left(\frac{\partial \overline{u_i''}}{\partial x_j} + \frac{\partial \overline{u_j''}}{\partial x_i} - \frac{2}{3}\frac{\partial \overline{u_k''}}{\partial x_k}\delta_{ij}\right) \tag{2.19}$$

The nonlinear term ($-\overline{\rho u_i'' u_j''}$) representing for the Reynolds stress needs additional modeling. The Boussinesq's gradient transport hypothesis for turbulence closure leads to the following equation:

$$\bar{\tau}_{ij}^{R} = -\overline{\rho u_i'' u_j''} = \mu_T \left(\frac{\partial \tilde{u}_i}{\partial x_j} + \frac{\partial \tilde{u}_j}{\partial x_i}\right) - \frac{2}{3}\delta_{ij}\left(\mu_T \frac{\partial \tilde{u}_k}{\partial x_k} + \bar{\rho} k\right) \tag{2.20}$$

The gradient transport hypothesis in Equation (2.20) is adopted based on the analogy to the molecular transport behavior [33,34].

Finally, the Favre-averaged Navier-Stokes equation is presented in the following form with density replaced by mixture density [16]:

$$\frac{\partial \bar{\rho}_m}{\partial t} + \nabla \cdot (\bar{\rho} \tilde{u}_j) = 0 \tag{2.21}$$

$$\frac{\partial \bar{\rho}_m}{\partial t} + \nabla \cdot (\bar{\rho}_m \tilde{u}_i \tilde{u}_j) = -\nabla \bar{P} + \nabla \cdot (\bar{\tau}_{ij} + \tau_{ij}^{R}) \tag{2.22}$$

$$\bar{\tau}_{ij} + \bar{\tau}_{ij}^{R} = (\mu + \mu_T)\left(\frac{\partial \tilde{u}_i}{\partial x_j} + \frac{\partial \tilde{u}_j}{\partial x_i} - \frac{2}{3}\frac{\partial \tilde{u}_k}{\partial x_k}\delta_{ij}\right) \tag{2.23}$$

As for the turbulence closure, two-equation k-ε model is used [33-35], where k is the turbulent kinetic energy, and ε is turbulent dissipation rate:

$$\frac{\partial(\bar{\rho}_m k)}{\partial t} + \frac{\partial(\bar{\rho}_m \tilde{u}_j k)}{\partial x_j} = P_t - \bar{\rho}_m \varepsilon + \frac{\partial}{\partial x_j}\left[\left(\mu + \frac{\mu_t}{\sigma_k}\right)\frac{\partial k}{\partial x_j}\right] \tag{2.24}$$

$$\frac{\partial(\bar{\rho}_m \varepsilon)}{\partial t} + \frac{\partial(\bar{\rho}_m \tilde{u}_j \varepsilon)}{\partial x_j} = C_{\varepsilon 1}\frac{\varepsilon}{k} P_t - C_{\varepsilon 1}\bar{\rho}_m \frac{\varepsilon^2}{k} + \frac{\partial}{\partial x_j}\left[\left(\mu + \frac{\mu_t}{\sigma_\varepsilon}\right)\frac{\partial \varepsilon}{\partial x_j}\right] \tag{2.25}$$

The production term of turbulent kinetic energy (P_t) is defined as:

$$P_t = \bar{\tau}_{ij}^{R} \frac{\partial \tilde{u}_i}{\partial x_j} \tag{2.26}$$

with $C_{\varepsilon 1}$=1.44, $C_{\varepsilon 2}$=1.92, σ_ε=1.3,σ_k=1.0. The turbulent eddy viscosity is defined as:

$$\nu_T = \frac{C_\mu k^2}{\varepsilon}, \quad C_\mu = 0.09 \tag{2.27}$$

The Large Eddy Simulation (LES) attempts to resolve most of the turbulence scales, and it is often more capable of reproducing large unsteadiness motion of the flow field, resulting in only the small unresolvable scales being modeled. Ruprecht et al. [36] and Germano et al. [37] have used a subgrid-scale model (SGS) to account for the smallest eddy by stress tensor. Also, some researchers, such as Smagorinsky [38], have linked additional transport equations to solve the turbulent kinetic energy k in SGS models with Δ as the filter size and a constant C_s:

$$\nu_T = C_S k^{1/2} \Delta \tag{2.28}$$

In practice, the grid spacing plays a major role in distinguishing the alternative turbulence models. Typically, the grid spacing requirement is more forgiving for the RANS model. For LES, the spatial and temporal resolutions are significantly more stringent with the expectation that most turbulence scales are resolved via direct computations, and only the smallest isotropic scales are molded via subgrid treatments. Obviously, the computational cost of LES is very high. Very Lager Eddy Simulation (VLES) attempts to strike a compromise between RANS and LES.

Various VLES models have been proposed. Essentially, based on the numerical resolutions available in a given computational set-up, it adaptively adjusts the use of the eddy viscosity. In the studies of Ruprecht et al. [36], Fasel et al. [39], and Johansen et al. [40], the general idea is to limit the influence of the eddy viscosity based on the local numerical resolution, essentially forming a combined direct numerical simulation and RANS model. Specifically, the level of the turbulent viscosity is corrected by comparing

the turbulence length scale ($k^{3/2}/\varepsilon$) and the filter size Δ, which is based on the local meshing spacing. The implementation can be described as follows by imposing a filter function f to Equation (2.27):

$$\nu_T = \frac{C_\mu k^2}{\varepsilon} f,\ f = \min(1\ , \frac{\Delta \cdot \varepsilon}{k^{3/2}}) \tag{2.29}$$

If the filter size Δ is large, it will reach RANS limit as shown in Equation (2.27):

$$\nu_T = 0.09 \frac{k^2}{\varepsilon} \tag{2.30}$$

If the filter size is small enough, it will reach LES limit, such as shown in Equation (2.28):

$$\nu_T = 0.09 k^{1/2} \Delta \tag{2.31}$$

For a filter size even smaller than the smallest scale, it eventually becomes DNS.

The choice of filter size for the filter functions above is based on the grid spacing. Fasel et al. [39] and Johansan et al. [40] have selected a homogeneous filter size based on the largest spacing in the computational domain, which avoids further considerations of grid size variation in turbulence transport equation:

$$\Delta = \max(\Delta_{present}, \Delta_{grid}) \tag{2.32}$$

where the value of Δ_{grid} is assigned based on the geometric mean of the maximum mesh sizes in the individual coordinates, and $\Delta_{present}$ is the candidate filter size.

Ruprecht et al. [36] have also taken the computational time step and local velocity into consideration:

$$\Delta = c \cdot \max(|u|\Delta t, \Delta_{grid}) \tag{2.33}$$

In summary, VLES keeps the ability to predict the large unsteady motion and spends less computational cost than that of original LES by utilizing a filter function. In this way, the uncertainties of the turbulence model can be reduced. However, the choice of filter function still can be critical.

Similarly, the detached eddy simulation (DES) has also been used for the modification of the hybrid RANS-LES approach [41-44]. Since the LES is computationally too expensive for practical applications, a two-layer model is used. In the wall region, RANS-type calculations are performed for attached boundary layer, and then at a specified distance from the wall, the computation switches to LES for the detached large eddy. The basic idea is similar to VLES, however, the filter function contains not only the local grid spacing, but also the wall distance. Chauvet et al. [42] have used a transport equation for 'eddy viscosity' derived with a destruction term:

$$Destruction \ \ term = \rho C(\frac{\nu_T}{\tilde{d}})^2 \tag{2.34}$$

where C is the combined function for near-wall corrections, and the filter is placed in the destruction term with a constant C_{DES}:

$$\tilde{d} = \min(d, C_{DES}\Delta) \tag{2.35}$$

Thus, if wall distance d is smaller to the filter size or the local grid spacing Δ near the wall region, RANS behavior is turned-on; if d is larger than Δ, then LES behavior will be activated for a larger destruction term so that the smaller eddy viscosity is obtained.

Some researchers of DES such as Strelets [43] and Home et al. [44] have switched RANS and LES by utilizing the concept of Mentor's SST [45], which blends k-ε and k-ω models for different zones. The filter is placed on the destruction term in the transport equation for the turbulent kinetic energy k:

$$Destruction\ term = C \cdot k\omega \max(1, \frac{\sqrt{k}}{CC_{DES} \cdot \omega\ \Delta}) \tag{2.36}$$

Overall, it can be observed that VLES switches between RANS and LES based on the local physical resolution; for DES, both resolution and wall distance could be regarded as important factors.

To account for the large density jump caused by cavitation, Hosangadi et al. and Singhal et al. [15,20] have considered the compressibility of mixture phases, and modified the eddy viscosity by a density correction function (DCM) as:

$$\nu_T = \frac{C_\mu k^2}{\varepsilon} f_{DCM},\ \ C_\mu = 0.09,\ f_{DCM} = \frac{\rho_v + (\alpha_l)^n(\rho_l - \rho_v)}{\rho_v + \alpha_l(\rho_l - \rho_v)} \tag{2.37}$$

With such a treatment, the eddy viscosity is reduced based on the mixture density.

2.3 NUMERICAL METHODS

The Navier-Stokes equations are well established for multi-phase fluid dynamics by Senocak and Shyy [16,17], Wu et al [12], and Kunz et al [14]. For example, in a recent study by Tseng and Shyy [46], they have solved the set of governing equations for cavitation under the homogeneous-fluid modeling, consisting of the conservative form of the Favre-averaged Navier-Stokes equations (Equation (2.21)-(2.23)), the enthalpy-based energy equation for cryogenic cavitation, the k-ε two-equation turbulence closure (Equation (2.24) and (2.25)), and a transport equation for the liquid volume fraction (Equation (2.3) and (2.7)). Besides the baseline k-ε two-equation turbulence closure, a filter-based model is also used (Equation (2.29) and (2.32)).

Senocak and Shyy [16,17] have reported detailed numerical procedures for the cavitation model and associated fluid dynamics equations based on a modified pressure-based approach to account for large density jumps as well as thermal effects. In their work, to prevent the oscillations under sharp gradients caused by the phase change while preserving second-order accuracy elsewhere, the controlled variation scheme (CVS) [16,33] is applied to discretize the convection scheme.

Besides the Navier-Stokes model, one can employ kinetics-based approaches, such as the lattice Boltzmann method [5,47,48]. In the context of the LBE method for isothermal immiscible multiphase flow, various interfacial characteristics can be incorporated into the LBE model utilizing a kinetic framework. Employing the diffuse-interface approach [49], the LBE multiphase method does not track the interface explicitly and can handle

complex phase topology, including breakup and merger. The phase interface is modeled as a thin zone spanning several lattices over which the fluid/flow properties vary smoothly. The surface tension is modeled as a volumetric force that acts on the fluids only over a thin zone across the interface. The volumetric force is represented in the spatial density gradient (or index function) manner. For immiscible multiphase flows without phase change, this interface modeling in the LBE requires that the interface thickness does not smear off, and dispersed phase mass is conserved, with long time evolution. The numerical methods used in this modeling should also be numerically stable for large flow/fluid property jumps across the interface.

Some of the popular LBE multiphase models include Shan-Chen's (hereinafter referred as SC) inter-particle potential mode [50,51], free energy model by Swift et al. [52], He-Shan-Doolen's model (hereinafter referred to HSD model) from kinetic theory of dense fluid [53], and an extension by He-Chen-Zhang (the HCZ model) [54]. In the SC model, the interface is modeled through non-local fluid particle interaction. It is incorporated into the lattice Boltzmann equation through an additional forcing term added to the macroscopic velocity [50,51]. The SC model has been successfully applied in some multiphase flow simulations, including stationary droplet [50], oscillation of a capillary wave [51], and drag and virtual mass forces in bubbly suspensions [55]. However, in this model, temperature is not consistent with the thermodynamics definition, the surface tension coefficient can not be freely chosen according to the fluid property, and the viscosities of all phases must be the same. The free energy model of Swift et al. [52] does not suffer from such limitations as in SC model. It has been successfully used to simulate

some multiphase flows, such as stationary bubble/droplet, capillary wave, and phase separation in a narrow capillary [52], two-dimensional bubble in Poiseuille flow [56]. However the Galilean invariance can not be maintained in this model [57]. In the HSD model the kinetic theory of dense gases is applied to model phase segregation and surface tension. It overcomes the limitations of the SC model while maintaining the Galilean invariance. The major drawback of the HSD model is its numerical instability for flows with large gradients arising from interfacial forcing terms. This drawback of the HSD model, shared by all LBE multiphase models, has not been adequately addressed in the literature. In the HCZ model, introducing a second lattice Boltzmann equation alleviates the numerical instability. In this second lattice Boltzmann equation, the large gradient term is multiplied by a term that is proportional to the Mach number. The first lattice Boltzmann equation is used to track interfaces, and its function is similar to that of a fixed grid (Eulerian) method, such as the level set method and the volume-of-fluid method. With the improved numerical stability, the Rayleigh-Taylor instability with density ratio up to about 20 [54], and the two-phase Rayleigh-Benard convection with a deformable interface [58] have been successfully simulated using the HCZ model. The computational results also show that the HCZ model is comparable in accuracy with the macroscopic CFD method [57]. The detailed assessments for these three major LBE multiphase models can be found in Nourgaliev et al.'s work [57].

Recently these LBE multiphase models have been extended to flows with large density ratios. Inamuro et al. [59] used free energy model with a projection method for pressure correction to simulate multiphase flows with large density ratio. Zheng et al. [60] also

used free energy model, and two lattice Boltzmann equations for flows with large density ratios, like those in the HCZ model, to capture interface and represent momentum evolution. Lee and Lin's model [49] for multiphase flows with large density ratio differs only slightly from the HCZ model. Instead of using index function, Lee and Lin directly used density as the macroscopic variable calculated from the interface-capturing lattice Boltzmann equation. They also used a potential form for surface tension formulation and hybrid discretizations for the forcing terms.

For cavitating flow computations, the LBM approach offers potential opportunities for further development. At this point, the LBM approach can not handle the complexity and property jumps as well as the Navier-Stokes approach.

2.4 SURROGATE MODELS

The surrogate-based approach is used later in Chapter 4 to assess the importance of Merkle's phenomenogical cavitation model parameters, namely C_{dest} and C_{prod} and the uncertainties of material properties, such as vapor phase density and latent heat. Through a surrogate-based approach, one can utilize the global sensitivity analysis (GSA) and seek the optimal design.

Surrogate models can be obtained by using the available data generated from selected design points, and hence offer an effective approximation with a low cost especially when computer simulations and experiments are expensive. Surrogate models are constructed first by the limited samples generated using systematic approaches. In

addition, surrogate models provide a global, not local, view of the objective functions with respect to the design variables. Surrogate-based approaches are widely used in thermal-fluid and energy systems design optimization, as exemplified by the model parameter calibration for cryogenic cavitation modeling [11], dielectric barrier discharge plasma actuator performance characterization [61], flapping wing aerodynamic analysis [62], and the effect of particle shape and cycling rate on stress and heat generation of Li-ion batteries [63].

The key steps of surrogate modeling are illustrated in Figure 2.1, which includes designing experiments, running numerical simulations, conducting experimental measurements, constructing surrogate models, and validating and further refining the models if necessary [61,64,65].

By balancing the representative of the samples and the cost of numerical simulation, a more efficient approach is desired. Latin Hypercube sampling (LHS) provides a random sampling but ensures a stratified sample within the full range of each dimension of the sample space [66]. Although LHS can give a representative sample inside the design ranges, it can not guarantee to cover the extrema on the boundary of the design space due to its randomness. This issue could become crucial, especially when there may be critical interest in the boundary. As an alternative method, face-centered composite design (FCCD) can include the face-centered points and vertices of the design hypercube [67]. One can blend LHS and FCCD to obtain more representative and comprehensive samples, including the interior and the boundary of the design space.

After acquiring information by simulation or experimental results on the samples, surrogate models can be constructed. The commonly used surrogate models include polynomial response surface (PRS, [67]) kriging (KRG, [68]), radial basis neural network (RBNN, [69]), and a weighted average surrogate by using the previous three models (PWS, [11,65,70]). Further details of each model can also be found in ref. [71]. One should note that it is not possible to know which surrogate model will fit best for approximation beforehand, so it is necessary to construct multiple surrogate models.

PRS approximates the objective function as a linear combination of polynominal basis functions. An example for the second order polynomial response surface is shown below, where coefficients β are selected by minimizing the prediction error with a least squares method [67]:

$$\hat{f}(\mathbf{x}) = \beta_0 + \sum_i \beta_i x_i + \sum_i \sum_j \beta_{ij} x_i x_j \,, \tag{2.38}$$

For KRG, the prediction is approximated by a sum of a polynomial regression model $\sum_i \beta_i f_i(\mathbf{x})$ for a large scale variation and a systematic departure $Z(\mathbf{x})$ for a small scale variation:

$$\hat{f}(\mathbf{x}) = \sum_i \beta_i f_i(\mathbf{x}) + Z(x) \tag{2.39}$$

The systematic departure components are given by a function of distance between the locations under consideration, and a Gaussian function is used in this study [68].

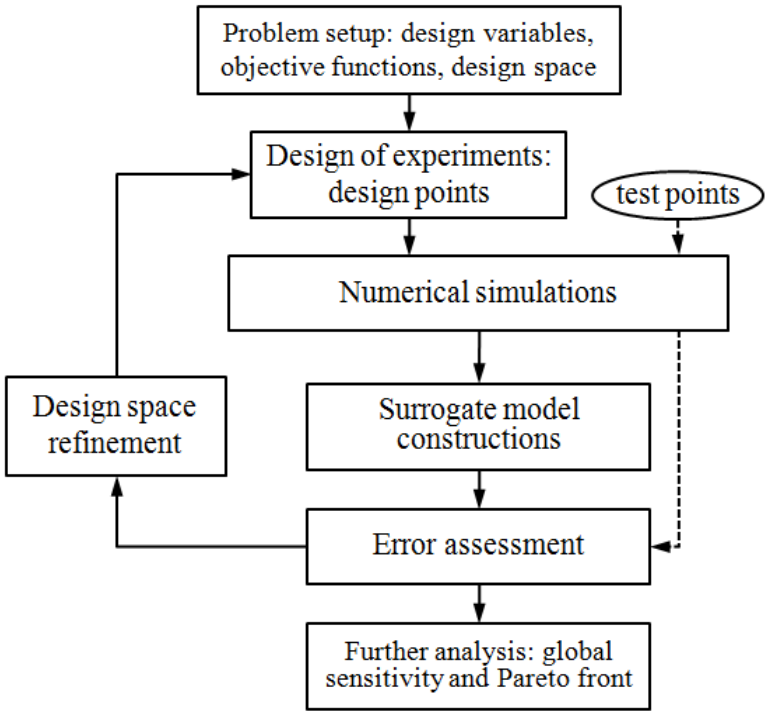

Figure 2.1: Flowchart for the surrogate-based modeling framework (adopted from [61])

A radial-basis neural network model utilizes a linear combination of radial basis functions a_i(x), also known as neurons, to approximate response functions:

$$\hat{f}(\mathbf{x}) = \sum_i w_i a_i(\mathbf{x}); \quad a_i(\mathbf{x}) = e^{-(\|S_i - X\| b)^2} . \tag{2.40}$$

$\|S_i - X\|$ is the distance to the i^{th} radial basis function. The number of neurons and associated weights are determined by satisfying the user-defined error. Parameter b is inversely related to a user-defined parameter referred to as the 'spread constant.' The spread constant controls the response of the radial basis function [69].

Weighted average surrogate models combine information from multiple individual surrogates via a weighting scheme to reduce uncertainties based on the PRESS (will be introduced in next page) values of the individual surrogates. Further details of weighting strategies for multiple surrogates can be found in ref. [65,70].

In order to assess the performance and select appropriate surrogate models, systematic methods to evaluate the accuracy are required. One common strategy is to obtain simulation data at additional test points besides original samples, and then compare the prediction errors between the surrogate model and simulation at these test points. While this method is easy to use and is useful for validation, it is only local and limited by the number of test points and the corresponding locations. Furthermore, the prediction error sum of squares (PRESS) can also be computed. PRESS is computed directly from the training data by summing the "leave-one-out" prediction errors at all data points. The "leave-one-out" prediction error is defined as the prediction error at a particular point

using the surrogate model constructed from all other remaining data points. In this study, we use the PRESS RMS value as the basis of evaluation and comparison:

$$\text{PRESS RMS} = \sqrt{\frac{1}{N_s}\sum_{i=1}^{N_s}(y_i - \hat{y}_i^{(-i)})^2} \tag{2.41}$$

where N_s is the number of training points, y_i is the predicted value at training point i based on the construction of a surrogate model from all original samples, and $\hat{y}_i^{(-i)}$ is the predicted value determined by leaving point i out and using the remaining N_s-1 training points as samples [65,70,72].

After validation of the surrogate model, the global sensitivity analysis [73] can be conducted to study the importance of design variables. The main concept of the global sensitivity analysis is to quantify the variation of the objective functions in terms of design variables. The main factor is the fraction of the total variance of the objective function contributed by a particular variable itself. Besides the sum of the main factors, the total effect also includes contribution of all partial variances due to interaction between the multiple variables. A surrogate-based objective function can be decomposed as a sum of functions of individual variables and interactions of variables:

$$f(\mathbf{x}) = f_0 + \sum_i f_i(x_i) + \sum_{i<j} f_{ij}(x_i, x_j) + \cdots + f_{12\ldots N}(x_1, x_2, \ldots, x_N). \tag{2.42}$$

The partial variance V_i can be computed by integrating f_i within its design range of the i^{th} design variable, and V_{ij} can be evaluated as an interaction between i^{th} and j^{th} design variables by integrating f_{ij} and then subtracted by V_i and V_j. A similar process can be applied to V_{ijk} and so on. Thus V_i, V_{ij}, V_{ijk} $\cdots$ represent the partial contribution of the corresponding independent variables or set of variables to the total variance and provide

an indication of their relative importance. The total variance $V(f)$ can be obtained by the sum of all the partial variances with N_v as the number of design variables:

$$V(f) = \sum_{i=1}^{N_v} V_i + \sum_{1 \le i,j \le N_v} V_{ij} + \ldots + V_{1 \ldots N_v} . \tag{2.43}$$

The main factor index of variable x_i is defined as

$$S_i^{\text{main}} = \frac{V_i}{V(f)} \tag{2.44}$$

The total effect index of variable x_i is defined as

$$S_i^{\text{total}} = \frac{V_i + \sum_{j, j \neq i} V_{ij} + \sum_{j, j \neq i} \sum_{k, k \neq i} V_{ijk} + \ldots}{V(f)} . \tag{2.45}$$

If insignificant design variables exist, then global sensitivity can be utilized for dimension reductions. Furthermore, surrogate models can be used to acquire optimal objective function. For two-objective optimization, a Pareto front can be generated to identify the tradeoffs between two objective functions. These details will be discussed in Chapter 4.3.

BIBLIOGRAPHY

1. Chen, Y., Hesiter, S. D.: A Numerical Treatment for Attached Cavitaition. J. Fluids Eng 116, 613-618 (1994)
2. Deshpande, M., Feng, J., Merkle, C.L.: Numerical Modeling of the Thermodynamic Effects of Cavitation: J. Fluids Eng 119, 420-427 (1997)
3. Ye, T., Mittal, R., Udaykumar, H.S., Shyy, W.: An accurate Cartesian grid method for viscous incompressible flows with complex immersed boundaries. Journal of Computational Physics 156. 209-240 (1999)

4. Chen, S., Doolen, D.: Lattice Boltzmann method for fluid flows. Annual Review of Fluid Mechanics 30, 329-364 (1998)
5. Huang, D., Zhuang, Y., Cai, R.: A Computational Method for Cavitational Flows Based on Energy Conservation. IMechE 207, 1333-1338 (2007)
6. Edward, J.R., Franklin, R.K., Liou, M.S.: Low-diffusion Flux-splitting Methods for Real Fluid Flows with Phase Transition. AIAA Journal 38(9), 1624-1633, (2000)
7. Wang, G., Ostoja-Starzewski, M.: Large Eddy Simulation of a Sheet/Cloud Cavitation on a NACA0015 Hydrofoil. Mathematical Modeling 31, 417–447 (2006)
8. Delannoy, Y., Kueny, J.L.: Cavity Flow Prediction Based on the Euler equations. ASM Cavitation and Multiphase Flow Forum. ASME-FED 98, 153-158 (1990)
9. Gopalan, S., Katz, J.: Flow Structure and Modeling Issues in the Closure Region of Attached Cavitation. Phys. Fluids 12(4), 895-911 (2000)
10. Utturkar, Y., Wu, J., Wang, G., Shyy, W.:Recent Progress in Modeling of Cryogenic Cavitation for Liquid Rocket Propulsion. Progress in Aerospace Sciences 41(7), 558-608 (2005)
11. Goel, T., Zhao, J., Thakur, S., Haftka, R. T., Shyy, W., Zhao, J.: Surrogate Model-Based Strategy for Cryogenic Cavitation Model Validation and Sensitivity Evaluation", Int. J. Numer. Meth. Fluids 58, 969-1007 (2008)
12. Wu, J.Y., Wang, G.Y., Shyy, W.: Time-dependent Turbulent Cavutating Flow Computations with Interfacial Transport and Filter-based Models. International Journal for Numerical Methods in Fluids 49(7), 739-761 (2005)
13. Merkle, C.L., Feng, J., Buelow, P.E.O.: Computational Modeling of Sheet Cavitation. Proc. 3rd International Symposium on Cavitation, Grenoble, France 1998.
14. Kunz, R.F., Boger, D.A., Stinebring, D.R., Chyczewski, T.S., Lindau, J.W., Gibeling, H.J., Venkateswaran, S., Govindan, T.R: A preconditioned Navier –stokes method for two phase flows with application to cavitation prediction. Comput. Fluids 29, 849-875 (2000)
15. Hosangadi, A., Ahuja, V.: A Numerical Study of Cavitation in Cryogenic Fluids. Journal of Fluids Engineering 127, 267-281 (2005)
16. Senocak, I., Shyy, W.: Interfacial Dynamics-Based Modeling of Turbulent Cavitating Flows, Part-1: Model Development and Steady-State Computations. Int. J. Numer. Meth. Fluids 44, 975-995 (2004)
17. Senocak, I., Shyy, W.: Interfacial Dynamics-Based Modeling of Turbulent Cavitating Flows, Part-2: Time-Dependent Computations. Int. J. Numer. Meth. Fluids 44, 997-1016 (2004)
18. Ha, C.T., Park, W.G., Merkle, C.L.: Multiphase Flow Aanlysis of Cylinder Using a New Cavitation Model. CAV2009, Paper No. 99, Proceedings of the 7th International Symposium on Cavitation, August 17-22, 2009, Ann Arbor, Michigan, USA.

19. Li, X., Wang, G., Yu, Z., Shyy, W.: Multiphase Fluid Dynamics and Transport Processes of Low Capillary Number Cavitating Flows. Acta Mechanica Sinica 25, 161-172 (2008)
20. Singhal, A.k., Li, H., Athavale, M.M., Jiang, Y., Mathematical Basis and Validation of the Full Cavitation Model. J. Fluids Eng 124(3), 617-625 (2002)
21. Hosangadi, A., Ahuja, V.A.: Numerical of Cavitation in Cryogenic Fluids Part II; New Unsteady Model for Dense Cloud. Cavitation. 6th International Symposium on Cavitation, Wageningen, Netherlands. Sep. 2006.
22. Hosangadi, A., Ahuja, V., Ungewitter, R.J.: Simulations of Rotational Cavitation Instabilities in the SSME LPFP Inducer. 43rd AIAA/ASME/SAE/ASEE Joint Propulsion Conference & Exhibit;1-16. 2007.
23. Giorgi, M.G.D., Ficarella, A., Chiara, F., Laforgia, D.: Experimental and Numerical Investigations of Cavitating Flows. 35th AIAA Fluids Dynamics Conference and Exhibit, Toronto, Ontario Canada, Jun. 2005.
24. Aliabadi, S., Tu, S.Z., Watts, M.D.: Simulation of Hydrodynamic Cavitating Flows Using Stabilized Finite Element Method. 43th AIAA Aerospace Science Meeting and Exhibit, Reno, Nevada, Jan. 2005.
25. Tani, N., Nagashima, T.: Numerical Analysis of Cryogenic Cavitating Flow on Hydrofoil-Comparison between Water and Cryogenic Fluids. 4th International Conference on Launcher Technology, Liege, Belgium, December 3-6. 2002.
26. Yao, W., Morel, C.: Volumetric Interfacial Area Prediction in Upward Bubbly Two-Phase Flow. International Journal of Heat and Mass Transfer 47, 307-328 (2004)
27. Mimouni, S., Boucker, M., Lavieville, J., Guelfi, A., Bestion, D.: Modeling and Computation of Cavitation and Boiling Bubbly Flows with the NEPTUNE_CFD Code. Nuclear Engineering and Design 238, 680-692 (2008)
28. Sarosdy, L.R., Acosta, A.J.: Note on Observations of Cavitation in Different Fluids. Paper 60-WA-83, ASME Winter Annual Meeting, New York (1961)
29. Kazuki, N., Satoshi, H., Shinichi, T., Yoshiki, Y., Tsutomu, T., Mamoru, O.: Thermodynamic Effects on Cryogenic Cavitation Flow in Orifice. CAV2009, Paper No. 36, Proceedings of the 7th International Symposium on Cavitation, August 17-22, 2009, Ann Arbor, Michigan, USA.
30. Yuka, I., Naoya, O., Yoshiki, Y., Toshiaki, I.: Numerical Invetigation of Thermodynamic Effect on Unsteady Cavitation in Cascade. CAV2009, Paper No. 78, Proceedings of the 7th International Symposium on Cavitation, August 17-22, 2009, Ann Arbor, Michigan, USA.
31. Kubota, A., Kato, H., Yamaguchi, H.: A New Modeling of Cavitating Flows: A Numerical Study of Unsteady Cavitation on a Hydrofoil Section. J. Fluids Mech 240, 59-96 (1992)
32. Xing, T., Frankel, S.H.: Effect of Cavitation on Vortex Dynamics in a Submerged Laminar Jet. AIAA Journal 40, 2266-2276 (2002)

33. Shyy, W., Thakur, S.S., Ouyang, H., Liu, J., Blosch, E.: Computational Techniques for Complex Transport Phenomenon. Cambridge University Press (2007)
34. Dahm, W.J.A.: Introduction to Turbulent Flows, Physical Concept, Statistical Theory, and Engineering Modeling. University of Michigan (2007)
35. Launder, B.E., Spalding, D.B.: The Numerical Computation of Turbulent Flow. Comp. Meth. Appl. Mech. Eng. 3, 269-289 (1974)
36. Ruprecht, A., Helmrich, T., Buntic, I.: Very Large Eddy Simulation for the Prediction of Unsteady Votex Motion. Conference on Modeling Fluid Flow (CMFF'05), The 12th International Conference on Fluid Flow Technologies. Budapest, Hungary, Sept 3-6, 2005.
37. Germano, M., Piomelli, U., Moin, P., Cabot, W.H.: A Dynamic Subgrid-Scale Eddy Viscosity Model. Physics of Fluids A 3(7), 1760-1765 (1991)
38. Smagorinsky, J., General Circulation Experiments with the Primitive Equations 1. The Basic Experiment. Monthly Weather Review 91(3), 99-164 (1963)
39. Fasel, H.F., Seidel, J., Wernz, S.: A Methodology for Simulations of Complex Turbulent Flows. J. of Fluids Eng 124, 933-942 (2002)
40. Johansen, S.T., Wu, J.Y., Shyy, W.: Filter Based Unsteady RANS Computational. International Journal of Heat and Fluid Flow 25, 10-21 (2005)
41. Shur, M.L., Spalart, P.R., Strelets, M.H., Travin, A.K.: A Hybrid RANS-LES Approach with Delayed-DES and Wall-Modeled LES Capability. International J. of Heat and Fluid Flow 29, 1638-1649 (2008)
42. Chauvet, N., Deck, S., Jacquin, L.: Zonal Detached Eddy Simulation of a Controlled Propulsive Jet. AIAA Journal 45(10), 2458-2473 (2007)
43. Strelets, M.: Detached Eddy Simulation of Massively Separated Flows. AIAA 2001-0879 (2001)
44. Home, D., Lightstone, M.F., Hamed, M.S.: Validation of DES-SST Based Turbulence Model for a Fully Developed Turbulent Channel Flow Problem. Numerical Heat Transfer, Part A. 55, 337-361 (2009)
45. Menter, F.R.: Zonal Two Equation k-ω Turbulence Models for Aerodynamic Flows. AIAA Paper 93-2906 (1993)
46. Tseng, C., Shyy, W,: Modeling for isothermal and cryogenic cavitation, Int. J. Heat Mass Transfer 53, 513-525 (2010)
47. Yu, D., Mei, R., Luo, L., Shyy, W.: Viscous Flow Computations with the Method of Lattice Boltzmann Equation. Progress in Aerospace Sciences,39, 329-367 (2003)
48. Mei, R., Yu, D., Shyy, W., Luo, L.S.: Force Evaluation in the Lattice Boltzmann Method Involving Curved Geometry. Physical Review E 65, 1-14 (2002)
49. Lee, T., Lin, C.: A stable discretization of the lattice Boltzmann equation for simulation of incompressible two-phase flows at high density ratio. Journal of Computational Physics 206, 16-47 (2005)

50. Shan, X., Chen, H.: Lattice Boltzmann model of simulating flows with multiple phases and components. Physical Review E 47, 1815-1819 (1993)
51. Shan, X., Chen, H.: Simulation of non-ideal gases and liquid-gas phase transitions by the lattice Boltzmann equation. Physical Review E 49, 2941-2948 (1994)
52. Swift, M., Osborn, W., Yeomans, J.: Lattice Boltzmann simulation of nonideal fluids. Physical Review Letter 75, 830-833 (1995)
53. He, X., Shan, X., Doolen, G.D.: A discrete Boltzmann equation model for non ideal gases. Physical Review E 57, R13-R16 (1998)
54. He, X., Chen, S., Zhang, R.: A lattice Boltzmann scheme for incompressible multiphase flow and its application in simulation of Rayleigh-Taylor instability. Journal of Computational Physics 152, 642-663 (1999)
55. Sankaranarayanan, K., Shan, X., Kevrekidis, I.G., Sundaresan, S.: Analysis of drag and virtual mass forces in bubbly suspensions using an implicit formulation of the lattice Boltzmann method. Journal of Fluid Mechanics 452, 61-96 (2002)
56. Holdych, D.J., Georgiadis, J.G., Buckius, R.O.: Migration of a van der Waals bubble: lattice Boltzmann formulation. Physics of Fluids 13, 817-825 (2001)
57. Nourgaliev, R., Dinh, T., Theofanous, T., Joseph, D.: The lattice Boltzmann method: theoretical interpretation, numerics and implications. International Journal of Multiphase Flow 29, 117-169 (2003)
58. Chang, Q., Iwan, J., Alexander, D.: Application of the lattice Boltzmann method to two-phase Rayleigh-Benard convection with a deformable interface. Journal of Computational Physics 212, 473-486 (2006)
59. Inamuro, T., Ogata, T., Tajima, S., Konishi, N.: A lattice Boltzmann method for incompressible two-phase flows with large density difference. Journal of Computational Physics 198, 628-644 (1998)
60. Zheng, H.W., Shu, C., Chew, Y.T.: A lattice Boltzmann model for multiphase flows with large density ratio. Journal of Computational Physics 218, 353-371 (2006)
61. Cho, Y.C., Jayaraman, B., Viana, F.A.C., Haftka, R.T., and Shyy, W.: Surrogate Modeling for Characterizing the Performance of Dielectric Barrier Discharge Plasma Actuator, 46th AIAA Aerospace Sciences Meeting and Exhibit, January 7-10, 2008, Reno, Nevada.
62. Trizila, P., Kang, C.K., Visbal, M., and Shyy, W.: A Surrogate Model Approach in 2D versus 3D Flapping Wing Aerodynamic Analysis, 12th AIAA/iSSMO Multidisciplinary Analysis and Optimization Conference, Spetember 10-12, 2008, Victoria, British Columbia, Canada.
63. Du, W., Gupta, A., Zhang, Z., Sastry, A.M., and Shyy, W.: Effect of cycling rate, particle size and transport properties on lithium-ion cathode performance, Int. J. Heat Mass Transfer 53, 3552-3561 (2010)
64. Madsen, J.I., Shyy, W., and Haftka, R.T.: Response Surface Techniques for Diffuser Shape Optimization, AIAA Journal, 38, 1512-1518 (2000).

65. Goel, T., Vaidyanathan, R., Haftka, R.T., Shyy, W., Queipo, N.V., and Tucker, K.: Response Surface Approximation of Pareto Optimal Front in Multi-Objective Optimization, Computer Methods in Applied Mechanics and Engineering, 196, 879–893 (2007).
66. McKay, M.D., Beckman, R.J., and Conover, W.J.: A Comparison of Three Methods of Selecting Values of Input Variables in the Analysis of Output from a Computer Code, Technometrics 21, 239-245 (1979)
67. Myers, R.H., Montgomery, D.C.: Response Surface Methodology, John Wiley, Sons, Inc (1995)
68. Matheron, G.: Principles of Geostatistics. Economic Geology 58, 1246-1266 (1963)
69. Orr, M.J.L.: Introduction to Radial Basis Function Networks, Center for Cognitive Science, Edinburg University, EH 9LW, Scotland, UK. 1996. http://www.anc.ed.ac.uk/~mjo/rbf.html
70. Goel, T., Haftka, R.T., and Shyy, W.: Comparing error estimation measures for polynomial and kriging approximation of noise-free functions, Struct. Multidisc. Optim. 38, 429-442 (2009)
71. Queipo, N.V., Haftka, R.T., Shyy, W., Goel, T., Vaidyanathan, R., and Tucker, P.K.: Surrogate-based analysis and optimization, Prog. Aero. Sci. 41, 1-28 (2005)
72. Viana, F.A.C., Haftka, R.T., and Steffen, V.: Multiple Surrogates: How Cross-Validation Errors Can Help Us to Obtain the Best Predictor, Structural and Multidisciplinary Optimization 39, 439-457 (2009)
73. Sobol, I.M.: Sensitivity Analysis for Nonlinear Mathematical Models. Mathematical Modeling & Computational Experiment 1(4), 407-414 (1993)

CHAPTER 3

ISOTHERMAL AND CRYGENIC CAVITATION UNDER ATTACHED CONDITIONS

In this Chapter, the simulation results are categorized as isothermal and cryogenic cavitation. In the first part, the sensitivity of eddy-to-laminar viscosity ratio at the inlet has been examined under the isothermal condition by utilizing the filter-based approach. In the second part, the competing effects between cavitation number and liquid-to-vapor density have been demonstrated under the cryogenic condition. The simulations shown in this Chapter are based on the steady-state computation since the cavity is still attached in the given flow conditions.

3.1 MODELING OF ISOTHERMAL CAVITATION

Wu et al. [1], Hosangadi and Ahuja [2] and Li [3] have suggested that the RANS model will produce too much eddy viscosity and sometimes will dissipate the unsteadiness and fail to capture the large periodic motions of turbulent cavitating flow. As a result, the importance of LES/DES calculations or a reasonable methodology to reduce eddy viscosity is desirable, even for steady-state computation [4].

Based on the eddy-to-laminar viscosity ratio at the inlet, $\mu_T/\mu_L|_{inlet}$, the inlet turbulent quantities can be given as follows:

$$k = \frac{3}{2}(U_\infty I)^2 \quad \varepsilon = \frac{C_\mu k^2}{\nu_L(\mu_T / \mu_L\big|_{inlet})} \tag{3.1}$$

where I is turbulence intensity, which is 0.02. Without experimental guidance, the inlet conditions are selected to allow the eddy-to-laminar viscosity ratio at the inlet, $\mu_T/\mu_L|_{inlet}$, to vary. There are two geometries simulated for water under isothermal conditions: a hemispherical projectile with the experimental measurements by Rouse and McNown [5] (Figure 3.1(a), number of grid points=7.8×10^3) and the NACA66MOD hydrofoil with the experimental measurements by Shen and Dimotakis [6] (Figure 3.1(b), number of grid points=3.3×10^4). The phenomenological cavitation model used in this Chapter is based on a study of Merkle et al. [7] with C_{dest} =1 and C_{prod}=80 as shown in Equation (2.3):

$$m^- = \frac{C_{dest}\alpha_l}{t_\infty}\frac{\rho_l}{\rho_v}\frac{\min(0, P-P_v)}{(0.5\rho_l U_\infty^2)} \quad m^+ = \frac{C_{prod}(1-\alpha_l)}{t_\infty}\frac{\max(0, P-P_v)}{(0.5\rho_l U_\infty^2)} \tag{2.3}$$

For the hemispherical projectile, an axisymmetric case, the Reynolds number is 1.36×10^5, and the cavitation number σ_∞ is 0.4. There is no information regarding the inlet turbulent variables, and three different inlet turbulent quantities are presented here. With turbulence intensity=0.02, the dissipation rate is adjusted, resulting in the inlet eddy-to-laminar viscosity ratio of 1.5×10^2, 5×10^2, and 10^3, and the effective Reynolds number (based on the eddy viscosity) is 900, 270, and 136, respectively. For the NACA66MODE hydrofoil (angle of attack of 4°), the Reynolds number and the cavitation number σ_∞ are 2×10^6 and 0.91, respectively. In this case, the inlet eddy-to-laminar viscosity ratio is assigned as 10^3, 2×10^3, and 10^4 respectively, and the corresponding effective Reynolds

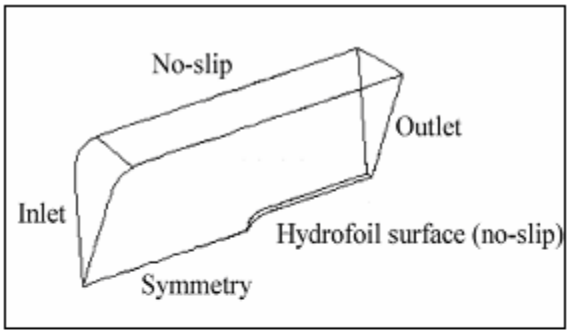

(a) Hemi. projectile [5]

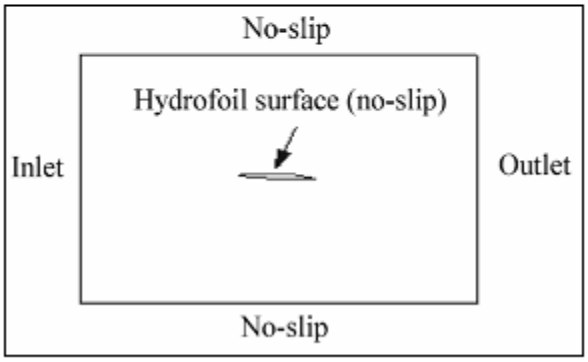

(b) NACA66MOD hydrofoil [6]

Figure 3.1 Schematic of the geometries and the boundary conditions of the isothermal cases.

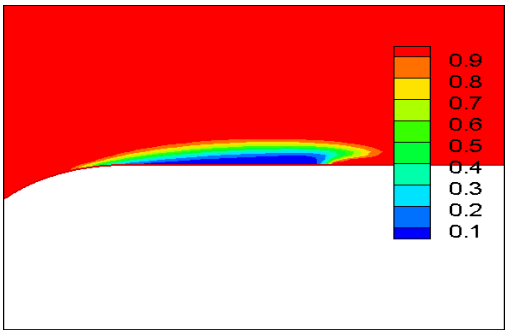

(a) Hemi. projectile,
$\mu_T/\mu_L|_{inlet}$ =1.5 × 10^2, effective *Re*=900

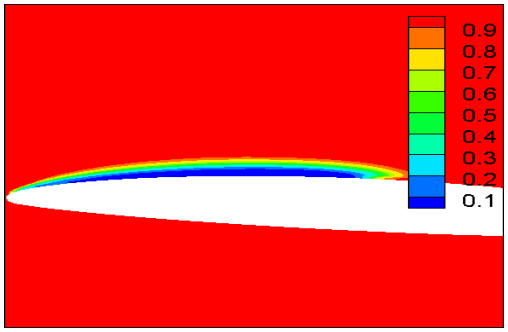

(b) NACA66MODE hydrofoil
$\mu_T/\mu_L|_{inlet}$ =10^3, effective *Re*=2000

Figure 3.2 The liquid volume fraction contour α_l and cavity shape for isothermal cases by baseline *k*-ε model

number is 2000, 1000, and 200. With the baseline k-ε model (no filter), the cavity shapes and the liquid volume fraction distributions are highlighted in Figure 3.2 based on the viscosity ratio 1.5×10^2 (effective *Re*=900) for the hemispherical projectile and 10^3 (effective *Re*=2000) for the NACA66MODE hydrofoil. The wall pressure distribution along with the experimental data [5,6] and liquid volume fraction α_l corresponding to different inlet turbulent quantities are shown in Figure 3.3.

The results in Figure 3.3 show a much higher dependency of inlet turbulent quantities for NACA66MOD hydrofoil than that for the hemispherical projectile. Efforts have been made to elucidate the mechanisms responsible for these diverging trends. First, Figure 3.4 simply confirms that for high Reynolds number flows, the dynamic pressure is much larger than the shear stress overall. In general, cavitation appears largely from the exchange between dynamic and static pressures locally. However, the viscous effect, which is confined to a very thin region of the high Reynolds number flows, can significantly modify the effective shape of a solid object through the concept of displacement thickness. This is defined along the normal direction of a solid surface:

$$\delta^* = \int_0^\infty (1 - \frac{\rho u}{(\rho u)_\infty}) dn \qquad (3.2)$$

For the hemispherical projectile, Figure 3.5(a) shows that profiles of the displacement thickness for different inlet turbulent quantities are consistent except near s/D=0. However, since cavitation occurs in the straight section of the projectile, the effective object shape modified by δ^* does not affect the sink term m^- and the source term m^+ in the cavitation model as illustrated in Figure 3.5(b), so the cavity size and mixture density

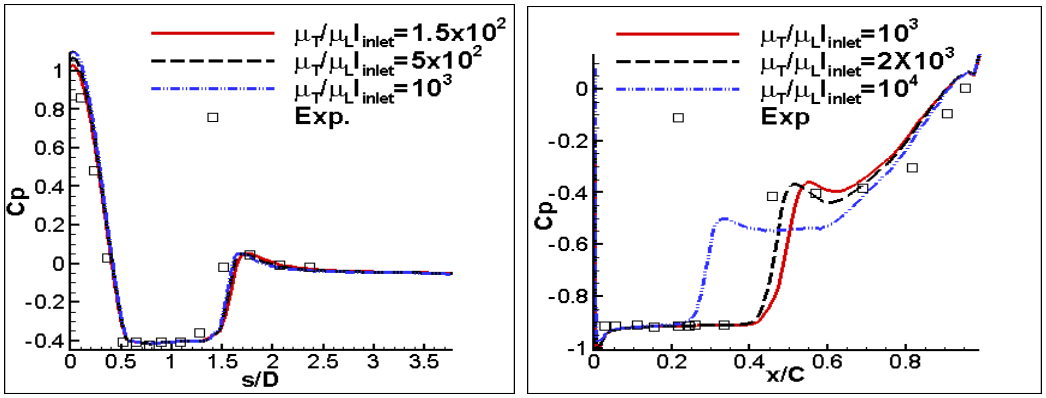

(a) C_p, hemispherical projectile (b) C_p, NACA66MODE hydrofoil

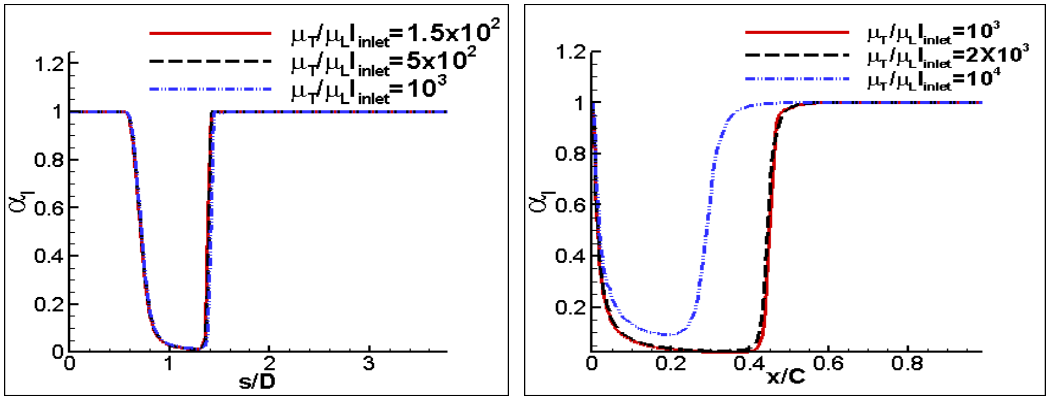

(c) α_l, hemispherical projectile (d) α_l, NACA66MODE hydrofoil

Figure 3.3 C_p and α_l along surface of different $\mu_T/\mu_L|_{\text{inlet}}$, isothermal cases by baseline k-ε model (without filter)

(For hemi. projectile, 1.5×10^2, 5×10^2, and 10^3 correspond to the effective Re of 900, 270, and 136; for NACA66MOD hydrofoil, 10^3, 2×10^3, and 10^4 correspond to the effective Re of 2×10^3,10^3, and 10^2. D is the diameter of hemispherical front, and C is the chord length of NACA66MODE hydrofoil)

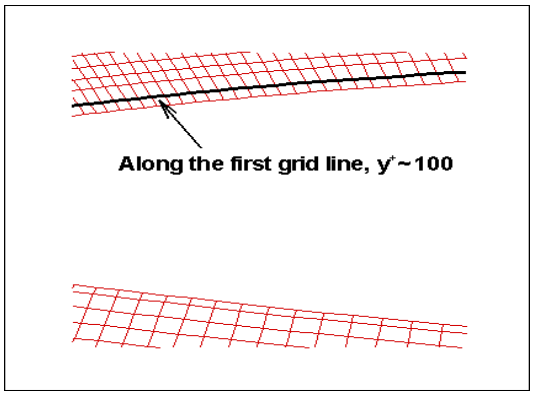

(a) Layout of first grid line on first grid line

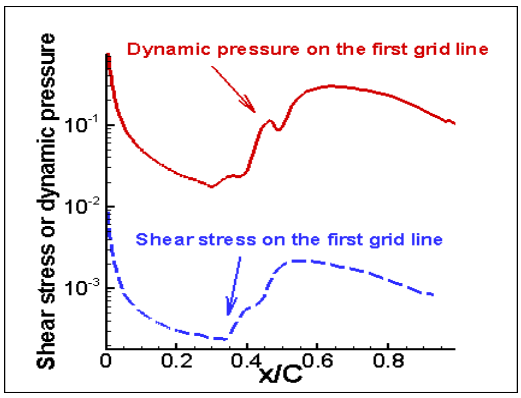

(b) Dynamic pressure vs. shear stress

Figure 3.4 Near-wall grid layout and quantities along the first grid line of NACA66MODE hydrofoil

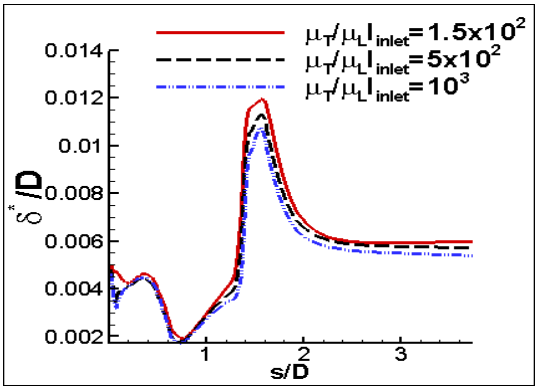

(a) δ*

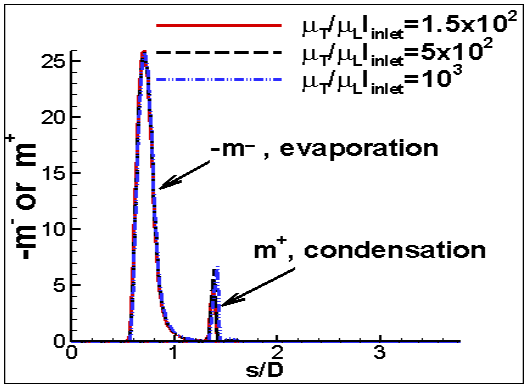

(b) m^- or m^+along the first grid line

Figure 3.5 Associated flow variables for hemispherical projectile along surface by baseline k-ε model

(s denotes distance along the surface and D is the diameter of hemispherical front)

inside the cavity in Figure 3.3(a) and (c) are comparable by different inlet turbulent quantities. For the NACA66MOD hydrofoil, as shown in Figure 3.6(a), the displacement thickness varies between the different inlet conditions and consequently affects the pressure field and cavitation formation. Due to a smaller mixture density after the leading edge for a lower inlet eddy-to-laminar viscosity ratio in Figure 3.3(d), the corresponding displacement thickness becomes larger in Figure 3.6(b). Therefore, the sink (evaporation) term m^- is stronger in Figure 3.6(c). As for the source (condensation) term m^+, a lower inlet eddy-to-laminar viscosity ratio gives a smaller value. When combined with a larger sink term, a larger cavity size will be obtained. Because of this, the cavity size is more sensitive for different inlet turbulent quantities, and the cavity size is larger as inlet eddy-to-laminar viscosity ratio becomes smaller.

In Figure 3.7, the simulation results of NACA66MOD hydrofoil are illustrated again by using the filter-based turbulence model in Equation (2.29) (FBM, Johansen et al. [8] as discuss in Chapter 2.2) with a filter size Δ=1.5 times maximum grid size to NACA66MOD hydrofoil:

$$\begin{aligned} \nu_T &= 0.09\frac{k^2}{\varepsilon} f \\ f &= \min(1\ , \frac{\Delta \cdot \varepsilon}{k^{3/2}}) \end{aligned} \tag{2.29}$$

As shown in Figure 3.7(a), the displacement thicknesses of all cases become insensitive to the inlet turbulent quantities; therefore, the pressure distributions shown in Figure 3.7(b) and other variables such as the sink (evaporation) term m^- in Figure 3.7(c) and the source (condensation) term m^+ in Figure 3.7(d) are comparable based on different inlet conditions.

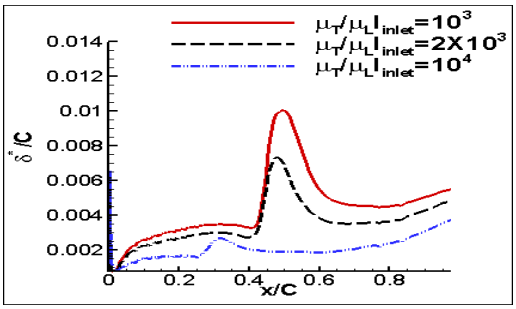

(a) δ*

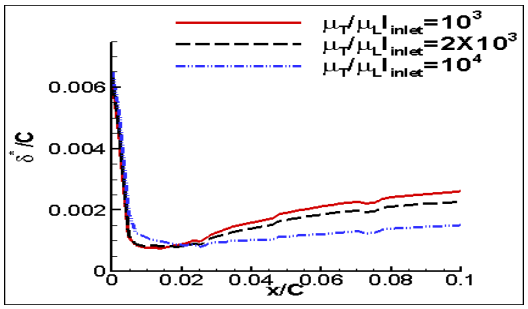

(b) δ* near trhe leading edge

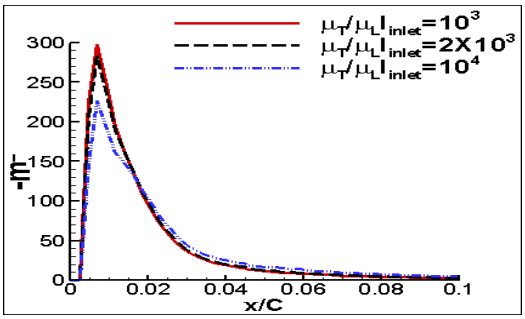

(c) m^- along the first grid line

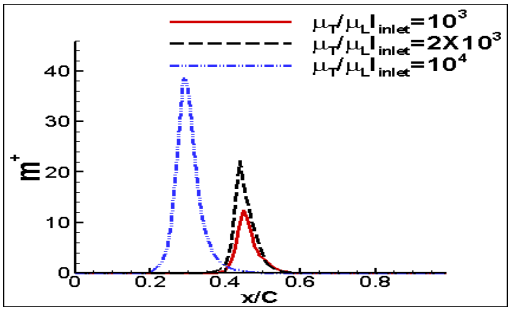

(d) m^+ along the first grid line

Figure 3.6 The various flow variables and cavitation model terms for the NACA66MODE hydrofoil by using the baseline k-ε model

(10^3, 2×10^3, and 10^4 corresponds to effective Re of 2000, 1000, and 200 respectively)

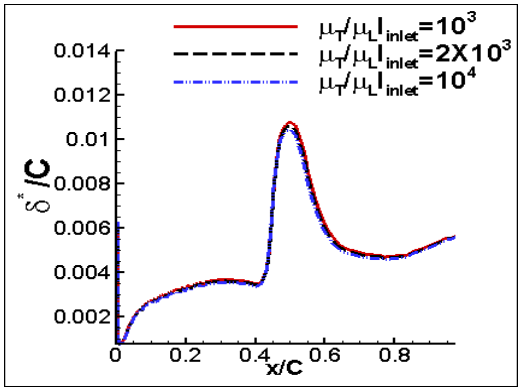

(a) δ*

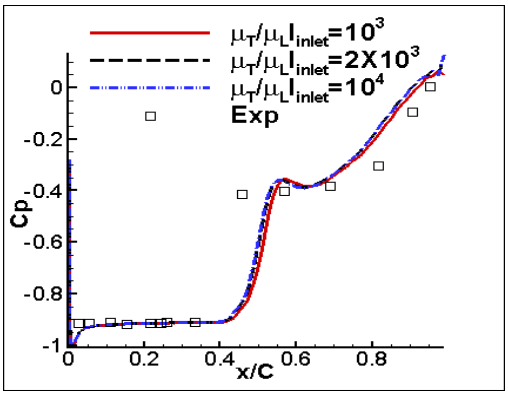

(b) C_p

Figure 3.7 Results after using FBM with Δ=1.5 maximum grid size for NACA66MODE hydrofoil

(10^3, 2×10^3, and 10^4 corresponds to effective Re of 2000, 1000, and 200 respectively)

Figure 3.8, Figure 3.9, and Figure 3.10 explain how the filter helps reduce the sensitivity of the solution with respect to the inlet conditions. For a higher inlet eddy-to-laminar viscosity ratio, the filter function $\min(1,\Delta/(k^{1.5}/\varepsilon))$ is lower, and the numerical resolution of the grid adopted here is sufficient to produce solutions with less dependence of the turbulence model. Hence, the eddy viscosity is lowered after the inlet region, resulting in reduced sensitivity of the computations. Based on this observation, even though FBM is not invoked in the near wall region due to the wall function treatment, it still can affect the overall solutions. Figure 3.11 clearly shows that the eddy viscosity in the near wall region is reduced after using FBM.

It should be noted that under the current approach, the phase change is driven by the thermodynamic conditions (namely, pressure and density in the sink/source terms), and the turbulence effect appears indirectly via the computation of the flow field in momentum and energy equations. In a separate effort, the effect of turbulence has also been addressed directly in the cavitation model. In particular, Singhal et al [9] observed that the drift of bubbles could penetrate the region where pressure is already higher than the vapor pressure. They proposed that a possible mechanism for this phenomenon is the pressure fluctuations, which is $0.39\rho k$, due to the turbulence. For the cases considered in the present model, this impact of the turbulent fluctuation is insignificant (less than 1% near the leading edge and inside the cavity).

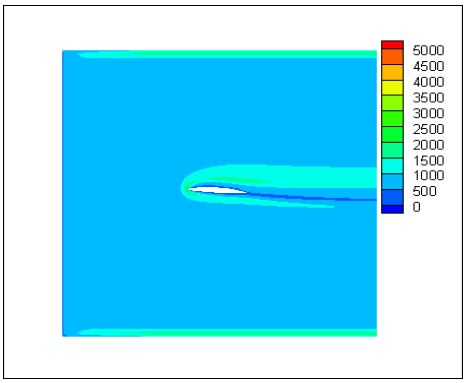

(a) $\mu_T/\mu_L|_{inlet}$ before FBM

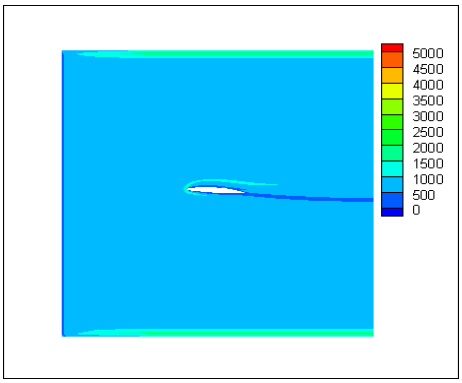

(b) $\mu_T/\mu_L|_{inlet}$ with FBM

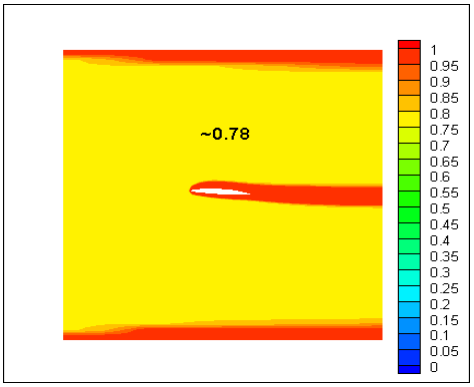

(c) $\min(1,\Delta/(k^{1.5}/\varepsilon))$

Figure 3.8 Comparisons before/after FBM for NACA66MODE hydrofoil, $\mu_T/\mu_L|_{inlet}=10^3$, effective Re= 2000

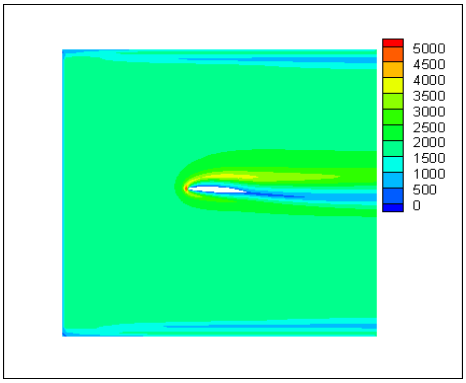

(a) $\mu_T/\mu_L|_{inlet}$ before FBM

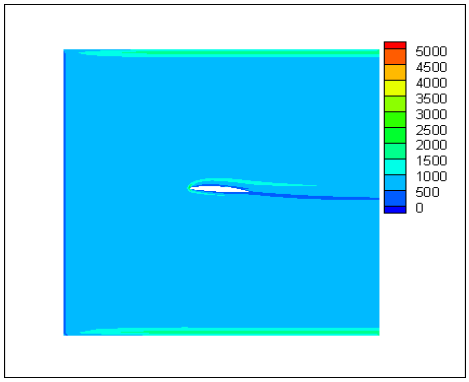

(b) $\mu_T/\mu_L|_{inlet}$ with FBM

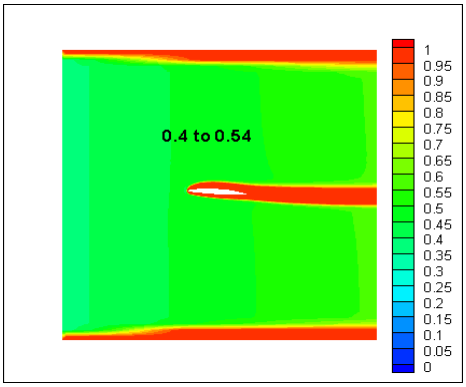

(c) $\min(1,\Delta/(k^{1.5}/\varepsilon))$

Figure 3.9 Comparisons before/after FBM for NACA66MODE hydrofoil, $\mu_T/\mu_L|_{inlet}$ $=2\times10^3$, effective Re=1000

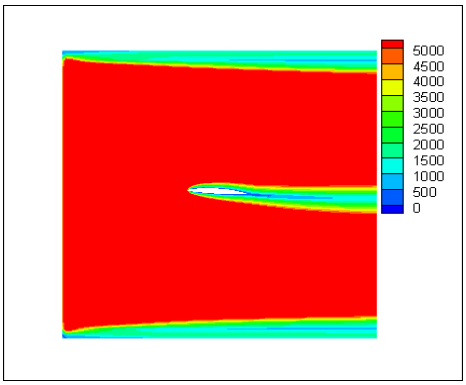

(a) $\mu_T/\mu_L|_{inlet}$ before FBM

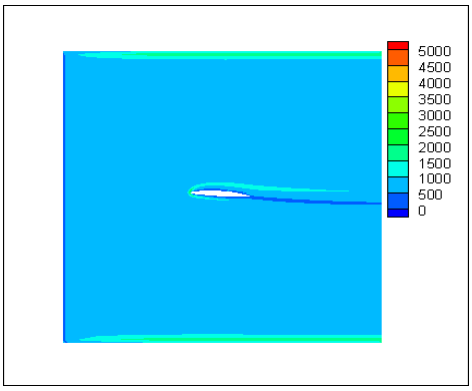

(b) $\mu_T/\mu_L|_{inlet}$ with FBM

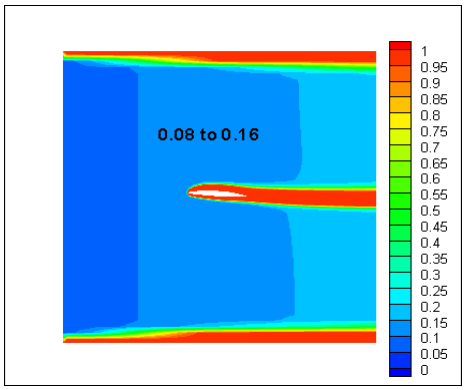

(c) $\min(1,\Delta/(k^{1.5}/\varepsilon))$

Figure 3.10 Comparisons with/without FBM for NACA66MODE hydrofoil, $\mu_T/\mu_L|_{inlet}$ $=10^4$, effective Re= 200

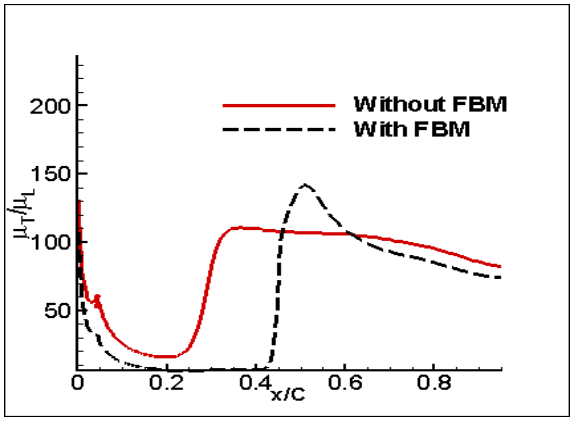

Figure 3.11 μ_T/μ_L near the wall region for NACA66MODE hydrofoil, $\mu_T/\mu_L|_{inlet}$ =10^4, effective Re= 200

3.2 MODELING OF CRYOGENIC CAVITATION

In this section, the filter-based turbulence model in Equation (2.29) and cavitation model in Equation (2.3) are used to investigate the competing effects between cavitation number and density ratio.

For water under room temperature, the thermal effects can be neglected. However, the impact of thermal effects in cryogenic cavitation has already shown in Figure 1.1. These thermo-sensible material properties will affect the energy equation in the following Equation (3.3) and cavitation sink/source terms in Equation (2.3):

$$\frac{\partial}{\partial x_j}[\rho_m u_j (h + f_v L)] = \frac{\partial}{\partial x_j}[(\frac{\mu_L}{\mathrm{Pr}_L} + \frac{\mu_t}{\mathrm{Pr}_t})\frac{\partial h}{\partial x_j}] \tag{3.3}$$

The temperature can be interpolated based on enthalpy in the database [10], and the vapor mass fraction is expressed as:

$$f_v = \frac{\rho_v(1-\alpha_l)}{\rho_m} \tag{3.4}$$

The effects of kinetic energy and viscous dissipation terms in Equation (3.3) are neglected ($O(Re^{-0.5})$, Re is around 10^6) because the evaporative cooling in cryogenic cavitation is the main contributor to the temperature field.

First, the latent heat L in Equation (3.3) appears as a non-linear source term and represents the latent heat transfer rate during the phase change. The spatial variation of the thermodynamic properties together with the evaporative cooling effect is embedded into this equation and causes a coupling with the set of governing equations [4,11,12].

As for the cavitation sink/source terms in Equation (2.3), one can assess the impacts due to the thermo-sensible material properties by using Taylor's series and neglect the higher order terms. The sink term m^- is first considered as the pressure is smaller than the vapor pressure based on the local temperature [4], or in other words, pressure coefficient C_p is smaller than $-\sigma$. Furthermore, the minus sign here in Equation (3.5) is for convenience to show that the larger evaporation strength will correspond to a larger positive value of $-m^-$.

$$
\begin{aligned}
-m^- &= -\frac{C_{dest}\alpha_l}{t_\infty}\frac{\rho_l}{\rho_v}\left(\frac{\min(0, P-P_v(T))}{0.5\rho_l U_\infty^2}\right) = -\beta R(T)\min(0,\ C_p+\sigma) \\
&= -\beta\left(R(T_\infty)+\left.\frac{dR}{dT}\right|_{T_\infty}\Delta T+\ldots\right)\left(C_p+\sigma_\infty-\left.\frac{dP_v}{dT}\right|_{T_\infty}\frac{\Delta T}{0.5\rho_l U_\infty^2}+\ldots\right) \\
&= -\beta\left(R(T_\infty)(C_p+\sigma_\infty)+(C_p+\sigma_\infty)\left.\frac{dR}{dT}\right|_{T_\infty}\Delta T-R(T_\infty)\left.\frac{dP_v}{dT}\right|_{T_\infty}\frac{\Delta T}{0.5\rho_l U_\infty^2}+\ldots\right)
\end{aligned}
\tag{3.5}
$$

here β is $C_{dest}\alpha_l/t_\infty$ and R is the temperature-dependent liquid-to-vapor density ratio. Similarly, for source term m^+ as the pressure is larger than the vapor pressure (C_p is larger than $-\sigma$):

$$
\begin{aligned}
m^+ &= \frac{C_{prod}(1-\alpha_l)}{t_\infty}\frac{\max(0, P-P_v(T))}{0.5\rho_l U_\infty^2} = \gamma\max(0,\ C_p+\sigma) \\
&= \gamma\left((C_p+\sigma_\infty)-\left.\frac{dP_v}{dT}\right|_{T_\infty}\frac{\Delta T}{0.5\rho_l U_\infty^2}+\ldots\right)
\end{aligned}
\tag{3.6}
$$

where γ is $C_{prod}(1.\alpha_l)/t_\infty$. Please note that $\Delta T=T-T_\infty<0$ in both Equation (3.5) and (3.6), which is defined based on evaporative cooling.

It can be concluded that the competing influence of the thermal effects in the cavitation model results from two aspects of Equation (3.5) during evaportative cooling as $\Delta T=T-T_\infty<0$: (a) the thermal rate of change of liquid-to-vapor density ratio (dR/dT), which is

negative in Figure 1.1, together with $C_p+\sigma_\infty < 0$ and $\Delta T < 0$ as evaporation occurs will tend to enhance the strength of $-\dot{m}^-$; and (b) the thermal rate of change of vapor pressure (dp_v/dT), which is positive in Figure 1.1, will tend to suppress $-\dot{m}^-$. It is also obvious that the impacts of thermal effects will change significantly for different working temperatures and pressures due to the non-linear variation of material properties from energy equation in Equation (3.3) and cavitation sink/source terms in Equation (2.3) [4,11].

Cavitation with thermal effects in the cryogenic liquids past a 2D quarter hydrofoil, illustrated in Figure 3.12 with number of grids=2×10^4, will be presented here. The Case 290C and 296B from the experimental data reported by Hord [13] are investigated with the following conditions: σ_∞=1.7, Re=9.1 × 10^6, T_∞=83.06K for 290C; σ_∞=1.61, Re=1.1×10^7, T_∞=88.54K for 296B. The working liquids for these two cases here are both liquid nitrogen. In the following, based on Case 290C and 296B, the assessment of the thermal effect on cavitating flow structures is presented.

Cavitation and filter-based turbulence closure are still used as those presented in Equation (2.3) and (2.29) as described in Chapter 3.1. The empirical constants are chosen as C_{dest} =0.639 and C_{prod} =54.4 as suggested in [11]. Figure 3.13 and Figure 3.14 compare the predicted and experimental pressure and temperature profiles in [13] on the hydrofoil surface. Overall, the present cavitation and turbulence models can consistently capture

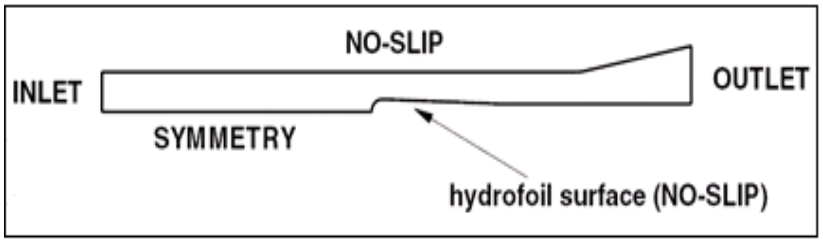

Figure 3.12 Schematic of the geometries and the boundary conditions of the cryogenic cases [13]

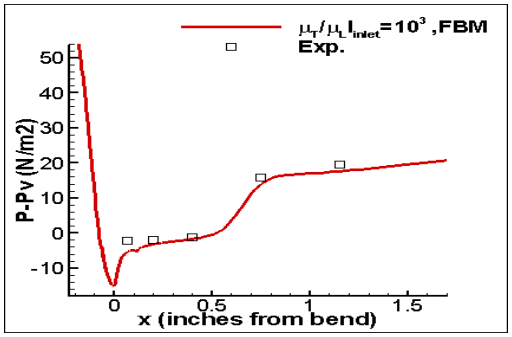

(a) Pressure

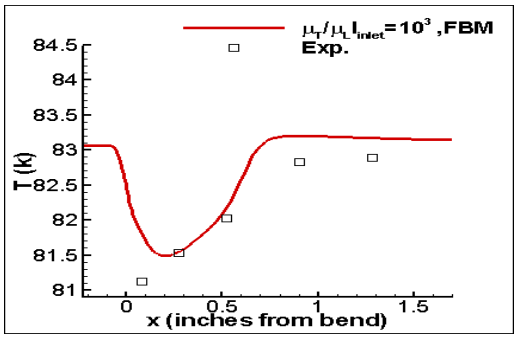

(b) Temperature

Figure 3.13 Cryogenic cavitation Case 290C, pressure and temperature along surface by filter-based model with Δ=1.5 maximum grid size

($\mu_T/\mu_L|_{inlet}$ =10^3, σ_∞=1.7, Re=9.1×10^6, T_∞=83.06K)

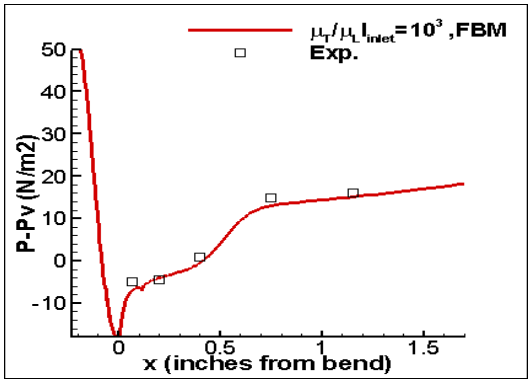

(a) Pressure

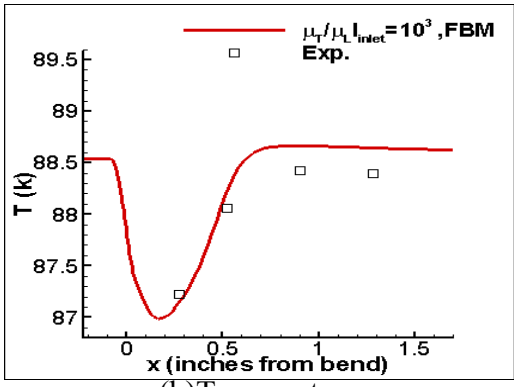

(b)Temperature

Figure 3.14 Cryogenic cavitation Case 296B, pressure and temperature along surface by filter-based model with Δ=1.5 maximum grid size

($\mu_T/\mu_L|_{inlet}$ =10^3, σ_∞=1.61, Re=1.1×10^7, T_∞=88.54K)

the main features of both pressure and thermal profiles. The temperature drop inside the cavity in Figure 3.13(b) and Figure 3.14(b) also clearly demonstrates the evaporative cooling resulting from cryogenic cavitation. In Figure 3.15, as a further assessment based on Case 290C, one can compare the present cryogenic model solution in Figure 3.15(a) with the isothermal solution in Figure 3.15(b) obtained by using the identical model except that the energy equation is not invoked. Clearly, the thermal field does affect the cavity structures. The cavity size is reduced due to the thermal effect because the temperature drop inside the cavity decreases the local vapor pressure. Therefore, the temperature drop inside the cavity increases the local cavitation number, resulting in a weaker cavitation intensity and higher overall liquid volume fraction in the cavity as shown in Figure 3.15(c). Finally, in Figure 3.15(d), the pressure profile inside the cavity is steeper under the cryogenic condition than when under the isothermal condition.

The local cavitation number $\sigma(T)$ and temperature contours are illustrated in Figure 3.16 and Figure 3.17. The free stream cavitation number of Case 296B (σ_∞=1.61, T_∞=88.54K) is smaller than that of Case 290C (σ_∞=1.7, T_∞=83.06K). However, the evaporative cooling and associated factors, such as the thermal rate of change of the vapor pressure, increase when temperature approaches critical temperature as shown in Figure 1.1(a). This effect causes a greater increase in local cavitation number σ inside the cavity for Case 296B in Figure 3.17(b) than that of Case 290C in Figure 3.16(b). This phenomenon can be directly revealed from Equation (1.3):

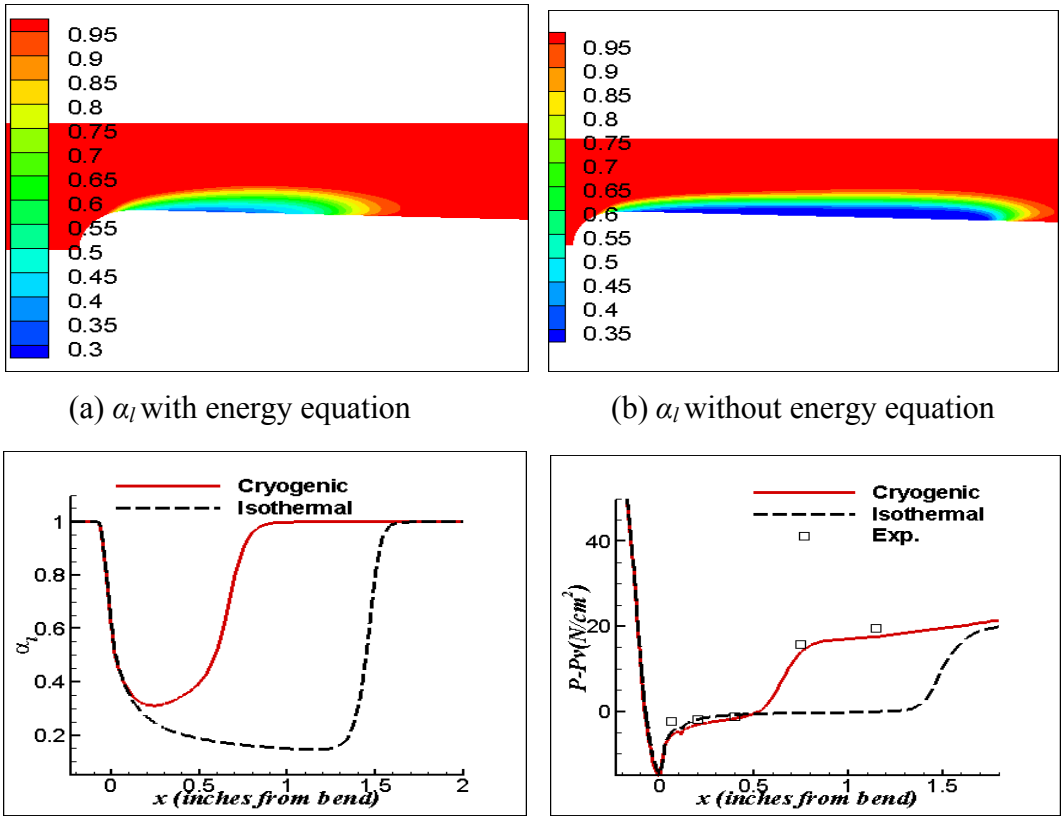

(a) α_l with energy equation

(b) α_l without energy equation

(c) α_l along surface

(d) Pressure along surface

Figure 3.15 Comparisons for cryogenic cavitation Case 290C between results with/without energy equation

($\mu_T/\mu_L|_{inlet}$ =10^3, σ_∞=1.7, Re=9.1×10^6, T_∞=83.06K)

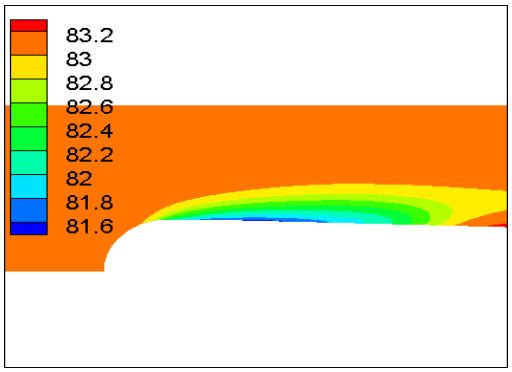

(a)Temperature

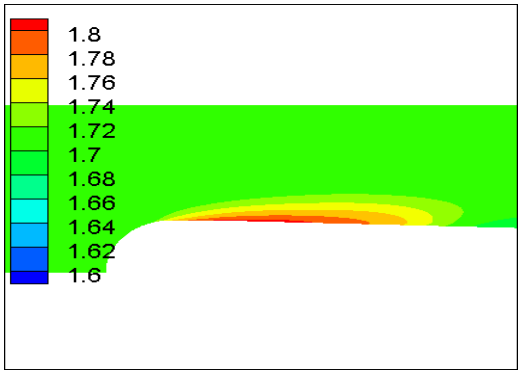

(b) $\sigma=\sigma(T)$

Figure 3.16 Cryogenic cavitation Case 290C, the impact of thermal effect on local cavitation number

($\mu_T/\mu_L|_{inlet}=10^3$, $\sigma_\infty=1.7$, $Re=9.1\times10^6$, $T_\infty=83.06$K)

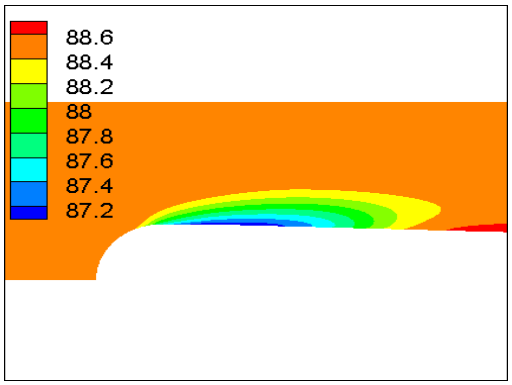

(a)Temperature

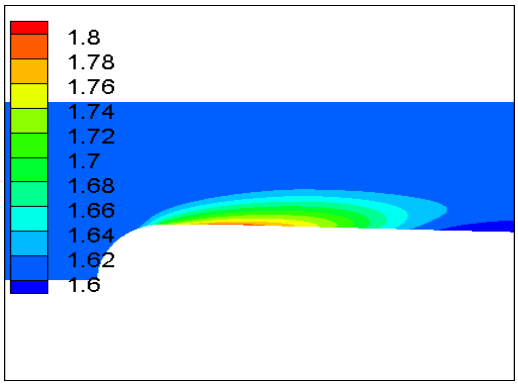

(b) $\sigma=\sigma(T)$

Figure 3.17 Cryogenic cavitation Case 296B, the impact of thermal effect on local cavitation number

($\mu_T/\mu_L|_{inlet}=10^3$, $\sigma_\infty=1.61$, $Re=1.1\times10^7$, $T_\infty=88.54$K)

$$\frac{1}{2}\rho_l U_\infty^2(\sigma-\sigma_\infty)=\frac{dP_v}{dT}(T_\infty-T)$$
$$\sigma=\sigma_\infty-\frac{dP_v}{dT}\frac{\Delta T}{0.5\rho_l U_\infty^2};\ \Delta T=T-T_\infty<0 \qquad (1.3)$$

Under comparable temperature drop and free stream dynamic pressure, a higher thermal rate of change of vapor pressure due to a higher temperature will cause a higher increase of local cavitation number and hence involves a stronger thermal effect. For isothermal cases, a higher free stream cavitation number will result in a larger cavity length. However, the overall higher local cavitation number in Figure 3.16(b) of Case 290C still gives a larger cavity length than that of Case 296B. This reveals that a local cavitation number itself is not enough to describe the detail of cavitation dynamics in cryogenic cavitation.

In order to probe the cavitation dynamics, Equation (3.5) for evaporation dynamics of the present cavitation model is rewritten here:

$$-m^- = -\frac{C_{dest}\alpha_l}{t_\infty}\frac{\rho_l}{\rho_v}\left(\frac{\min(0,P-P_v(T))}{0.5\rho_l U_\infty^2}\right)=-\beta R(T)\min(0,\ C_p+\sigma) \qquad (3.7)$$

The evaporation intensity is clearly linked to not only the conditional statement term, min(0, C_p+σ) in Figure 3.18(a) and (b), but also to the density ratio R in Figure 3.18(c) and (d). The local cavitation number σ and -min(0, C_p+σ) actually demonstrate the same thing: if the local cavitation number is smaller, it means the tendency to be cavitated for local liquids should be easier, and hence the affected area and the value of -min(0, C_p+σ) are larger. However, even though the local cavitation number is smaller and the

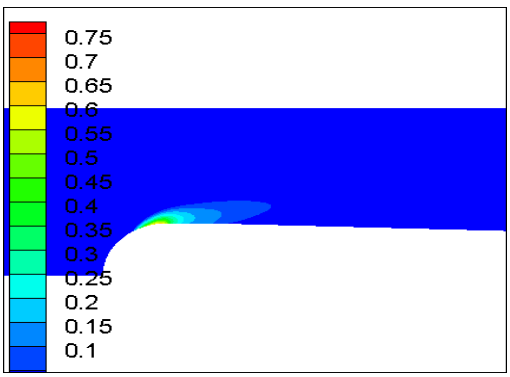

(a) -min(0, Cp+σ), 290C

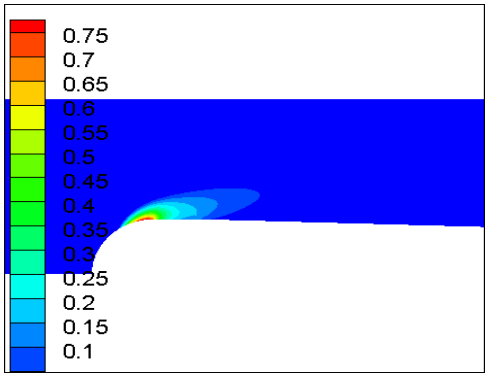

(b) -min(0, Cp+σ), 296B

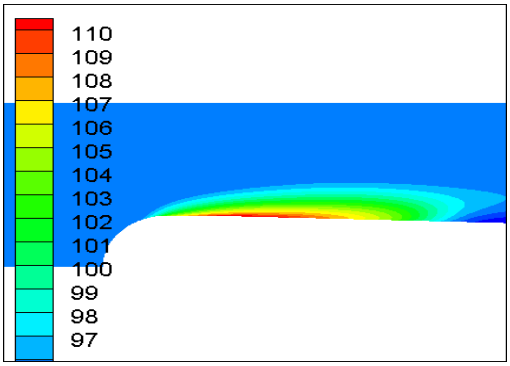

(c) Liquid-to-vapor density ratio, 290C

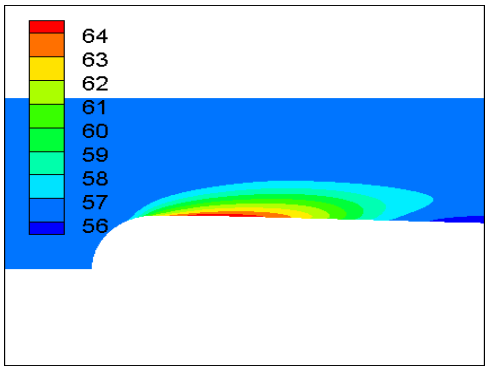

(d) Liquid-to-vapor density ratio, 296B

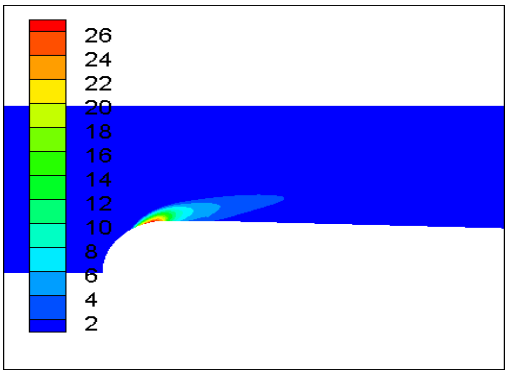

(e) $-\dot{m}^-$, 290C

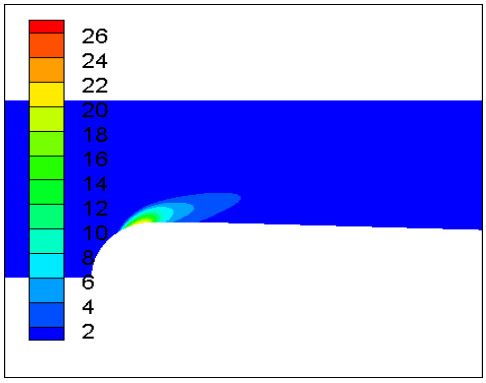

(f) $-\dot{m}^-$, 296B

Figure 3.18 The impact of thermal effect on evaporation sink term for cryogenic cavitation

(Case 290C: $\mu_T/\mu_L|_{inlet}=10^3$, $\sigma_\infty=1.7$, $Re=9.1\times10^6$, $T_\infty=83.06$K; Case 296B: $\mu_T/\mu_L|_{inlet}=10^3$, $\sigma_\infty=1.61$, $Re=1.1\times10^7$, $T_\infty=88.54$K. The evaporation sink terms in (e) and (f) are illustrated with a minus sign)

conditional statement term -min(0, $C_p+\sigma$) is larger for Case 296B, the density ratio R is smaller for Case 296B in Figure 3.18(d) than that for Case 290C in Figure 3.18(c) since Case 290C has a lower temperature; thus Case 296B ends up with a weaker evaporation sink term from Equation (3.7) in Figure 3.18(f) than that for case 290C in Figure 3.18(e) even though the local cavitation number is smaller overall. The comparison is based on the same β ($C_{dest}\alpha_l/t_\infty$) in the evaporation region. This assumption is reasonable since the coefficient for the evaporation term is a constant, and the inlet velocity is within 1% difference to give comparable t_∞. Also from Figure 3.19, one could see that the distribution of the liquid volume fraction α_l is comparable in the leading edge where evaporation occurs.

The stronger evaporation term for Case 290C allows the mixture phase inside the cavity to have more expansion so that the liquid volume fraction/mixture density is lower for Case 290C and results in a longer cavity length, which is shown in Figure 3.19

As for condensation dynamics, it is dominated by Equation (3.6) in our current framework and can be rewritten as Equation (3.8):

$$m^+ = \frac{C_{prod}(1-\alpha_l)}{t_\infty}\frac{\max(0, P - P_v(T))}{0.5\rho_l U_\infty^2} = \gamma \max(0,\ C_p + \sigma) \qquad (3.8)$$

In addition to max(0, $C_p+\sigma$), the term (1.α_l) is also very important. Unlike similar liquid volume fraction distributions near the leading edge as evaporation occurs, Case 290C and 296B have different distributions of liquid volume fraction near the closure region as condensation occurs. In Figure 3.20(a) and (b), which track the corresponding values

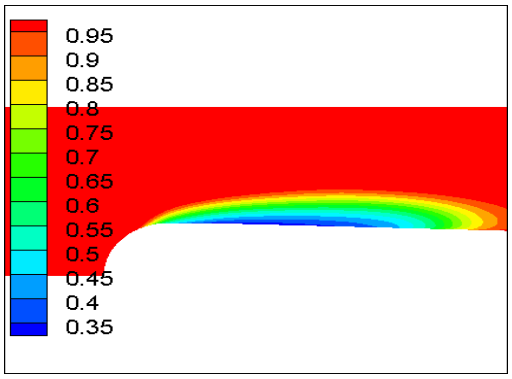

(a) 290C

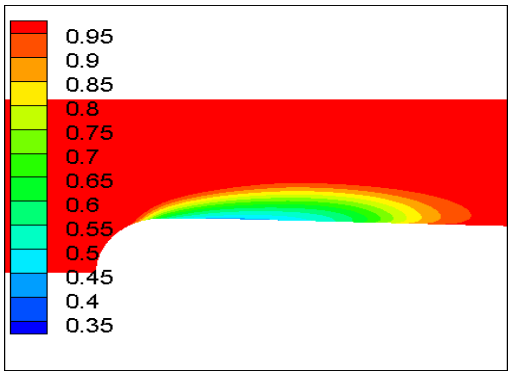

(b) 296B

Figure 3.19 Comparisons of cavity size and liquid volume fraction for Case 290C and 296B

(Case 290C: $\mu_T/\mu_L|_{inlet}=10^3$, $\sigma_\infty=1.7$, $Re=9.1\times10^6$, $T_\infty=83.06$K; Case 296B: $\mu_T/\mu_L|_{inlet}=10^3$, $\sigma_\infty=1.61$, $Re=1.1\times10^7$, $T_\infty=88.54$K)

along the surface, one can observe Case 290C has a larger (1-α_l) term in Figure 3.20(a) due to more vapor phase inside the cavity. After combining max(0, C_p+σ) term in Figure 3.20(b), the condensation term is stronger for Case 290C in Figure 3.20(c). The peaks also correspond to the locations of the closure region. In Case 290C and 296B, the condensation dynamics is also affected by the value of liquid volume fraction, which is dominated by evaporation.

To highlight the competing effects between Case 290C and 296B, Taylor's series is used in Equation (3.5) and can be regrouped as below:

$$-\dot{m}^- = \beta([-R(T_\infty)(C_p+\sigma_\infty)]+[-(C_p+\sigma_\infty)\frac{dR}{dT}\Big|_{T_\infty}\Delta T]+[R(T_\infty)\frac{dp_v}{dT}\Big|_{T_\infty}\frac{\Delta T}{0.5\rho_l U_\infty^2}]+.....$$

First it can be seen that the conditional statement term -min(0, C_p+σ) is based on free stream properties, which actually is -min(0, C_p+σ_∞) under isothermal consideration. In Figure 3.21, the value and area are both larger compared with those in Figure 3.18(e) and (f) with thermal effect; therefore, the influence of thermal effect, which is more significant for Case 296B (larger difference between Figure 3.18(f) and Figure 3.21(b) for Case 296B than that between Figure 3.18(e) and Figure 3.21(a) for Case 290C) is illustrated again. It can be shown that all three terms in the right hand side of Taylor's series clearly express the competing effect because none of the terms increase or decrease monotonically:

(i). For the first term $-R(T_\infty)(C_p+\sigma_\infty)$ after the Taylor's expansion, Case 290C has a smaller $-\min(0, C_p+\sigma_\infty)$ in Figure 3.21(a) but a higher density ratio $R(T_\infty)$.

(ii). For the second term $-(C_p+\sigma_\infty)dR/dT|_{T\infty}$, dR/dT is -9.5 and -5.1 for Case 290C and 296B respectively, and $-\min(0, C_p+\sigma_\infty)$ is smaller for Case 290C.

(iii). For the third term $R(T_\infty)\ dp_v/dT|_{T\infty}$, dp_v/dT is 19 and 28 kPa/K for Case 290C and 296B respectively, and the density ratio $R(T_\infty)$ is larger for Case 290C.

To sum up, for Cases 290C and 296B, there are competing effects between a larger cavitation number (which forms weaker cavitation) and a larger liquid-to-vapor density ratio (which promotes cavitation); in Case 290C, this results in a larger cavity length than that of Case 296B. Therefore, the cavitation dynamics of cryogenic cavitation depends on both the local cavitation number and the vapor-to-liquid density ratio.

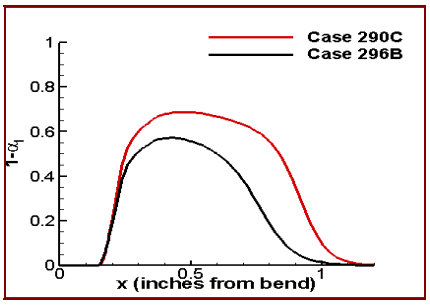

(a) $1-\alpha_l$

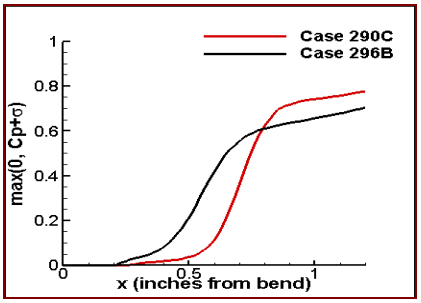

(b) $\max(0, C_p+\sigma_\infty)$

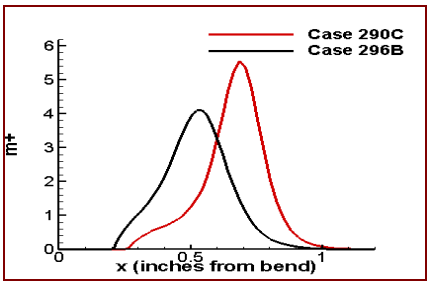

(c) m^+

Figure 3.20 Examine for condensation dynamics along the surface

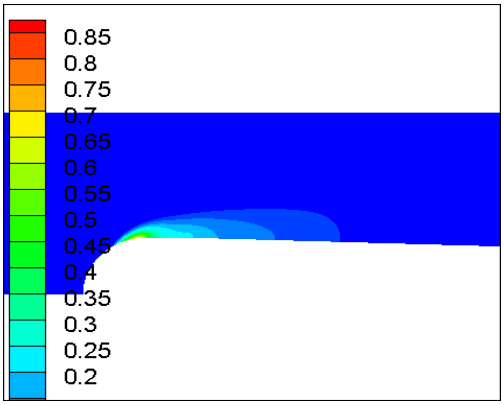

(a) 290C

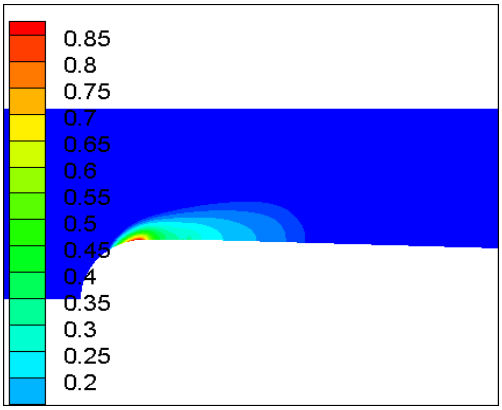

(b)296B

Figure 3.21 Contour for - $min(0, C_p+\sigma_\infty)$ based on free stream properties (without thermal effect)

BIBLIOGRAPHY

1. Wu, J.Y., Wang, G.Y., Shyy, W.: Time-dependent Turbulent Cavutating Flow Computations with Interfacial Transport and Filter-based Models. International Journal for Numerical Methods in Fluids 49(7), 739-761 (2005)
2. Hosangadi, A., Ahuja, V.: A Numerical Study of Cavitation in Cryogenic Fluids. Journal of Fluids Engineering 127, 267-281 (2005)
3. Li, D.Q.I., Naoya, O., Lindell, P., Toshiaki, I.: A Modified SST K- Turbulence Model to Predict the Steady and Unsteady Sheet Cavitation on 2D and 3D Hydrofoils. CAV2009, Paper No. 107, Proceedings of the 7th International Symposium on Cavitation, August 17-22, 2009, Ann Arbor, Michigan, USA.
4. Tseng, C., Shyy, W,: Modeling for isothermal and cryogenic cavitation, Int. J. Heat Mass Transfer 53, 513-525 (2010)
5. Rouse, H., McNown, J.S.: Cavitation and Pressure Distribution, Head Forms at Zero Angle of Yaws Flow Phenomenon. Studies in Engineering, Bulletins 32, State University of Iowa (1948)
6. Shen, Y., Dimotakis, P.: The Influence of Surface Cavitation on Hydrodynamic Forces. Proc", 22nd. ATTC, St. Johns, 44-53 (1989)
7. Merkle, C.L., Feng, J., Buelow, P.E.O.: Computational Modeling of Sheet Cavitation. Proc. 3rd International Symposium on Cavitation, Grenoble, France 1998.
8. Johansen, S.T., Wu, J.Y., Shyy, W.: Filter Based Unsteady RANS Computational. International Journal of Heat and Fluid Flow 25, 10-21 (2005)
9. Singhal, A.k., Li, H., Athavale, M.M., Jiang, Y., Mathematical Basis and Validation of the Full Cavitation Model. J. Fluids Eng 124(3), 617-625 (2002)
10. Lemmon, E.W., McLinden, M.O., Huber, M.L.: REFPROP: Reference Fluid Thermodynamic and Transport Properties. NIST Standard Database 23, version 7.0 (2002)
11. Goel, T., Zhao, J., Thakur, S., Haftka, R. T., Shyy, W., Zhao, J.: Surrogate Model-Based Strategy for Cryogenic Cavitation Model Validation and Sensitivity Evaluation", Int. J. Numer. Meth. Fluids 58, 969-1007 (2008)
12. Utturkar, Y., Wu, J., Wang, G., Shyy, W.:Recent Progress in Modeling of Cryogenic Cavitation for Liquid Rocket Propulsion. Progress in Aerospace Sciences 41(7), 558-608 (2005)
13. Hord, J.: Cavitation in Liquid Cryogens II-Hydrofoil. NASA CR-2156 (1973)

CHAPTER 4

SURROGATE-BASED GLOBAL SENSITIVITY EVALUATION AND OPTIMIZATION OF MODEL PARAMETERS

In this chapter, a systematic investigation based on the surrogate modeling techniques is used to assess and improve the performance of the Merkle's phenomenological cavitation model in Equation (2.3) under cryogenic condition. Using the surrogate model, global sensitivity analysis is to be conducted to assess the role of model parameters regulating the condensation (C_{dest}) and evaporation rates (C_{prod}) in Equation (2.3) and uncertainties in material properties, specifically the vapor density ρ_v and latent heat L, which could possibly affect the thermodynamics of cavitation in Equation (2.3) and energy equation in Equation (3.3):

$$m^- = \frac{C_{dest}\alpha_l}{t_\infty}\frac{\rho_l}{\rho_v}\frac{\min(0, P - P_v)}{(0.5\rho_l U_\infty^2)} \quad m^+ = \frac{C_{prod}(1-\alpha_l)}{t_\infty}\frac{\max(0, P - P_v)}{(0.5\rho_l U_\infty^2)} \tag{2.3}$$

$$\frac{\partial}{\partial x_j}[\rho_m u_j (h + f_v L)] = \frac{\partial}{\partial x_j}[(\frac{\mu_L}{\mathrm{Pr}_L} + \frac{\mu_t}{\mathrm{Pr}_t})\frac{\partial h}{\partial x_j}] \tag{3.3}$$

Global sensitivity analysis allows decomposition of a suitable measure of prediction into the components of individual variables from which one can easily calculate the impact of each variable by Sobol [1]. This framework helps probe the global sensitivity of the cavitation model and material uncertainties; to facilitate this framework, suitable surrogate models will be constructed first [2-5]. Furthermore, since the fidelity of surrogate models is critical in determining the success of the sensitivity analysis, different

surrogate models are used to help ascertain the performance measures. In this section, four surrogate models are used, namely polynomial response surface approximation (PRS, [6]), Kriging (KRG, [7]), radial basis neural network (RBNN, [8]) and PRESS-based weighted average (PWS) surrogate model constructed by using the previous three surrogates [2,5].

4.1 THE DESIGN SPACE AND CONSTRUCTION OF THE SURROGATE MODEL

First, C_{dest}, C_{prod}, ρ_v, and L are chosen as design variables, while holding the Re_∞ and σ_∞ constant for the given cases. The performance of predictions for the cryogenic cavitation models are represented by the differences between computed and experimental values along the hydrofoil surface for temperature (T_{diff}) and pressure (P_{diff}) as objectives. The model parameters, C_{dest} and C_{prod}, vary from 0.578 to 0.68 and 46.2 to 54.4 respectively (this range is refined form the suggestion in [2]). The material properties ρ_v and L are perturbed within ±10% of the value from the NIST database [9].

The two empirical constants C_{dest} and C_{prod} in Equation (2.3) directly control the evaporation and condensation rate via the cavitation model. As a fluid property, ρ_v dominates the evaporative cooling and appears directly in the cavitation sink term. L will determine the energy absorbed or released during the phase change in Equation (3.3). Therefore, these four model parameters and fluid properties are selected as design variables.

There are five data points along the hydrofoil surface. The root mean square error along these five data points between the experimental data in [10] and our simulation results are evaluated as the objective functions T_{diff}, temperature prediction, and P_{diff}, pressure prediction. The geometry is already shown in Figure 3.12, and the computational framework is the same as those described previously in Chapter 3.2 for the cryogenic cavitation. A surrogate model will be constructed for both Case 290C (σ_∞=1.7, Re=9.1×10^6, T_∞=83.06K) and 296B (σ_∞=1.61, Re=1.1×10^7, T_∞=88.54K) to assess the generality of surrogate outcomes with different thermal effects. Figure 4.1 illustrates the high sensitivity of the empirical constants to T_{diff} and P_{diff} for Case 290C without perturbations in material properties (Case 296B has similar trends). The design variables and objective functions are summarized in Table 4.1.

To facilitate the development of surrogate models, 70 "training" points are chosen to balance the computational cost and accuracy of surrogate models by using combined face-centered cubic composite design (FCCD, 25 points) and Latin hypercube sampling (LHS, 45 points) [2]. Five additional test points that are not included in the 70 training points are used to validate the surrogate models for both Case 290C and 296B. PRS, KRG, RBNN, and PWS models are used for both objectives and cases. All variables and objectives are normalized such that '0' corresponds to the minimum value and '1' corresponds to the maximum value. Normalized variables and objectives are denoted by a superscript '*'. Second order polynomials for PRS and a spread coefficient=0.4~0.7 for RBNN are used here. Relevant details of surrogate models are documented in [2].

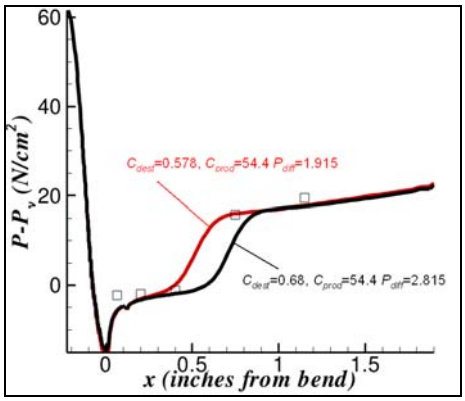

(a) Pressure

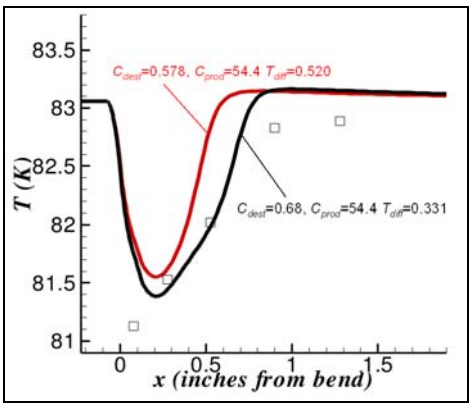

(b) Temperature

Figure 4.1: Sensitivity of C_{dest} in the design space for Case 290C (σ_∞=1.7, Re=9.1×10^6, T_∞=83.06K)

Table 4.1: Objective functions and design variables with corresponding ranges

Symbol	**Design variable**	**Range**
C_{dest}	Evaporation rate	0.578~0.68
C_{prod}	Condensation rate	46.2~54.4
ρ_v	Vapor density*	-10%~10%
L	Latent heat*	-10%~10%
Symbol	**Objective function**	
P_{diff}	Pressure difference between CFD and exp. data	
T_{diff}	Temperature difference between CFD and exp. data	

*: Vapor density and latent heat are relative to database values.

The PRESS RMS as discussed in Equation (2.41) are shown in Appendix Table A1:

$$\text{PRESS RMS} = \sqrt{\frac{1}{N_s}\sum_{i=1}^{N_s}(y_i - \hat{y}_i^{(-i)})^2} \tag{2.41}$$

It indicates that the KRG model has the best performance, while RBNN has the worst overall performance. The contribution of different surrogate models to the PWS model is given by the weights in Appendix Table A2. Since the performance of KRG is the best, its weight is also the greatest. There are additional five test points to validate the surrogates. Appendix Table A3 shows the locations of these points in the normalized design space for both Case 290C and 296B. The simulation results are compared with the prediction of surrogates in Appendix Table A4 and A5 for Case 290C, and Appendix Table A6 and A7 for Case 296B. Due to the best performance in error estimate in Appendix Table A1 and tests of the additional five samples from Appendix Table A4 to A7, KRG is used to demonstrate the global sensitivity analysis hereafter.

4.2 SURROGATE-BASED GLOBAL SENSITIVITY ANALYSIS AND SCATTER PLOTS

The global sensitivity analysis is conducted through Equation (2.42) to (2.45). From Figure 4.2 and Figure 4.3, which evaluate the weights of each variable via global sensitivity analysis as pie-charts by the total effect, C_{dest} and ρ_v, are very important for P_{diff}; additionally, C_{prod} and L do not noticeably contribute in either case. Furthermore, the weights of P_{diff} are very similar for Case 290C and 296B. As for T_{diff}, the importance of L clearly increases, and even equals the importance of C_{dest} and ρ_v in Case 296B, while in Case 290C, the weight is only 6%. This surely indicates that the thermal effects and

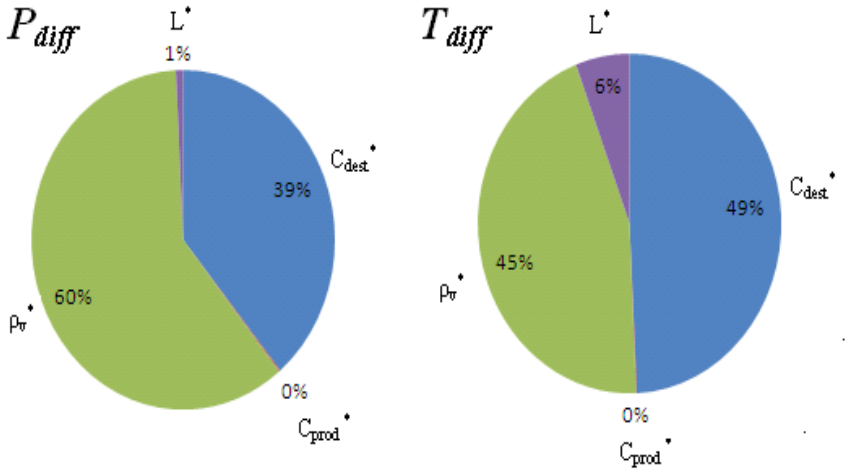

Figure 4.2 Pie-chart of global sensitivity analysis for Case 290C of Hord's experiment [10] (σ_∞=1.7, Re=9.1×10^6, T_∞=83.06K)

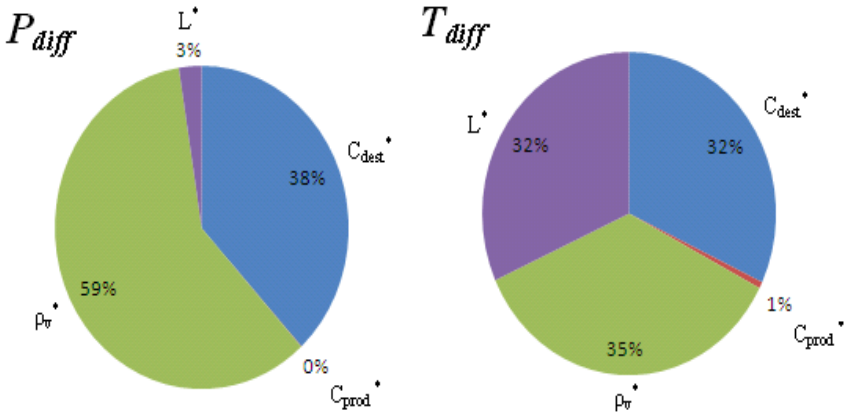

Figure 4.3 Pie-chart of global sensitivity analysis for Case 296B of Hord's experiment [10] (σ_∞=1.61, Re=1.1×10^7, T_∞=88.54K)

importance of the thermodynamic properties will influence the thermal field more significantly as temperature increases (Case 296B has higher inlet temperature than Case 290C). C_{prod} is not important within this design space from the pie-chart, and this implies that the sensitivity of the condensation term is not significant compared with the evaporation term or C_{dest}. This should be expected because cavitation initiates from evaporation, and the condensation strength will also depend on the evaporation strength of the amount of the liquid volume fraction in Equation (2.3). If someone assigns a very low strength to the evaporation term, the condensation dynamics will still be weak possibly even when C_{prod} is large because the vapor inside the cavity will not be sufficient for the condensation source term. Thus the weight of C_{dest} is much more important than C_{prod} in this design space.

The cavitation terms are expressed in Equation (2.3):

$$m^- = \frac{C_{dest}\alpha_l}{t_\infty}\frac{\rho_l}{\rho_v}\frac{\min(0, P - P_v)}{(0.5\rho_l U_\infty^2)} \quad m^+ = \frac{C_{prod}(1-\alpha_l)}{t_\infty}\frac{\max(0, P - P_v)}{(0.5\rho_l U_\infty^2)} \tag{2.3}$$

Therefore, it is reasonable to group C_{dest}/ρ_v and show C_{prod} to reveal the variation in strength of cavitation sink and source terms under the combinations of design variables, and then normalize these values in Figure 4.4 and Figure 4.5 as scatter plots. All the normalized values here are from the previous simulation results of the 70 training points. In Figure 4.4 and Figure 4.5, the distributions of P_{diff}^* vs. $(C_{dest}/\rho_v^*)^*$ are approximately the same for Case 290C and 296B because they have consistent pie-charts and weights in the pressure prediction P_{diff}^* in Figure 4.2 and Figure 4.3.

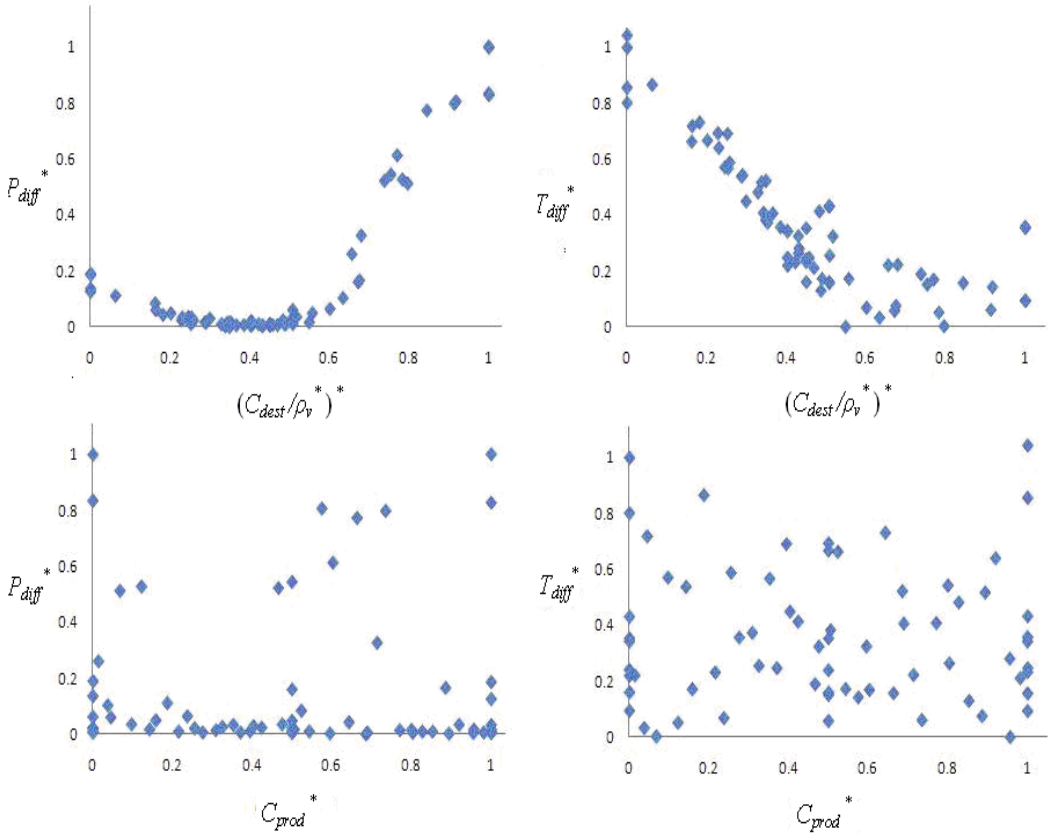

Figure 4.4 Scatter plot for Case 290C of Hord's experiment [10]

(σ_∞=1.7, Re=9.1×10^6, T_∞=83.06K)

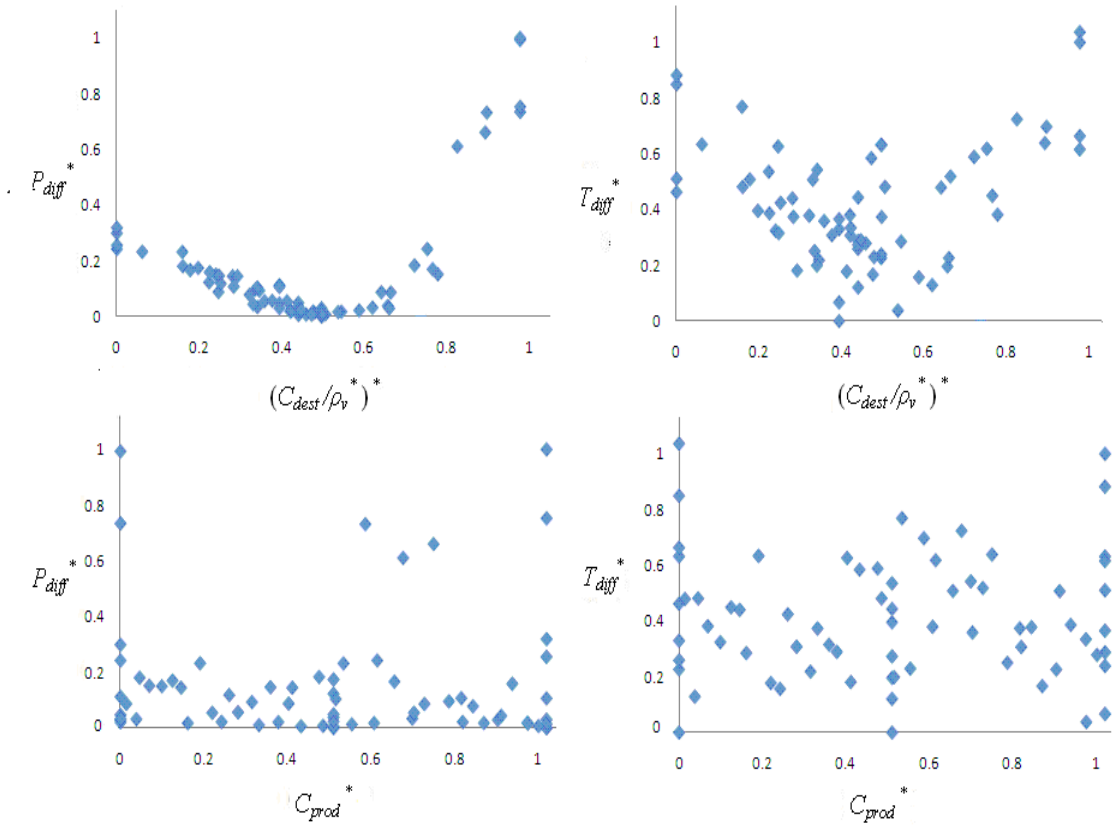

Figure 4.5 Scatter plot for Case 296B Hord's experiment [10]

(σ_∞=1.61, Re=1.1×10^7, T_∞=88.54K)

As $(C_{dest}/\rho_v^*)^*$ is small in Figure 4.4 and Figure 4.5, the sink term is not strong enough so the cavity size is too small; therefore, P_{diff}^* will be large. When $(C_{dest}/\rho_v^*)^*$ goes up to a certain moderate value, P_{diff}^* decreases because the corresponding evaporation term gives a more suitable cavity size. For even large values of $(C_{dest}/\rho_v^*)^*$, the cavity sizes will be too large, so P_{diff}^* will increase again. This clearly indicates that there exists a suitable range for sink term or C_{dest} to obtain good pressure predictions.

As for $(C_{dest}/\rho_v^*)^*$ vs. T_{diff}^*, one still can see similar trends as shown in $(C_{dest}/\rho_v^*)^*$ vs. P_{diff}^*, but these distributions of Case 290C in Figure 4.4 and 296B in Figure 4.5 are not so consistent. This comes from different pie-charts of T_{diff}^* for both cases as shown in Figure 4.2 and Figure 4.3, and it also implies different impacts of thermal effects at different temperatures. Because different fluid properties, namely ρ_v^* or L^*, will influence the flow fields and are not isolated from Figure 4.4 and 4.5, one can see the identical value of $(C_{dest}/\rho_v^*)^*$ can sometimes correspond to different P_{diff}^* and T_{diff}^* in Figure 4.4 and Figure 4.5. In addition, this aspect is more obvious for T_{diff}^* of Case 296B in Figure 4.5, suggesting that L becomes more important in Figure 4.3 for temperature prediction, which also can be shown by comparing Figure 4.2 and 4.3.

As for C_{prod}^*, there is really no trend for P_{diff}^* and T_{diff}^*. This is reasonable because from the pie-chart in Figure 4.2 and Figure 4.3, the importance of C_{prod} is insignificant, and all these distributions in Figure 4.4 and Figure 4.5 would be mainly due to the contributions of the sink term. Therefore, the random distributions for C_{prod}^* vs. P_{diff}^* and T_{diff}^* in

Figure 4.4 and Figure 4.5 validate the insignificant weight of C_{prod} in Figure 4.2 and Figure 4.3 from another viewpoint.

4.3 OPTIMIZATION OF MODEL PARAMETERS

In the next step of the surrogate process, we can optimize the evaporative term C_{dest} within its design range to minimize the pressure and temperature discrepancies between computed results and experimental data. Since the condensation term does not influence the performance of the present cryogenic cavitation model, it is appropriate to fix its value (C_{prod} = 54.4). Additionally, since material properties are not variables that can be tuned for optimization and are studied only to compare the relative sensitivity and uncertainties of the pressure and temperature prediction in these properties, we fix the temperature-dependent material properties ρ_v and L to values obtained from the NIST database [9].

The two objectives are plotted against C_{dest} for both cases in Figure 4.6. Note that while in Case 296B the two objectives show a similar trend to each other, the trends are nearly the opposite in Case 290C. Due to these opposing trends, the optimal value for C_{dest} depends on which objective should be minimized. Instead of a single optimum, there exists a Pareto-optimal set of solutions among which one objective may only be improved at the cost of the other.

Tradeoffs in the function spaces between the two objectives are plotted in Figure 4.7 for both cases. Despite the similar trends in the two objectives in Case 296B as shown in

Figure 4.6(b), Figure 4.7(b) shows that there also exists a Pareto-optimal set, although much smaller than that in Case 290C. Note that in Case 290C, significant reductions in P_{diff} can be realized while incurring a small penalty in T_{diff}. Combined with the fact that pressure fluctuations play a more important role in determining the cavitation dynamics and the loadings on fluid machinery, this nonlinear tradeoff strongly favors reducing P_{diff}, suggesting an optimal value of about C_{dest}=0.65. This value also coincides with one of the Pareto-optimal solutions in Case 296B. Likewise, simulations using C_{dest}=0.65 for other liquid nitrogen cases in Table 4.2 have also shown consistent results with experimental data, suggesting that the optimum is insensitive to differing thermal effects because these cases correspond to different temperatures.

This exercise has helped to validate the model parameter value. Note that since the model parameters are material dependent, the optimal evaporative parameter will vary with different cryogenic fluids. For example, repeating the process with liquid hydrogen for Case 249D (σ_∞=1.57, T_∞=20.7K, Re_∞=2×10^7) and 255C (σ_∞=1.49, T_∞=22.2K, Re_∞=2.5×10^7) in [10] showed that the optimal value should be C_{dest} = 0.78 and C_{dest} = 54.4.

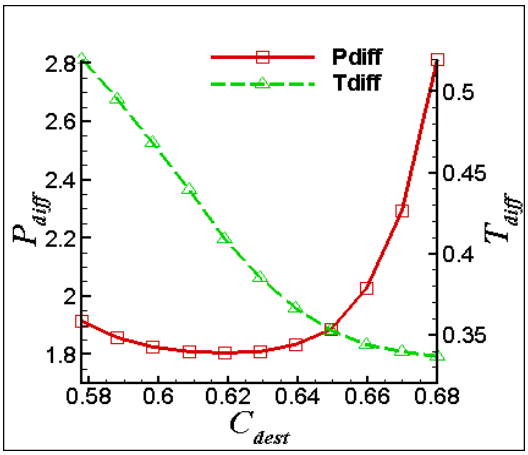

(a) 290C

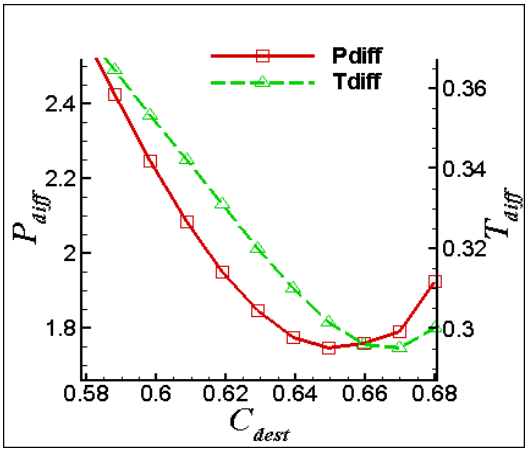

(b) 296B

Figure 4.6 Location of points (C_{dest}) and corresponding responses

(P_{diff} is shown on left y-axis, and T_{diff} is shown on right y-axis) used for calibration of the cryogenic cavitation model

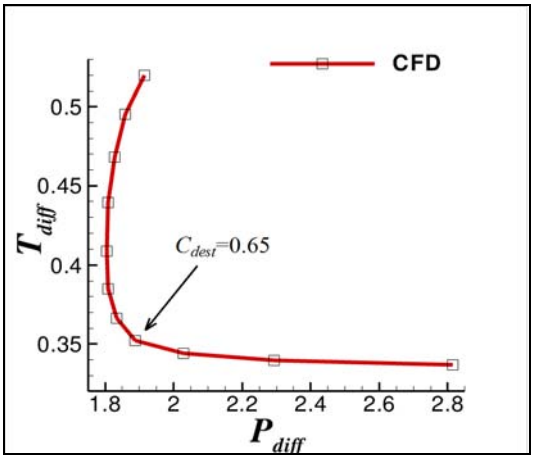

(a) 290C

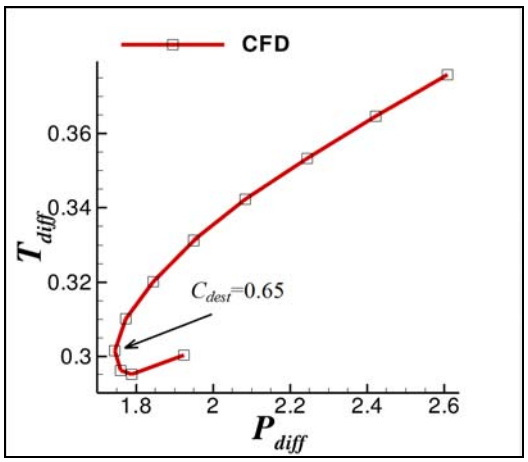

(b) 296B

Figure 4.7 Pareto front of different cases

Table 4.2 C_{dest}=0.65 for other liquid nitrogen cases

Case	σ_∞	T_∞ (K)	P_{diff}(N/cm^2)	T_{diff}(K)
283B	1.73	77.65	1.66	0.32
283C	1.80	77.71	1.31	0.19
293A	1.75	77.64	2.23	0.39

Appendix

Acronyms in this appendix:

PRS	Polynomial Response Surface
KRG	Kriging
RBNN	Radio Basis Neural Network
PWS	PRESS-Based Weighted Average Surrogate
PRESS	The predicted residual sum of square

Table. A1 Error estimate for different cases and surrogates (70 training points)

	P_{diff}^*		T_{diff}^*	
Surrogate	290C	296B	290C	296B
PRESS RMS of PRS	6.38%	11.90%	9.11%	10.02%
PRESS RMS of KRG	2.97%	2.93%	2.48%	6.62%
PRESS RMS of RBNN	13.91%	11.67%	13.31%	19.03%
PRESS RMS of PWS	3.97%	5.44%	5.50%	9.20%

Table. A2 Weights associated with different surrogate models (70 training points)

	P_{diff}^*		T_{diff}^*	
Surrogate	290C	296B	290C	296B
PRS	44.2%	27.5%	31.8%	36.4%
KNG	47.4%	44.5%	45.0%	39.6%
RBNN	8.4%	28.3%	23.2%	24.0%

Table. A3 Test points inside the normalized design space

	C_{dest}^*	C_{prod}^*	ρ_v^*	L^*
No.1	0.692	0.2336	0.7828	0.6928
No.2	0.5806	0.9394	0.2	0.7639
No.3	0.8039	0.1432	0.4183	0.8426
No.4	0.0435	0.4289	0.0991	0.4591
No.5	0.3308	0.6054	0.8575	0.0395

Table. A4 Predictions error of P_{diff} for case 290C

PRS	KRG	RBNN	PWS	CFD
-2.3%	-2.7%	-8.0%	-3.6%	1.865
-7.4%	-2.7%	-5.4%	-5.0%	3.788
30.6%	3.0%	12.0%	14.8%	2.387
19.2%	-5.3%	-1.6%	4.3%	1.847
-5.7%	0.2%	-3.7%	-2.7%	1.969

Table. A5 Predictions error of T_{diff} for case 290C

PRS	KRG	RBNN	PWS	CFD
-0.2%	-0.5%	1.2%	0.0%	0.406
1.4%	-1.7%	-9.1%	-2.4%	0.341
6.4%	1.8%	-0.7%	2.7%	0.321
3.2%	-1.1%	1.1%	0.8%	0.406
-4.4%	0.1%	-0.2%	-1.4%	0.538

Table. A6 Predictions error of P_{diff} for case 296B

PRS	KRG	RBNN	PWS	CFD
-15.9%	-5.1%	12.2%	2.8%	2.3231
55.0%	-3.6%	46.3%	-20.9%	1.9201
35.7%	-6.6%	-26.0%	0.4%	1.9439
0.0%	-6.8%	28.1%	-4.6%	1.7866
-12.0%	-4.6%	28.8%	-2.7%	2.6871

Table. A7 Predictions error of T_{diff} for case 296B

PRS	KRG	RBNN	PWS	CFD
0.6%	0.3%	-2.2%	0.2%	0.2979
6.1%	6.4%	1.5%	-4.9%	0.3046
8.5%	6.7%	0.2%	-5.5%	0.2768
1.2%	0.9%	-1.6%	-0.4%	0.3467
-0.6%	1.0%	-1.3%	0.1%	0.3915

(The column for CFD in Appendix Table A4 to A7 denotes simulation results before normalized.)

BIBLIOGRAPHY

1. Sobol, I.M.: Sensitivity Analysis for Nonlinear Mathematical Models. Mathematical Modeling & Computational Experiment 1(4), 407-414 (1993)
2. Goel, T., Zhao, J., Thakur, S., Haftka, R. T., Shyy, W., Zhao, J.: Surrogate Model-Based Strategy for Cryogenic Cavitation Model Validation and Sensitivity Evaluation", Int. J. Numer. Meth. Fluids 58, 969-1007 (2008)
3. Tseng, C., Shyy, W.: Surrogate-based Modeling of Cryogenic Turbulent Cavitating Flows. CAV2009, Paper No. 77, Proceedings of the 7th International Symposium on Cavitation, August 17-22, 2009, Ann Arbor, Michigan, USA.
4. Queipo, N.V., Haftka, R.T., Shyy, W., Goel, T.,Vaidyanathan, R., Tucker, P.K.: Surrogate Based Analysis and Optimization. Progress in Aerospace Sciences, 41, 1-28 (2005)
5. Goel, T., Haftka, R.T., Shyy, W., Queipo, N.V.: Ensemble of Multiple Surrogates. Structural and Multidisciplinary Optimization 33(3), 199-216 (2007)
6. Myers, R.H., Montgomery, D.C.: Response Surface Methodology, John Wiley, Sons, Inc (1995)
7. Matheron, G.: Principles of Geostatistics. Economic Geology 58, 1246-1266 (1963)
8. Orr, M.J.L.: Introduction to Radial Basis Function Networks, Center for Cognitive Science, Edinburg University, EH 9LW, Scotland, UK. 1996. http://www.anc.ed.ac.uk/~mjo/rbf.html
9. Lemmon, E.W., McLinden, M.O., Huber, M.L.: REFPROP: Reference Fluid Thermodynamic and Transport Properties. NIST Standard Database 23, version 7.0 (2002)
10. Hord, J.: Cavitation in Liquid Cryogens II-Hydrofoil. NASA CR-2156 (1973)

CHAPTER 5

TIME-DEPENDENT TURBULENT CAVITATING FLOW COMPUTATIONS

In this chapter, the impacts of turbulence closures on the flow structures are investigated in the time-dependent turbulent cavitating flows. The transport processes of the evaporation and condensation are also highlighted by comparing the difference between Merkle's phenomenogical model in Equation (2.3) [1-6] and IDM in Equation (2.7) [1,3,5,6] as discussed in Chapter 2.2.

$$m^- = \frac{C_{dest}\alpha_l}{t_\infty}\frac{\rho_l}{\rho_v}\frac{\min(0, P-P_v)}{(0.5\rho_l U_\infty^2)} \quad m^+ = \frac{C_{prod}(1-\alpha_l)}{t_\infty}\frac{\max(0, P-P_v)}{(0.5\rho_l U_\infty^2)} \tag{2.3}$$

$$m^- = \frac{\rho_l \min(P-P_v, 0)\alpha_l}{\rho_v (U_{v,n}-U_{I,n})^2(\rho_l-\rho_v)t_\infty} \quad m^+ = \frac{\max(P-P_v, 0)(1-\alpha_l)}{(U_{v,n}-U_{I,n})^2(\rho_l-\rho_v)t_\infty} \tag{2.7}$$

5.1 HYBRID TURBULENCE MODEL

In this chapter, the turbulence closure is still based on two-equation *k*-*ε* model, which is introduced in Chapter 2.2 from Equation (2.24) and (2.25). Within this framework, eddy viscosity μ_T will be defined as follows:

$$\mu_T = \frac{C_\mu \rho_m k^2}{\varepsilon}, \quad C_\mu = 0.09 \tag{5.1}$$

Furthermore, a filter-based model (FBM) [7] and density correction model (DCM) [8] can also be applied to Equation (5.1):

$$\mu_{T\_FBM} = \frac{C_\mu \rho_m k^2}{\varepsilon} f_{FBM}, \;\; C_\mu = 0.09, \; f_{FBM} = \min\left(1, \frac{\Delta \cdot \varepsilon}{k^{3/2}}\right) \tag{5.2}$$

$$\mu_{T\_DCM} = \frac{C_\mu \rho_m k^2}{\varepsilon} f_{DCM}, \;\; C_\mu = 0.09, \; f_{DCM} = \frac{\rho_v + (\alpha_l)^n (\rho_l - \rho_v)}{\rho_v + \alpha_l (\rho_l - \rho_v)} \tag{5.3}$$

For FBM, if the grid resolution is significantly smaller than the turbulence length scale in the entire flow field, the solution will approach that of the direct numerical simulation; for inadequately resolved computations, the RANS model is recovered. Based on the filter function in Equation (5.2), the sensitivity due to the inlet turbulent quantities can be reduced [9].

To account for the large density jump caused by cavitation and re-entrant jet near the closure region, Singhal et al. [8] and Hosangadi et al. [10] have considered the compressibility of mixture phases and used DCM to modify the eddy viscosity by using Equation (5.3). In fact, the local speed of sound is a function of phase change process, and the value inside the cavity region can drop by orders of magnitude dramatically based on the liquid volume fraction from either value of pure liquid or vapor [11,12]. It leads to the compressibility effect substantial, depending on the liquid volume fraction. Equation (5.3) has considered this aspect and reduced eddy viscosity to compensate the excess eddy viscosity by baseline turbulence model in Equation (5.1)

With such a treatment, the eddy viscosity is reduced based on the liquid volume fraction, as shown in Figure 5.1, with *n*=10; it can be used to capture the unsteadiness due to the re-entrant jet.

It is reported that RANS models often yield excess eddy viscosity [1,3,7,9], which can suppress the large-scale unsteady motion. The filter function in Equation (5.2) and the density correction function in Equation (5.3) provide a systematic approach to reduce the excess eddy viscosity based on the local resolution or mixture density.

Besides the mathematical differences in the filter function and the density correction function, there also exists another major difference. The filter function mainly modifies the eddy viscosity away from the near-wall region. This approach apparently does not correct the eddy viscosity directly near the wall region where cavitation can occur frequently, as discussed in Chapter 3.1. As for the density correction function, generally speaking, it has no influence in the region away from the near-wall region since there is no phase change. However, the density correction function will work aggressively when closer to the cavitation region around the near-wall region. In regards to the affected region, the difference between these two eddy viscosity correction functions is noticeable. From this concept, one can develop a hybrid turbulence model like the following:

$$\mu_{T\_hybrid} = \frac{C_\mu \rho_m k^2}{\varepsilon} f_{hybrid},\ C_\mu = 0.09,\ f_{hybrid} = \chi(\rho_m / \rho_l) f_{FBM} + [1 - \chi(\rho_m / \rho_l)] f_{DCM} \quad (5.4)$$

$$\chi(\rho_m / \rho_l) = 0.5 + \tanh[\frac{C_1(0.6\rho_m / \rho_l - C_2)}{0.2(1 - 2C_2) + C_2}] / [2\tanh(C_1)] \quad (5.5)$$

where C_1.and C_2 are chosen to be 4 and 0.2 respectively. The hybrid function χ (shown in Figure 5.2) will blend the filter-based approach and the density correction method based on the local mixture density.

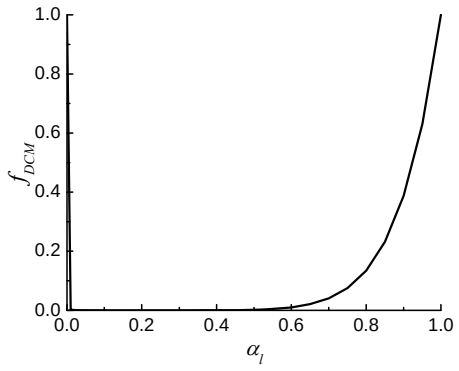

Figure 5.1 Distribution of density correction function

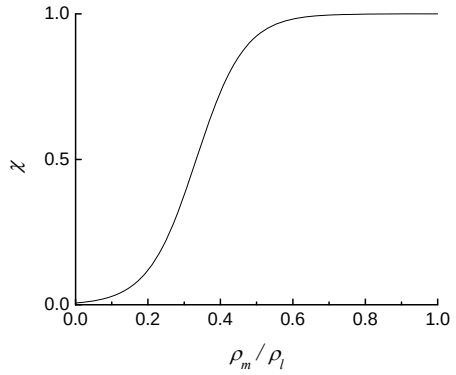

Figure 5.2 Distribution of hybrid function χ

Table 5.1 Turbulence models used in the present study

Model	Eddy viscosity	Modification
Baseline model	$\mu_T = \frac{C_\mu \rho_m k^2}{\varepsilon} f$ $C_\mu = 0.09$	$f_{baseline} = 1$
Filter-based model (FBM)		$f_{FBM} = \min\left(1, \frac{\Delta \cdot \varepsilon}{k^{3/2}}\right)$
Density correction model (DCM)		$f_{DCM} = \frac{\rho_v + (\alpha_l)^n (\rho_l - \rho_v)}{\rho_v + \alpha_l (\rho_l - \rho_v)}$
Hybrid model		$f_{hybrid} = \chi(\rho_m / \rho_l) f_{FBM} + [1 - \chi(\rho_m / \rho_l)] f_{DCM}$ $\chi(\rho_m / \rho_l) = 0.5 + \frac{\tanh[\frac{C_1(0.6\rho_m / \rho_l - C_2)}{0.2(1-2C_2)+C_2}]}{2\tanh(C_1)}$

In this chapter, the baseline k-ε turbulence model (Equation (5.1)), the modified k-ε turbulence model with filter function (Equation (5.2)), the density correct function (Equation (5.3)), and the hybrid function (Equation (5.4)) will be utilized to investigate the impacts of turbulence models. The selected turbulence closures are summarized in Table 5.1.

5.2 TIME-DEPENDENT TURBULENT CAVITATING FLOW ON CLARK-Y HYDROFOIL

The computational domain of the Clark-Y hydrofoil with 22000 cells is given according to the experimental setup in [1,3,13,14], which is shown in Figure 5.3. The boundary conditions – including liquid volume fraction, velocity, temperature, and turbulent quantities – are specified at the inlet. For the outlet, pressure is fixed according to the corresponding cavitation number, and other flow variables are extrapolated. On the walls, pressure, liquid volume fraction, and turbulent quantities are extrapolated along with the no-slip boundary condition. The Clark-Y hydrofoil is placed in the center of a water tunnel with the angle of attack equal to 8º. The Reynolds number and the cavitation number are 7×10^5 and 0.8 respectively, and the flow is basically turbulent with cavity shedding under the current flow conditions. The filter size of FBM in Equation (5.2) is chosen to be 1.5 times larger than the largest grid size in the computation domain, which is around 0.17c. There are five model combinations listed in Table 5.2 to investigate the interactions between cavitation and turbulence models. Furthermore, the time-averaged drag coefficient, lift coefficient, and the primary main frequency obtained by numerical simulations from fast Fourier transfer (FFT) are also provided to compare with experimental data in Table 5.2

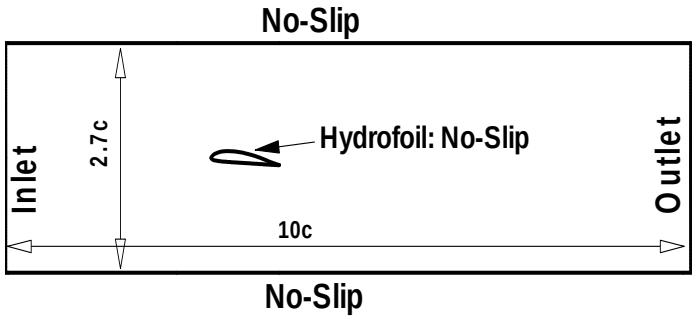

Figure 5.3 Boundary conditions for Clark-Y hydrofoil

Table 5.2 Model combinations and corresponding behaviors

Cavitation model: Phenomenological model (Equation (2.3)) and IDM (Equation (2.7))

Turbulence model: Baseline model (Equation (5.1)), FBM (Equation (5.2)), DCM (Equation (5.3)), and hybrid model (Equation (5.4))

Model combinations	**Cavitation model**	**Turbulence model**	**Primary Frequency (Hz)**	C_l	C_d
Phenomenological-baseline	Phenomenological	Baseline	27.3	0.682	0.118
Phenomenological-FBM	Phenomenological	FBM	27.3	0.669	0.114
Phenomenological-DCM	Phenomenological	DCM	35.1	0.543	0.121
Phenomenological-hybrid	Phenomenological	Hybrid	27.3	0.659	0.110
IDM-hybrid	IDM	Hybrid	39.1	0.641	0.112
Experimental data [1,3,13,14]			24.1	0.760	0.119

5.2.1 TIME-AVERAGED CAVITY VISUALIZATION AND FLOW STRUCTURES

Figure 5.4 shows the time-averaged flow structure and cavity shape. It is clear that the cavitation structures consist of two parts, which are attached and detached cavities respectively. The attached cavity is located in the leading edge of the hydrofoil, while the detached cavity is formed due to the re-entrant jet and will overlap with the recirculation zone near the trailing edge as shown in Figure 5.5. Figure 5.5 highlights the formation and significance of the re-entrant jet by the phenomenological-hybrid model to show the representative unsteady behaviors. The pressure inside the cavity is very low and close to the vapor pressure. When the adverse pressure gradient is strong enough to overcome the weaker momentum of the flow confined by the near-wall region, the re-entrant jet will form and push the flow toward the leading edge during the growth process of the attached cavity.

In Figure 5.5(a), a recirculation zone will consist of the re-entrant jet in the lower part and the incoming flow from upstream in the upper part; the front of the re-entrant jet will determine the cavity closure. The recirculation zone will grow in size, and, simultaneously, the re-entrant jet pushing the attached cavity toward upstream will also become stronger. Then the cavity is detached in Figure 5.5(b) with a low-density region near the center of the recirculation zone. Finally, the detached cavity will be dissipated when it travels toward downstream. In this last stage, the re-entrant jet and the recirculation zone will become weaker. Meanwhile, the attached cavity will grow up again to form the next cycle. The formation of the re-entrant jet and its relationship to the cavity visualizations imply that the re-entrant jet plays a key role in triggering the

unsteadiness of cavitation. The model combinations in Table 5.2 capture these dynamic behaviors, and the difference between each combination will be discussed hereafter.

In regards to Figure 5.4, the time-averaged attached cavity has a lower liquid volume fraction than that of the detached cavity. However, this does not necessarily mean the attached cavity always consists of high liquid volume fraction, but it does mean that the attached cavity tends to remain on the leading edge longer during each cycle, until the re-entrant front arrives. As illustrated in Figure 5.4, the local velocity, where it is near the closure region and the center of the recirculation zone ($> 0.4U_\infty$), is always faster than that of the re-entrant jet ($-0.2U_\infty$ m/s at maximum) in our current flow condition. Therefore, the local velocity will sweep the detached cavity downstream faster than the velocity of the re-entrant jet pushing the attached cavity toward the leading edge. This leads to the longer existence of the attached cavity than the detached one.

From Figure 5.4, one can itemize the following observations:

(1) For the phenomenological-FBM model in Figure 5.4(b) and the phenomenological-baseline model in Figure 5.4(a), the visualization of the time-averaged cavity is very similar, and the only difference is that the size of the detached cavity is slightly larger for FBM. FBM and baseline turbulence models can perform comparably if the inlet turbulence quantities are chosen properly [9]. Therefore, the time-averaged behaviors are very similar under the current setups.

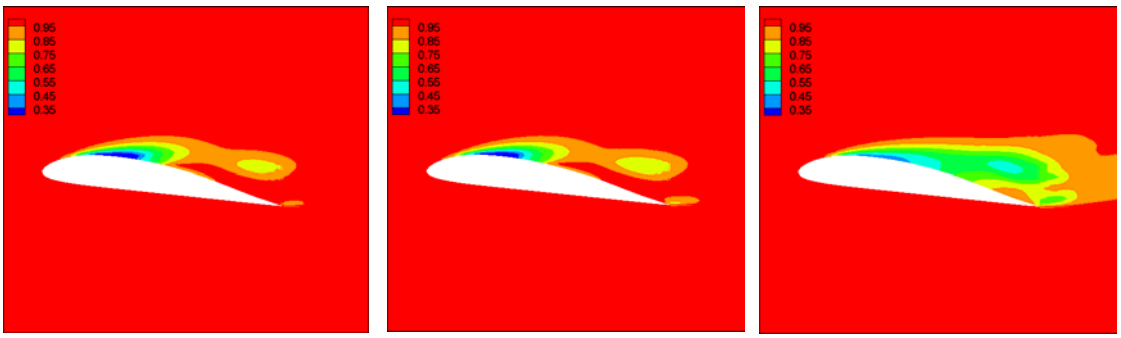

(a) Phenomenological-baseline (b) Phenomenological-FBM (c) Phenomenological-DCM

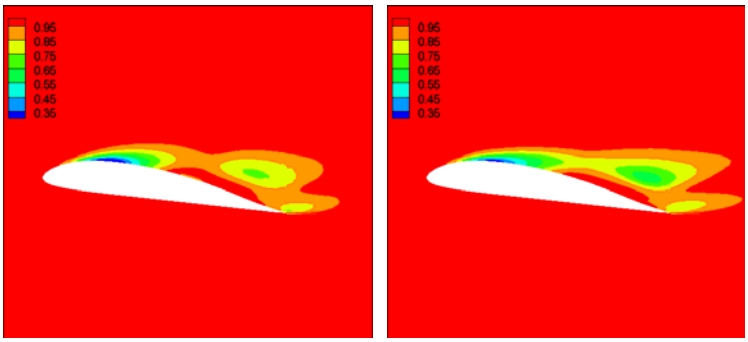

(d) Phenomenological-hybrid (e) IDM-hybrid

Figure 5.4 Time-averaged liquid volume fraction contours

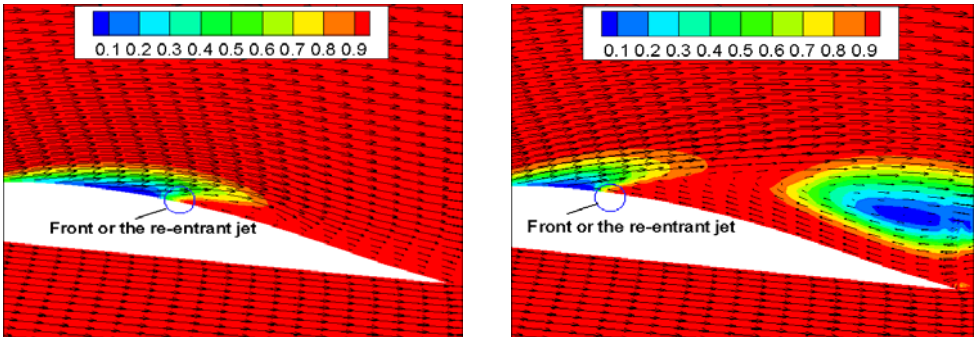

(a) Formation of the re-entrant jet (b) Highlight of the detached cavity

Figure 5.5 The generation of re-entrant jet and detached cavity (by the phenomenological-hybrid model with black arrows as velocity vectors)

(2) For the phenomenological-DCM model in Figure 5.4(c), a bigger time-averaged cavity size is obtained. This is because it has the fastest frequency (35.1Hz) among all the cases by phenomenological cavitation model in Table 5.2.

(3) For the phenomenological-hybrid model in Figure 5.4(d), there is apparently more weight placed from FBM than from DCM because of the similarity between Figure 5.4(b) and (d). Additionally, from Table 5.2, the frequencies are almost the same for the phenomenological-FBM and the phenomenological-hybrid model. The following two aspects can explain the similarity between the phenomenological-FBM and the phenomenological-hybrid model: first, the re-entrant jet, which triggers the shedding and unsteady motion, consists of high liquid volume fraction, and FBM is more influential than DCM model in this area. Second, the hybrid model illustrated in Figure 5.4 tends to use more portions from FBM (90% from FBM when liquid volume fraction is larger than 0.5). However, the detached cavity of the phenomenological-hybrid model surely becomes more substantial than that of the phenomenological-FBM due to the contribution of DCM. The details will be discussed in Chapter 5.2.4 and 5.2.5.

5.2.2 TIME-AVERAGED VELOCITY PROFILES

The mean *x*-direction velocity of the flow field is illustrated in Figure 5.6. These time-averaged velocity profiles are along the vertical direction at different chordwise locations, namely x/c = 20%, 40%, 60%, 80%, 100%, and 120%. The difference between the CFD results and the experimental data becomes more substantial after the closure region. In

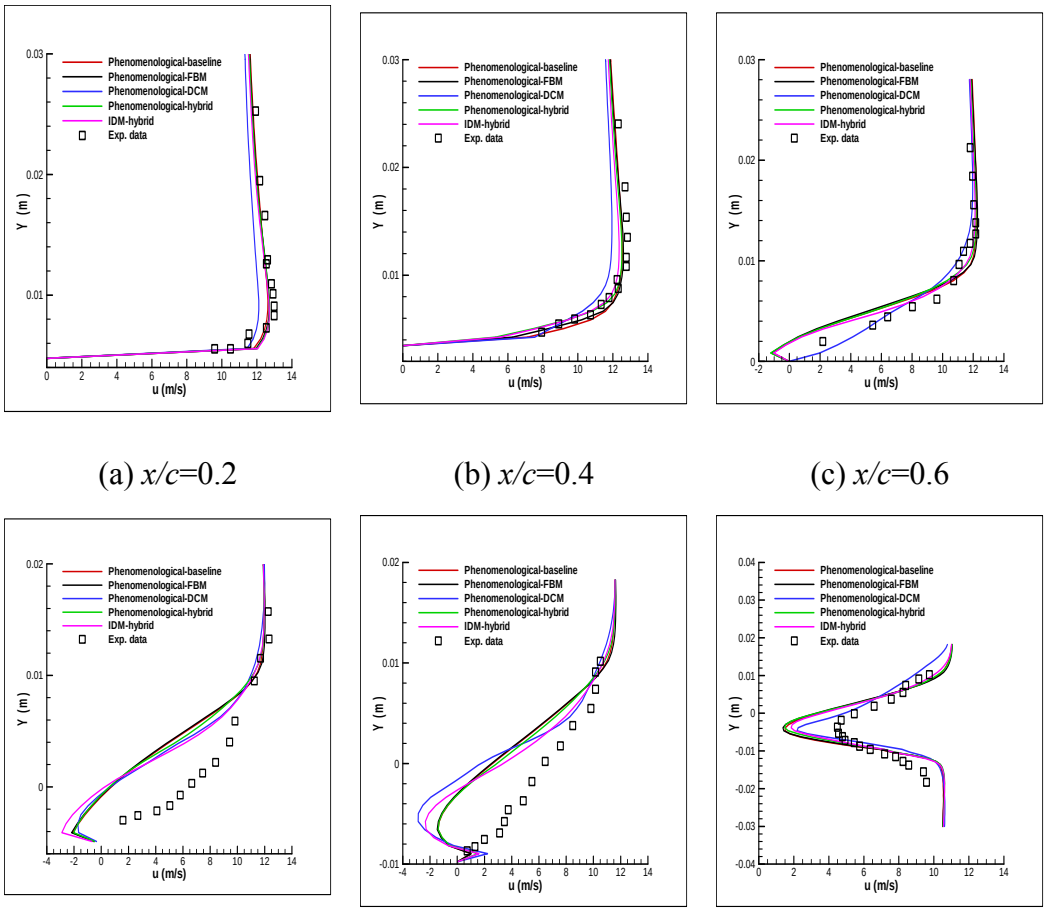

(a) x/c=0.2 (b) x/c=0.4 (c) x/c=0.6

(d) x/c=0.8 (e) x/c=1.0 (f) x/c=1.2

Figure 5.6 Time-averaged x-direction velocity at different locations

general, the agreement is reasonable given the difficulties of the experimental measurement [3,13]. Even though the time-averaged velocity profiles look very similar**,** noticeable differences in instantaneous solutions do exist, especially in the near-wall region. Consequently, different lift forces are presented in Table 5.2. The instantaneous solution characteristics will be highlighted in Chapter 5.2.5.

5.2.3 LIFT AND DRAG COEFFICIENTS

The history profile of lift coefficients is also shown in Figure 5.7 in order to compare it with the experimental data. The CFD results and experimental data are very comparable in Figure 5.7, except for the phenomenological-DCM and IDM-hybrid model, which apparently have faster frequencies in Table 5.2. Also, the phenomenological-DCM model in Figure 5.7(b) has the smallest overall lift coefficient and results in the smallest mean lift coefficient in Table 5.2. Besides the phenomenological-DCM model, there are strong agreements expressed in Table 5.2 between CFD and the experimental data in terms of the mean lift and drag coefficient; these agreements are especially strong between the mean drag coefficients. From the time-averaged flow structures of the phenomenological-DCM in Figure 5.4(b) and IDM-hybrid in Figure 5.4(e), the cavity changes the effective shape of the hydrofoil more substantially, which causes flow to separate more easily with faster frequencies in Table 5.2. Therefore, a smaller mean lift force for these two model combinations is expected.

The frequencies of lift coefficients and their corresponding powers defined as the mean square value of the amplitude are both obtained by FFT analysis, as shown in Table 5.3.

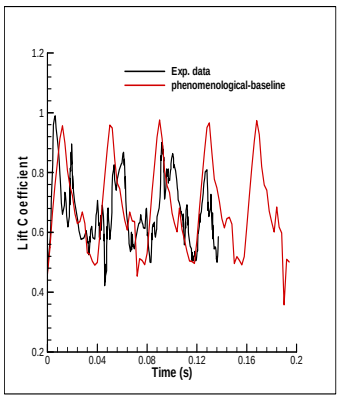

(a) Phenomenological-baseline

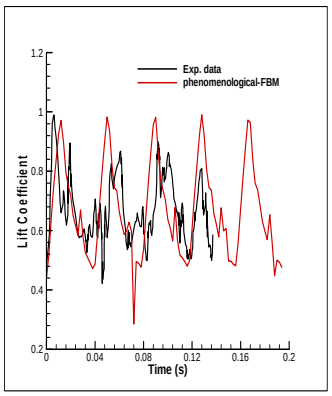

(b) Phenomenological-FBM

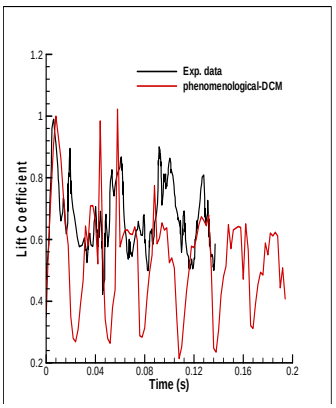

(c) Phenomenological-DCM

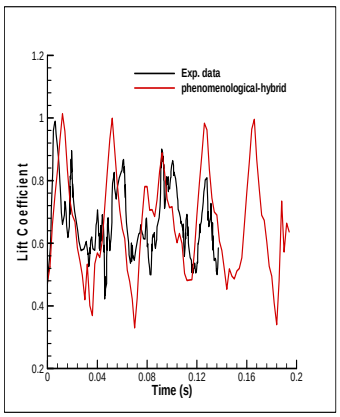

(d) Phenomenological-hybrid

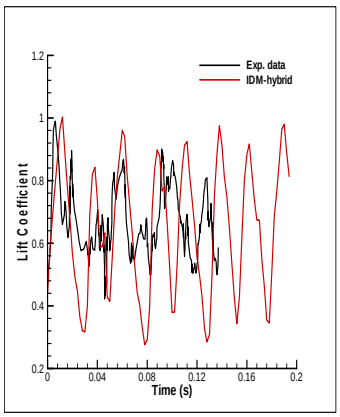

(e) IDM-hybrid

Figure 5.7 History profile of lift coefficient

Table 5.3 Frequency and Power of lift coefficient

Model Combination	Frequency	Power 1	Frequency	Power 2
Phenomenological-	27.3	0.496	50.8	0.121
Phenomenological-	27.3	0.578	50.8	0.134
Phenomenological-	35.1	0.421	70.3	0.078
Phenomenological-	27.3	0.653	43.0	0.064
IDM-hybrid	23.4	0.119	39.1	1.235

FFT for time histories of upper and lower wall pressure are also examined to investigate the source of these two main frequencies in Table 5.3. The results show that the primary main frequencies with stronger power come from the upper wall, while the other weaker main frequencies in Table 5.3 originate from the lower wall. Therefore, the cavitation region on the upper wall determines the primary main frequencies listed in Table 5.2.

5.2.4 TIME-AVERAGED EDDY VISCOSITY

Figure 5.8(a) illustrates the time-averaged eddy viscosity contour determined by the phenomenological-baseline model, and there are two local maximum regions. One is located near the leading edge of the hydrofoil, and the other is located near the closure region of the cavity. In Figure 5.8(b), FBM will filter out the larger portions of the excess eddy viscosity in the regions near the leading edge and away from the cavity shown in Figure 5.8(a). FBM surely reduces the eddy viscosity near the closure region, but not as aggressively as those in the outer region. Basically, the filter function is not invoked in this cavity region because of the resolution and the treatment of the near-wall region. However, FBM places a stronger reliance on DNS. Therefore, the reduction of eddy viscosity is still expected even in the cavity region, so FBM in Figure 5.8(b) only performs a minor reduction of eddy viscosity in the detached cavity region. Consequently, the time-averaged visualization of FBM in Figure 5.4(b) has a slightly bigger detached cavity with a lower density inside than those determined by the baseline turbulence model due to its weaker dissipation of the eddy viscosity in this area.

For the phenomenological-DCM model in Figure 5.8(c), based on the liquid volume fraction, the eddy viscosity is reduced inside the cavity region. Meanwhile, the eddy viscosity of the outer region is consistent with that by baseline turbulence model in Figure 5.8(a). DCM directly performs an aggressive reduction of eddy viscosity, i.e. f_{DCM} =0.4 as α_l=0.9 in Equation (5.3), and it contrasts to FBM in Figure 5.8(b) with only a minor reduction of the eddy viscosity in the detached cavity region. Therefore, the substantially lower eddy viscosity will tend to maintain the evaporation inside the detached cavity and have further shedding toward downstream. The smaller eddy viscosity, which covers the entire cavity region in Figure 5.8(c), will create a stronger cavitation phenomenon in Figure 5.4(c) and faster frequency in Table 5.2.

In Figure 5.8(d) of the phenomenological-hybrid model, it is clear that more weight comes from FBM than that of DCM, which is also consistent with the analysis in Chapter 5.2.1. In the front part of the attached cavity, the density is still high, and thus FBM is mainly applied in this region by the hybrid function in Equation (5.5) and Figure 5.2. In the rear part of the attached cavity, DCM will start to dominate due to the low density in this region. However, the profiles of eddy viscosities by DCM and FBM in this region are very comparable. As for the closure region, the local maximum value in Figure 5.8(d) is smaller than that of FBM in Figure 5.8(b). This contribution definitely comes from DCM. The detail of this aspect will be discussed in the next section.

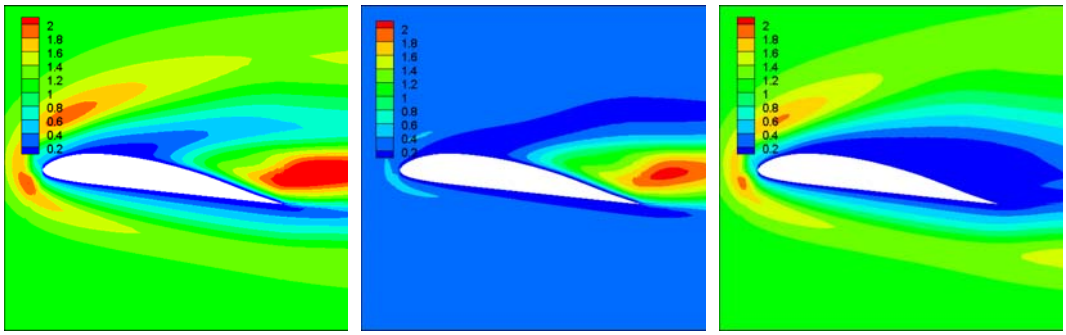

(a)Phenomenological-baseline (b) Phenomenological-FBM (c) Phenomenological-DCM

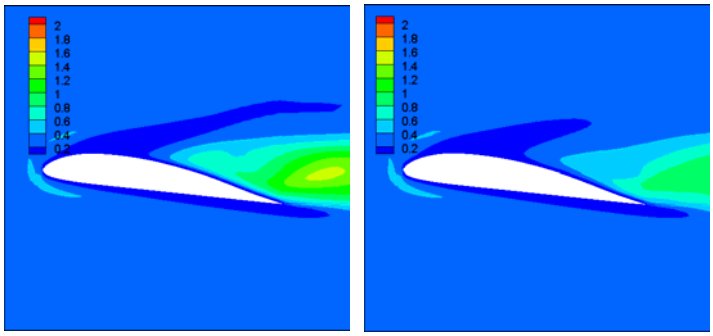

(d) Phenomenological-hybrid (e) IDM-hybrid

Figure 5.8 Time-averaged eddy viscosity contours

As for the IDM-hybrid model in Figure 5.8(e), the eddy viscosity near the closure region is even lower than that of the phenomenological-hybrid model in Figure 5.8(d), which results in a bigger mean size of the detached cavity and a lower density inside in Figure 5.4(e) than those of the phenomenological model in Figure 5.4(d).

5.2.5 INSTANTANEOUS LIQUID VOLUME FRACTION

The instantaneous contours of liquid volume fraction are compared with experimental data side by side in Figure 5.9. In addition, in order to highlight the impact of the turbulence model, the interaction between cavitation and turbulence will be discussed based on the phenomenological cavitation model. Although the frequencies are different between the CFD results and the experimental data, the cavity visualizations are placed side by side according to 20%, 50%, 70%, and 90% of each corresponding cycle.

For the phenomenological-baseline and the phenomenological-FBM models, the instantaneous contours of liquid volume fraction are very similar, so only the results of the phenomenological-FBM model are shown in Figure 5.9(a). The density inside the detached cavity still contains 60% of the liquid phase during 50% to 70% of the cycle. The higher eddy viscosity of FBM near the closure region, as shown in Figure 5.8(b), will dissipate the detached cavity faster than that of DCM even before the density inside starts to largely consist of vapor phase. As a result, the phenomenological-baseline and the phenomenological-FBM models can not capture the detached cavity during 90% of the cycle. Furthermore, there will be a short period without cavitation in the entire flow fields. As for the attached cavity, the maximum cavity length is no more than 0.5c.

For the phenomenological-DCM model in Figure 5.9(b), better comparisons between CFD and the experiment regarding the instantaneous cavity visualization are obtained. The detached cavity is well-captured around 90% of the cycle, which FBM fails to fulfill in Figure 5.9(a). During 20% of the cycle, the detached cavity from last cycle still prevails toward downstream in the right end of the first picture; meanwhile, the attached cavity remains under the growth process. During 50% of the cycle, before it is fully detached, the density inside this region already becomes very low, i.e. α_l<0.1, which is much less than that of FBM in Figure 5.9(a). The stronger evaporation near the closure region, which is due to the small eddy viscosity in Figure 5.8(c), provides a more substantial detached cavity. Thus, the phenomenological-DCM model can capture the detached cavity in the last stage of the cycle, which is observed in the experiment. The detached cavity can prevail further even to 2*c*, and this phenomenon is overestimated by comparing with the experimental data. As for the cavity length of the attached part, it can reach more than 0.8*c*. Because of the longer existence of the detached cavity, the phase change always takes place somewhere in the flow domain.

As for the phenomenological-hybrid model in Figure 5.9(c), the features of every stage in the experiment can be well-captured, including the detached cavity in the trailing edge of the last stage, and it will disappear before 1.2*c*, which is more consistent with the experimental observation. For the attached cavity, the maximum cavity can reach slightly more than 0.5*c*, which is similar to that of FBM but much less than that by DCM model. The density is still high during 50% of the cycle before it is fully detached in Figure 5.9(c). However, this value is already enough to activate the contribution from DCM

Cycle	Experiment	(a) Phenomenological-FBM	(b) Phenomenological-DCM	(c) Phenomenological-hybrid
20%	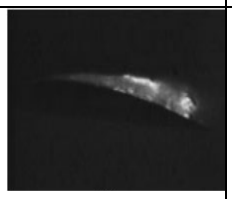	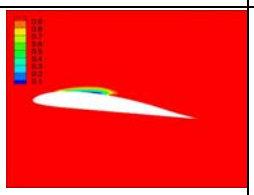	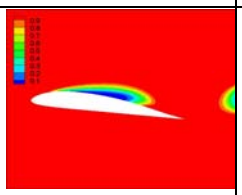	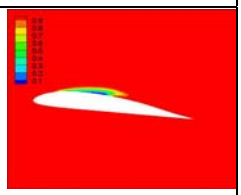
50%	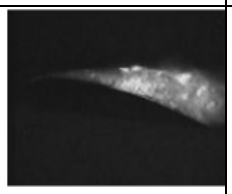	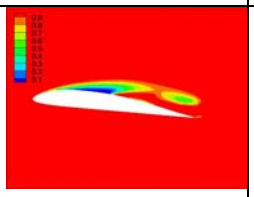	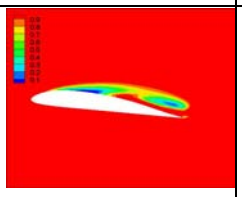	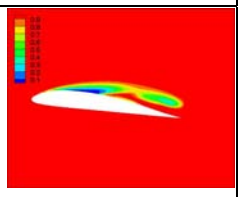
70%	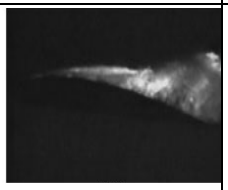	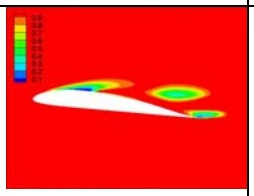	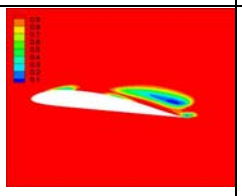	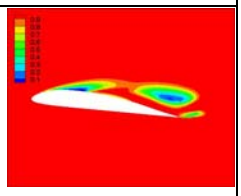
90%	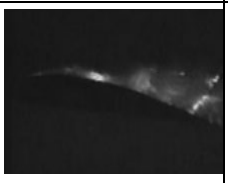	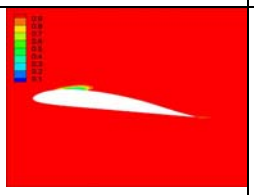	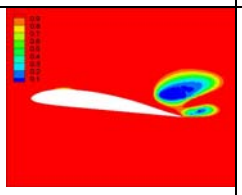	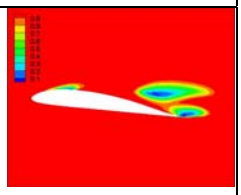

Figure 5.9 Instantaneous contours of liquid volume fraction

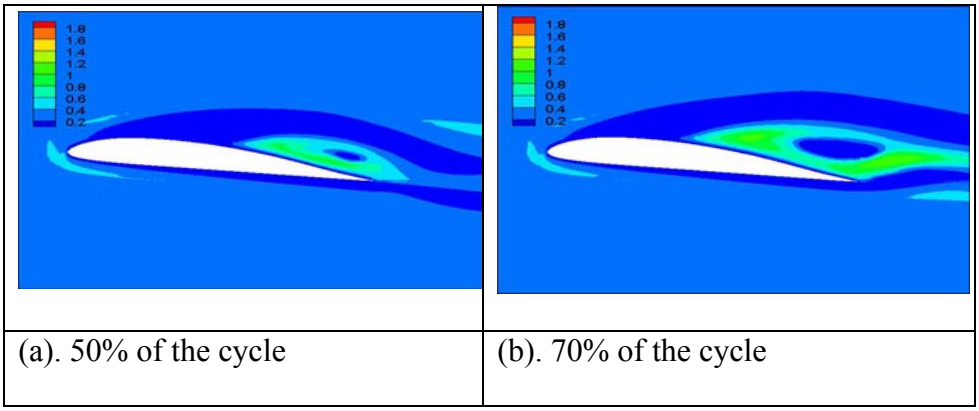

(a). 50% of the cycle	(b). 70% of the cycle

Figure 5.10 Instantaneous contours of eddy viscosity by the phenomenological-hybrid model

(44% from DCM as α_l=0.35). Therefore, a sudden reduction of eddy viscosity in the center of the detached cavity is obtained in Figure 5.10(a) for the instantaneous eddy viscosity contour. In the surroundings, except at the center of the detached cavity, the contribution mainly comes from FBM. However, the sudden reduction due to the aggressive performance of DCM already can enhance the generation of the lower density region during 70% of the cycle in Figure 5.9(c), i.e. α_l=0.1. The area with a sudden reduction of eddy viscosity will grow in size, which is shown in Figure 5.10(b) during 70% of the cycle. This contribution from DCM enhances the detached cavity size compared with that of FBM in Figure 5.9(a), and it weakens the dissipation so that the detached cavity is well-captured in the last stage.

5.2.6 INTERPRETATION OF C_{DEST} AND C_{PROD} OF ALTERNATIVE CAVITATION MODELS

The impact and interactions between cavitation and turbulence models have been investigated in Chapter 5.2.4 and 5.2.5 based on the phenomenological model. In this section, the equivalent model parameters C_{dest}' and C_{prod}' can be obtained by comparing the phenomenological model in Equation (3.3) and IDM in Equation (3.7) as:

$$C'_{dest} = C'_{prod} = \frac{0.5\rho_l U_\infty^2}{(\rho_l - \rho_v)(U_{v,n} - U_{I,n})^2} \tag{5.6}$$

The hybrid turbulence model is used in this section, and there are two purposes for the analysis of C_{dest}' and C_{prod}': (1) to investigate when and where the evaporation and condensation processes become significant and (2) to assess the differences and impacts between the phenomenological model and IDM.

Instantaneous cavity visualization of IDM:

There are several notable aspects when comparing the cavity visualization shown in Figure 5.11(a) of IDM and Figure 5.9(c) of the phenomenological model: (1) during 50% of the cycle, IDM already can generate a low density region before it is fully detached, and while this region of the phenomenological model still largely consists of water during this moment; and (2) the sizes of the detached cavity and its low density region are more substantial in Figure 5.11(a) of IDM.

Instantaneous equivalent model parameters:

The equivalent model parameters C_{dest}' and C_{prod}' are already normalized by C_{dest}=1 and C_{prod}=80 of the phenomenological model respectively in Figure 5.11(b) and (c). Since these two normalized model parameters are also highly consistent with the strengths and distributions of the cavitation sink and source terms, C_{dest}'/C_{dest} and C_{prod}'/C_{prod} can be representative of when and where the evaporation and condensation processes become important in Figure 5.11:

(a) During 20% of the cycle, the evaporation process largely concentrates in the low-density region of the attached cavity while the condensation process is confined to the interface of cavitation.

(b) During 50% of the cycle, the evaporation region travels to the cavity region above the trailing edge, and the value of C_{dest}'/C_{dest} becomes greater, especially in the center of the low-density region. The condensation process is still concentrated in the interface. The

value of C_{prod}'/C_{prod} in the region connecting the cavities above the leading edge and trailing edge also increases in this instant, suggesting the detachment is about to occur in this region.

(c) During 70% of the cycle in Figure 5.11(a), the cavity above the trailing edge is fully detached, and the low-density region inside this area grows in size, which is consistent with the distribution of C_{dest}'/C_{dest} in Figure 5.11(b) during this instant. Additionally, the value is even larger than that during 50% of the cycle. Since the full detachment is already fulfilled, the condensation area fully transports to the surroundings of the detached cavity at this moment.

(d) Finally during 90% of the cycle, the evaporation process in the center of the detached cavity becomes weaker, and the condensation area will become larger hereafter so that the detached cavity will collapse.

The increase and decrease of C_{dest}'/C_{dest} and C_{prod}'/C_{prod} highlight the growth and decay of the cavitation phenomenon. In addition, the phase change process is more significant around the detached cavity than that of the attached part under the current flow conditions.

Comparison of equivalent model parameters between the phenomenological model and IDM:

Furthermore, the difference between the phenomenological model and IDM can be assessed. During 20% of the cycle, C_{dest}'/C_{dest} varies from O(1) to O(2), and C_{prod}'/C_{prod}

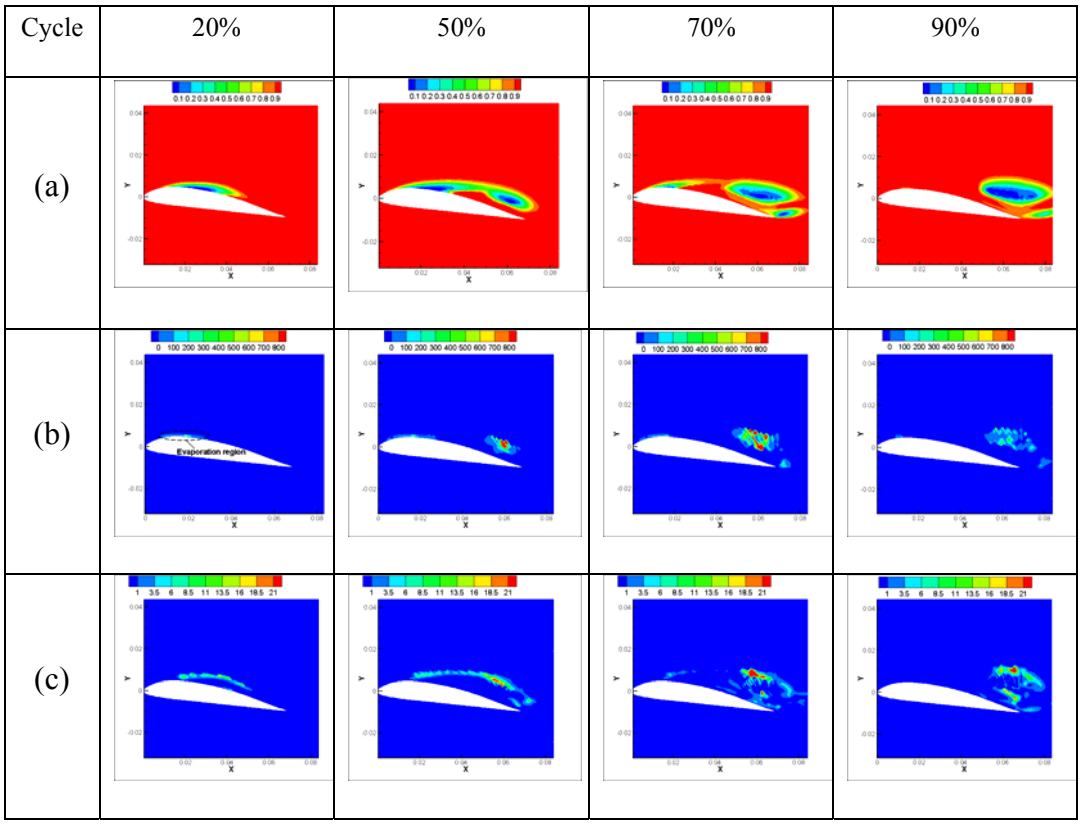

Figure 5.11 (a) Instantaneous cavity visualizations and equivalent model parameters (b) C_{dest}'/C_{dest} and (c) C_{prod}'/C_{prod} of IDM

varies largely around O(1). As from 50% to 70% of the cycle, C_{dest}'/C_{dest} increases from O(2) to O(3) with C_{prod}'/C_{prod} around O(1). Finally during 90% of the cycle, C_{dest}'/C_{dest} decays to O(2), and C_{prod}'/C_{prod} remains around O(1). Therefore, a relatively stronger evaporation process is acquired by IDM than the phenomenological model, which results in a more substantial cavitation phenomenon for IDM, especially in the detached cavity. Therefore, the smaller lift force and faster frequency of IDM in Table 5.2 are expected due to more significant changes in the effective shape of the hydrofoil in Figure 5.4(e). IDM assumes the phase change takes place between the vapor and mixture phases, and thus it can lead to more significant cavitation phenomena by the large density ratio between these two phases.

For the IDM model, the equivalent reference time scale t_∞' can also be obtained by comparing the phenomenological model in Equation (3.3) and IDM in Equation (3.7). The parameter t_∞/t_∞' for the evaporation and condensation processes is the reciprocal of C_{dest}'/C_{dest} and C_{prod}'/C_{prod} for the corresponding phase change process respectively. Therefore, t_∞/t_∞' is around O(1) to O(3) for the evaporation process and O(1) for the condensation process. It implies that the time scale t_∞' of IDM, which is based on interfacial dynamics, will be smaller than the mean flow time scale t_∞, especially for the evaporation process. On the other hand, this suggests the length scale for evaporation can be much smaller than that of condensation. Furthermore, it also reveals that a more precise definition for the time scale in IDM is needed.

Overall, IDM can also capture the detached cavity visualization in Figure 5.9 correctly. However, the performance of the frequency and lift force in Table 5.2 is less accurate compared with those of the phenomenological model.

BIBLIOGRAPHY

1. Utturkar, Y., Wu, J., Wang, G., Shyy, W.: Recent Progress in Modeling of Cryogenic Cavitation for Liquid Rocket Propulsion. Progress in Aerospace Sciences 41(7), 558-608 (2005)
2. Goel, T., Zhao, J., Thakur, S., Haftka, R. T., Shyy, W., Zhao, J.: Surrogate Model-Based Strategy for Cryogenic Cavitation Model Validation and Sensitivity Evaluation", Int. J. Numer. Meth. Fluids 58, 969-1007 (2008)
3. Wu, J.Y., Wang, G.Y., Shyy, W.: Time-dependent Turbulent Cavutating Flow Computations with Interfacial Transport and Filter-based Models. International Journal for Numerical Methods in Fluids 49(7), 739-761 (2005)
4. Merkle, C.L., Feng, J., Buelow, P.E.O.: Computational Modeling of Sheet Cavitation. Proc. 3rd International Symposium on Cavitation, Grenoble, France 1998.
5. Senocak, I., Shyy, W.: Interfacial Dynamics-Based Modeling of Turbulent Cavitating Flows, Part-1: Model Development and Steady-State Computations. Int. J. Numer. Meth. Fluids 44, 975-995 (2004)
6. Senocak, I., Shyy, W.: Interfacial Dynamics-Based Modeling of Turbulent Cavitating Flows, Part-2: Time-Dependent Computations. Int. J. Numer. Meth. Fluids 44, 997-1016 (2004)
7. Johansen, S.T., Wu, J.Y., Shyy, W.: Filter Based Unsteady RANS Computational. International Journal of Heat and Fluid Flow 25, 10-21 (2005)
8. Singhal, A.k., Li, H., Athavale, M.M., Jiang, Y., Mathematical Basis and Validation of the Full Cavitation Model. J. Fluids Eng 124(3), 617-625 (2002)
9. Tseng, C., Shyy, W,: Modeling for isothermal and cryogenic cavitation, Int. J. Heat Mass Transfer 53, 513-525 (2010)
10. Hosangadi, A., Ahuja, V.: A Numerical Study of Cavitation in Cryogenic Fluids. Journal of Fluids Engineering 127, 267-281 (2005)
11. Venkateswaran, S., Lindau, J.W., Kunz, R.F., Merkle, C.L: Computation of Multiphase Mixture Flows with Compressibility Effects. J. Comp. Physics 180(1), 54-77 (2002)
12. Hosangadi, A.,Ahuja, V., Ungewitter, R.J.: Simulations of Cavitating Flows in Turbopumps. Journal of propulsion and power 60(4), 604-611 (2004)

13. Wang, G., Senocak, I., Shyy, W., Ikohagi, T., Cao, S.: Daynamics of Attached Turbulent Cavitating Flows. Progress in Aerospace Sciences 37, 551-581 (2001)

14. Wang G., Zhang B., Huang B., Zhang M. Unsteady dynamics of cloudy cavitating flows around a hydrofoil. CAV2009, Paper No. 9, Proceedings of the 7th International Symposium on Cavitation, August 17-22, 2009, Ann Arbor, Michigan, USA.

CHAPTER 6

CONCLUSIONS AND FUTURE WORK

A computational modeling framework has been further developed for both isothermal and cryogenic cavitation. The cavitation models include the phenomenological model with empirical supports and the interfacial dynamics model (IDM) that utilizes continuity and force balance across the interfaces. For the turbulence closure, a filter-based model (FBM) and density correction method (DCM) have been imposed to the two equation k-ε model.

For the high Reynolds number flows, while cavitation appears largely from the exchange between dynamic and static pressure locally, the viscous effect can significantly modify the shape of a solid object. This results in variations of the cavitation dynamics. For the hemispheric projectile, the cavitation occurs in the straight cylindrical portion of the projectile, and the effect of the displacement thickness on the cavitation process is minor. For the NACA66MOD hydrofoil, the pressure distribution is noticeably more sensitive to the displacement thickness because it modifies the local curvature of the airfoil more substantially. It is shown that FBM can help reduce the impact of the uncertainty associated with the conventional two equation model and the inlet turbulent quantities by reducing the reliance of eddy viscosity based on the local resolution.

For cryogenic cavitation, the evaporative cooling reduces cavitation intensity and results in a shorter cavity size than that under isothermal conditions. The thermal field shows noticeable impact on the local cavitation number. In addition to the effective cavitation number, the liquid-to-vapor density ratio, which varies with the fluid temperature, also influences the intensity of the evaporation and condensation dynamics. Under this statement, it is discovered that Case 296B with a smaller σ_∞ still has a shorter cavity size because of the competing effects between a lower σ_∞ (enhance the cavitation intensity) and smaller density ratio (suppress the cavitation intensity) from a lower inlet temperature.

As for the surrogate-based global sensitivity analysis, C_{dest}, C_{prod}, ρ_v, and L are chosen as design variables to construct the response of pressure prediction P_{diff} and temperature prediction T_{diff} for the cryogenic cavitation. The results demonstrate that the performance of the phenomenological cavitation model is affected most by the evaporation and vapor density terms. In addition, it is shown that the condensation term is not important within this design space, and the latent heat is significant only in temperature prediction. This enables a reduction in dimensionality of the problem, allowing the evaporation term to be optimized to minimize prediction errors of the cavitation model when compared to the experimental data. Although a Pareto front is found demonstrating tradeoffs between the pressure and temperature prediction, we recommend a value of $C_{dest} = 0.65$ due to the large gains available in pressure prediction with only minor sacrifices in temperature prediction.

For the time-dependent computation, the interaction of the cavitation and turbulence models is investigated through different model combinations. The phenomenological model and IDM are used as cavitation models. For the turbulence closure, FBM and DCM have been utilized to reduce the eddy viscosity systematically based on the meshing resolution and density respectively. Moreover, the hybrid model has blended FBM and DCM according to the density. The numerical results show that the difference between each model combination can be significantly different in time dependent processes even when the time-averaged velocity profiles are sometimes reasonably similar. Furthermore, the hybrid model has placed more weight from FBM. However, the contribution of DCM becomes more substantial near the closure region, and it can significantly affect the dynamic behavior of the detached cavity. From the experimental validations, no single model combination performs best in all aspects.

Furthermore, the equivalent model parameter ratios between IDM and the phenomenological model are also investigated to highlight the transport of the phase change process and assess the differences between these two cavitation models. The evaporation and condensation region will travel based on the different stages within each cycle, and the phase change process is more significant around the detached cavity than that of the attached part under the current flow conditions. Moreover, a relatively stronger evaporation process is acquired by IDM, which results in a more substantial cavitation phenomenon, especially in the detached cavity. Therefore, the smaller lift force and faster frequency by IDM are expected. Additionally, it also reveals that a more precise definition for the time scale in IDM is needed for further investigation.

The present study may be extended in the following manner:

(a) LES/DES with necessary resolution.

(b) Multi-scale modeling including bubble interactions and cavity scale phenomena.

(c) Investigation of compressibility in cryogenic fluids.

(d) Examination time dependent flow structures using dynamics model and refinement of the definition for time scale.

(e) Investigation evaporation/condensation dynamics for attached and cloud cavity, and assess the suitability of modeling parameters.

(f) Investigation of the fluid-structure interactions to assess the impacts of cavitation on the structures of underwater vehicles.